# MOLECULAR SIMULATION AND EXPERIMENTAL APPROACH ON THE EFFECT OF MOLECULAR MODIFICATION ON STRUCTURES AND PROPERTIES OF POLYMER ELECTROLYTE

KANJANA   SIRIRAK

A Thesis Submitted in Partial Fulfillment of the Requirements for the

Degree of Master of Science in Chemistry

Suranaree University of Technology

Academic Year 2023

# การจำลองระดับโมเลกุลและวิธีการทดลองผลของการดัดแปลงโมเลกุลต่อโครงสร้างและสมบัติของพอลิเมอร์อิเล็กโทรไลต์

นางสาวกาญจนา ศิริรักษ์

วิทยานิพนธ์นี้เป็นส่วนหนึ่งของการศึกษาตามหลักสูตรปริญญาวิทยาศาสตรมหาบัณฑิต
สาขาวิชาเคมี
มหาวิทยาลัยเทคโนโลยีสุรนารี
ปีการศึกษา 2566

# MOLECULAR SIMULATION AND EXPERIMENTAL APPROACH ON THE EFFECT OF MOLECULAR MODIFICATION ON STRUCTURES AND PROPERTIES OF POLYMER ELECTROLYTE

Suranaree University of Technology has approved this thesis submitted in partial fulfillment of the requirements for a Master's Degree.

Thesis Examining Committee

_____

(Prof. Dr. Kritsana Sagarik)

Chairperson

_____

(Assoc. Prof. Dr. Visit Vao-soongnern)

Member (Thesis Advisor)

_____

(Assoc. Prof. Dr. Chaiwat Ruksakulpiwat)

Member

_____

(Assoc. Prof. Dr. Kamonwad Ngamchuea)

Member

_____
(Assoc. Prof. Dr. Yupaporn Ruksakulpiwat)
Vice Rector for Academic Affairs
and Quality Assurance

_____
(Prof. Dr. Santi Maensiri)
Dean of Institute of Science

กาญจนา ศิริรักษ์ : การจำลองระดับโมเลกุลและวิธีการทดลองผลของการดัดแปลงโมเลกุล ต่อโครงสร้างและสมบัติของพอลิเมอร์อิเล็กโทรไลต์ (MOLECULAR SIMULATION AND EXPERIMENTAL APPROACH ON THE EFFECT OF MOLECULAR MODIFICATION ON STRUCTURES AND PROPERTIES OF POLYMER ELECTROLYTE) อาจารย์ที่ปรึกษา : รองศาสตราจารย์ ดร.วิสิษฐ์ แววสูงเนิน, 113 หน้า

คำสำคัญ: พอลิเอทิลีนออกไซด์, สารเติมแต่งแบบโมเลกุล, การจำลองแบบมอนติคาร์โล, การตกผลึก ของพอลิเมอร์, ความแข็งของสายโซ่, การจำลองหลากหลายระดับ, MD-EXAFS

การปรุงปรับโครงสร้างของสายโซ่พอลิเมอร์สามารถนำไปสู่คุณสมบัติใหม่ที่ดีขึ้นสำหรับวัสดุ พอลิเมอร์ งานวิจัยนี้ศึกษาวัสดุพอลิเมอร์ที่มีคุณสมบัติเป็นอิเล็กโทรไลต์ โดยใช้วิธีการจำลองในระดับ โมเลกุลและการทดลอง เพื่อให้เข้าใจความสัมพันธ์ระหว่างโครงสร้างและคุณสมบัติของพอลิเมอร์ได้ดี ขึ้น สำหรับการเพิ่มการนำประจุของวัสดุพอลิเมอร์ที่มีคุณสมบัติเป็นอิเล็กโทรไลต์ โดยการหาวิธี สำหรับลดความเป็นผลึกของพอลิเมอร์ เพิ่มความสามารถในการแยกตัวของประจุ และปรับเปลี่ยน คุณสมบัติทางเคมีของสายโซ่พอลิเมอร์

การเติมสารเติมแต่งแบบโมเลกุลและผลของการปรับเปลี่ยนความแข็งของสายโซ่พอลิเมอร์ เพื่อลดระดับความเป็นผลึกของพอลิเมอร์ได้รับการศึกษา โดยวิธีการทดลองและการจำลองด้วย คอมพิวเตอร์ สำหรับวิธีการทดลอง ได้มีการศึกษาคุณลักษณะเฉพาะของวัสดุ รวมถึงพฤติกรรมการ ตกผลึกและคุณสมบัติทางความร้อนของพอลิเมอร์ ซึ่งสัมพันธ์กับค่าการนำไฟฟ้าของประจุ สำหรับ การคำนวณ การจำลองแบบมอนติคาร์โลถูกนำมาใช้เพื่อศึกษาการตกผลึกและพลวัตของสายโซ่พอลิ เมอร์ สำหรับเปรียบเทียบกับวิธีการทดลอง และเพื่อศึกษาพอลิเมอร์ชนิดใหม่ การจำลองหลากหลาย ระดับถูกนำมาศึกษาคุณสมบัติทางโครงสร้างและวัสดุของเปอร์ฟลูออโรพอลิเอทิลีนออกไซด์ (perfluoro-polyethylene oxide, PF-PEO) ชนิดอสัณฐานและเปรียบเทียบกับพอลิเอทิลีนออกไซด์ (polyethylene oxide, PEO) แบบจำลองระดับอะตอมที่ความหนาแน่นรวมจะถูกสร้างและ เปรียบเทียบคุณสมบัติต่าง ๆ กับข้อมูลการทดลอง เช่น การกระจายมุมบิด พารามิเตอร์การละลาย ฟังก์ชันความสัมพันธ์ของคู่อะตอม และปัจจัยที่มีผลต่อโครงสร้างการกระเจิง นอกจากนี้ โครงสร้าง การล้อมรอบของสารเชิงซ้อนระหว่างเกลือโพแทสเซียมและโมเลกุลขนาดเล็กของพอลิเมอร์ชนิดใหม่ ได้แก่ ไดเมทอกซีอีเทน (1,2-dimethoxyethane, DME) และ ไดเมทิลเอทิลีนไดเอมีน (N,N-dimethyl ethylenediamine, DMEDA) ซึ่งเป็นโมเลกุลขนาดเล็กที่ใช้แทนหน่วยย่อยที่ซ้ำกันของ PEO และ PEI ตามลำดับ ได้ถูกศึกษาโดยใช้วิธีการจำลองทางพลวัตเชิงโมเลกุล (Molecular Dynamic (MD) simulation) และเทคนิค Extended X-ray Absorption Fine Structure (EXAFS)

ส่วนแรกของงานวิจัยคือ การศึกษาเชิงการทดลอง สำหรับผลของการเติมพอลิเอทิลีนไกล
คอล (polyethylene glycol, PEG) ที่มีน้ำหนักโมเลกุลแตกต่างกันและสารเติมแต่งยูเรียต่อการตก
ผลึกและสัณฐานวิทยาของ PEO ผลการศึกษาพบว่า PEG ที่มีน้ำหนักโมเลกุลสูง (20,000 กรัม/โมล)
สามารถเร่งการตกผลึกของ PEO (4,000,000 กรัม/โมล) ได้ ซึ่งตรงข้ามกับ PEG ที่มีน้ำหนักโมเลกุล
ต่ำ (400 กรัม/โมล) จะชะลอการตกผลึกของ PEO ในขณะที่ขนาดผลึกของตัวอย่างยูเรียผสม PEO
จะมีค่าลดลง ในส่วนที่สอง ศึกษาผลของความแข็งของสายโซ่พอลิเมอร์ในการควบคุมการตกผลึกของ
พอลิเมอร์จากการหลอมละลาย โดยใช้แบบจำลองมอนติคาร์โลสำหรับแบบจำลองเม็ดหยาบ ผลการ
จำลองบ่งชี้ว่าอัตราการก่อตัวของโครงสร้างและระดับความเป็นผลึกเพิ่มขึ้นสำหรับสายโซ่พอลิเอทิลีน
(polyethylene, PE) ปกติ การศึกษานี้ชี้ให้เห็นว่า เฉพาะพอลิเมอร์ที่มีความแข็งของสายโซ่ที่
เหมาะสมเท่านั้นที่สามารถแสดงหลักฐานที่ชัดเจนของการตกผลึกได้ ในส่วนที่สาม มีการใช้การจำลอง
โมเลกุลหลากหลายระดับเพื่อสร้างและปรับสมดุลวัสดุพอลิเมอร์อสัณฐานของ PF-PEO และ PEO
ผลลัพธ์ที่คำนวณได้สอดคล้องกับผลลัพธ์ที่ได้จากการทดลอง ส่วนสุดท้ายคือ การศึกษาโครงสร้างการ
ล้อมรอบของประจุโพแทสเซียมใน DME และ DMEDA ผลลัพธ์ที่ได้จากเทคนิคนี้คือชนิดของอะตอม
ข้างเคียง ระยะห่างระหว่างประจุที่สนใจกับอะตอมข้างเคียง และเลขโคออร์ดิเนชัน ซึ่งสัมพันธ์กันใน
ทั้งสองวิธี

สาขาวิชาเคมี           ลายมือชื่อนักศึกษา _____

ปีการศึกษา 2566         ลายมือชื่ออาจารย์ที่ปรึกษา _____

KANJANA SIRIRAK : MOLECULAR SIMULATION AND EXPERIMENTAL APPROACH ON THE EFFECT OF MOLECULAR MODIFICATION ON STRUCTURES AND PROPERTIES OF POLYMER ELECTROLYTE. THESIS ADVISOR : VISIT VAO-SOONGNERN, Ph.D. 113 PP.

Keyword: polyethylene oxide, molecular filler, Monte Carlo simulation, polymer crystallization, chain stiffness, multiscale simulation, MD-EXAFS

Modification of polymer chains can give new and better properties of polymeric materials. In this work, both molecular simulation and experimental techniques were employed to study polymer electrolytes to gain a better understanding of the correlation between the structure and property of the modified polymers. To Increase the ionic conductivity of polymer electrolytes, some of the possible approaches are to find ways to decrease the amount of polymer crystallinity, increase the degree of ion dissociation, and modify the chemistry of the polymer chain.

The addition of molecular fillers and the effect of modified chain stiffness for decreasing the degree of polymer crystallinity were investigated by experiment and computer simulation. For experiments, material characterizations were done including the crystallization behavior and thermal properties of polymers which are related to their ionic conductivity. For computation, Monte Carlo simulation was used to study polymer crystallization and chain dynamics to correlate experimental observation. To study a new polymer host, multiscale simulation for structural and material properties of amorphous perfluoro-poly(ethylene oxide), PF-PEO, was investigated and compared with normal poly(ethylene oxide), N-PEO. Full atomic models at bulk densities were obtained. Properties including torsional angle distribution, solubility parameter, atomic pair correlation function, and scattering structure factor were compared with experimental data. In addition, the solvation structure of small molecule models for new host polymers *i.e.* 1,2-dimethoxyethane (DME) and *N,N*-dimethyl ethylenediamine (DMEDA) which are the small molecules to represent the repeating unit of PEO and PEI, respectively, complexed with salt were compared using the combined method of

molecular dynamic (MD) simulation and Synchrotron extended X-ray absorption fine structure (EXAFS) spectroscopy.

The first part is the experimental study of the effect of adding low molecular weight poly(ethylene glycol), PEG, and urea fillers on the crystallization and morphology of the PEO. High (20,000 g/mol)/low (400 g/mol) molecular weight PEG can accelerate/delay the crystallization of PEO (4,000,000 g/mol), respectively, while the crystal sizes for the PEO blended urea sample are decreased. In the second part, the effect of chain stiffness in controlling polymer crystallization from the melts was studied using the Monte Carlo simulation of the coarse-grained model. Simulation results indicate that the rate of structural formation and the degree of crystallinity are increased for normal PE chains. Our study implies that only polymers with the appropriate chain stiffness can exhibit clear evidence for crystallization. In the third part, the multiscale molecular simulation has been used to generate and equilibrate the amorphous polymeric materials of PF-PEO and N-PEO. The calculated results were in good agreement with those experimental results. The final part is to study the solvation structures of cations in DME and DMEDA. The results obtained from this technique were the type of neighbor atoms, the distance between the probed ion and neighbor atoms, and the coordination number which are related in both methods.

School of Chemistry

Academic Year 2023

Student's Signature _____

Advisor's Signature _____

# ACKNOWLEDGEMENTS

Kanjana  Sirirak

# CONTENTS

# CONTENTS (Continued)

# CONTENTS (Continued)

# CONTENTS (Continued)

# LIST OF TABLES

# LIST OF FIGURES

# LIST OF FIGURES (Continued)

# LIST OF FIGURES (Continued)

# LIST OF FIGURES (Continued)

# LIST OF FIGURES (Continued)

# LIST OF ABBREVIATIONS

| | |
|---|---|
| PEO | Poly(ethylene oxide) |
| SPEs | Solid polymer electrolytes |
| KSCN | Potassium thiocyanate |
| CG | Coarse-grained model |
| MC | Monte Carlo |
| *2nnd* | Second Nearest Neighbor Diamond lattice |
| QC | *ab initio* quantum chemistry |
| PF-PEO | Perfluoro poly(ethylene oxide) |
| EXAFS | Extended X-ray Absorption Fine Structure |
| MD | Molecular dynamic |
| DME | 1,2-dimethoxyethane |
| DMEDA | N,N-dimethyl ethylenediamine |
| SAXS | Small-Angle X-ray Scattering |
| POM | Polarized Optical Microscopy |
| DSC | Differential Scanning Calorimeter |
| $\Delta G_m$ | Free energy change |
| $\Delta S_m$ | Mixing entropy |
| $\Delta H_m$ | Mixing enthalpy |
| °C | Degree celcius |
| $T_g$ | Glass transition temperature |
| $T_m$ | Melting temperature |
| RIS | Rotational Isomeric State |
| LJ | Lennard-Jones |
| $T_c$ | Crystallization temperature |

# LIST OF ABBREVIATIONS (Continued)

| | |
|---|---|
| PE | Polyethylene |
| MCS | Monte Carlo Step |
| $g^+$ | *gauche plus* |
| $g^-$ | *gauche minus* |
| $t$ | *trans* |
| $<r^2>_0/nl^2$ | characteristic ratio |
| $<\mu^2>_0/nm^2$ | dipole moment ratio |
| $B_2$ | the second virial coefficient |
| $\varepsilon$ | well depth |
| $\sigma$ | collision diameter |
| PCFF | the polymer consistent force-field |
| $K^+$ | potassium ion |
| $SCN^-$ | thiocyanate anion |
| OPLS-AA | the optimized potentials for liquid simulations-all atom |
| RDF | radial distribution function |
| CN | coordination number |
| RSF | radial structure function |
| $N_j$ | the number of atoms of type j in the j$^{th}$ shell |
| $F_j(k)$ | the backscattering amplitude from the $N_j$ atom |
| $S_0^2(k)$ | the amplitude reduction factor |
| $R_j$ | the root mean square distance between the central atom and the j$^{th}$ atom |
| $\lambda_j$ | the electron mean free path |
| $\sigma_j$ | the Debye-Waller factor |

# LIST OF ABBREVIATIONS (Continued)

| | |
|---|---|
| Å | Angstroms |
| $n$ | Avrami exponents |
| $k$ | crystallization rate constant |
| $E_{intra}$ | intrachain energies |
| $E_{inter}$ | interchain energies |
| $<R_g^2>$ | mean square radius of gyrations |
| $S_G$ | overall orientation order parameter |
| $M_1(j)$ | intramolecular bond order parameter |
| $S_L$ | intermolecular bond orientation order |
| PCF | intermolecular pair correlation function |
| MSD | mean square displacement of the center of mass |
| OACF | the normalized orientation autocorrelation functions |
| $<R_E^2>^{1/2}$ | root mean square end-to-end distance |
| $\delta$ | Hildebrand's solubility parameter |
| $CED$ | Cohesive energy density |
| D | diffusion coefficient |
| Q | Scattering vector magnitude |

# CHAPTER I

# INTRODUCTION

The demand for highly effective polymer electrolytes in solid-state batteries is increasing due to the intrinsic disadvantages of high cell potentials in liquid electrolytes such as decomposition reactions and flammability. Poly(ethylene oxide) or PEO has been extensively investigated for polymer electrolytes over the past decades because of the high ionic conductivity of PEO-salt complexes (Jo, 2016). However, the poor mechanical and thermal stability and semi-crystalline properties of PEO reduce its efficiency as a solid polymer electrolytes (SPEs). The ionic conductivity of polymer electrolytes can be improved by reducing the crystalline phase and increasing the transport of ions in the segmental movement of the main chain in SPEs (Song, 1999). Many investigations have focused on increasing ionic conductivity at room temperature through methods such as the use of blending, crosslinking, and copolymers achieved by decreasing the crystalline order and the glass-transition temperature ($T_g$) or creating an amorphous phase (Quartarone, 1998 and Dias, 2000).

In semicrystalline polymers, the amorphous phase is preferred for ion dissolves (Lee, 1986 and Robitaille, 1986). The crystalline complex can be formed at low salt concentrations while at higher salt concentrations than the solubility of semicrystalline PEO, a crystalline complex is formed. As a result of the low energy barrier, ions can easily move in the amorphous phase. When salt dissolves in polymer leading to ions dissociation which generates carrier ions and increases the viscosity. These two results provide opposite effects on ionic conductivity.

Blending polymers with mixed molecular weights (Mw) have been studied for PEO-based electrolytes (Preechatiwong, 1996). Poly(ethylene glycol) or PEG with low molecular weight was applied as a plasticizer for PEO/KSCN complexes. Blending PEO (Mw 4,000,000 g/mol) with a mixture of low- and high-Mw PEG can enhance the ionic conductivity of SPEs. This behavior is a result of a change in the effects of salt solubilization and free volume. The molar ratio of 8/1 for an ethylene oxide to potassium ion (O:K) unit displays a high ionic conductivity and an almost completely amorphous state. The ionic conductivity can be improved by the preparation of a new type of SPEs based on PEO/urea blends (Zhang, 2011). The added urea results in enhanced cation transfer and an increase in interface impedance. The salt diffusion coefficient suggests that urea increases the lithium transport. In addition, the structure, conformation, and motions of PEO and PEG were studied in their urea inclusion compounds (Vasanthan, 1996).

In addition, the effect of modifying chain stiffness to decrease the degree of polymer crystallinity that affects conductivity was investigated by experiment and computer simulation. Chain stiffness is an important factor in controlling the polymer crystallization process that arises from structural constraints and hindrances to internal rotation and is intimately related to the macroscopic properties of polymeric materials. The main goal of this study is to examine the role chain stiffness plays in controlling polymer crystallization. The topic of polymer crystallization continues to receive considerable interest and is a challenging topic from the viewpoint of both theory and experiment. Polymer crystallization has been studied by several experimental approaches (Piorkowska, 2013; Derakhshandeh, 2014; Drongelen, 2015). On the other hand, macroscopic theories have been used to explain the crystallization of polymers, such as the Loritzen-Hofmann theory (Hoffman, 1976 and Armitstead, 1992) which become a widely used model and is a theoretical prediction of crystalline thickness and growth rate. In addition, computer simulations can provide an alternative technique to gain molecular understanding during the polymer crystallization process.

The development of multiscale models for complex chemical systems has been used as the concept of multiscale simulation to investigate the structures and properties of amorphous polymeric materials. Coarse-grained (CG) and molecular models for polymer materials consist of electronic degree of freedom and quantum effects which range from a real classic model of chemistry to mesoscale or coarse-grained models by contain the most important components of the polymer system to be simulated. Challenging in computational research for polymer materials is the multiscale simulation that bridges time and length scales and links computational methods to predict properties at the macroscopic level and fundamental molecular behavior (Baschnagel, 2000). In 1995, the Monte Carlo (MC) simulation technique was developed that used the adjusted Rotational Isomeric State or RIS model of coarse-grained polymer chains mapped onto the second nearest neighbor diamond (*2nnd*) lattice (Rapold, 1995). In this work, we refine new RIS models based on *ab initio* quantum chemistry (QC) calculation of the selected polymer segments to the MC technique to gain more accuracy in the conformational statistics of the polymer chain. The normal and perfluoro poly(ethylene oxide), will be selected for illustration and comparison for this multiscale technique.

The Extended X-ray Absorption Fine Structure (EXAFS) has been used to investigate the local structure of the complex between PEO and salts (Chaodamrongsakul, 2014). The solvation structure of tetraglyme:KSCN (TET:KSCN) electrolytes with many ethylene-oxide:K ion (O:K = 20/1) ratios was studied by a combination of molecular dynamic (MD) simulation and Extended X-ray Absorption Fine Structure (EXAFS), as called "MD-EXAFS" technique. This method gives very useful information at the atomistic scale including the average distance between atom pairs around the probed ion ($R_0$) and Coordination Number (CN). The advantages of using TET to typify the PEO are TET and their blends are smaller molecules with similar structures and are easier for equilibration than the long chain. KSCN salt has been considered beneficial to use in SPEs due to it may form either monodentate, bidentate, or tridentate coordination to $K^+$ ion by its S, C, and N atoms. When the $K^+$ ion is coordinated by TET or PEO, it may also induce conformation and ionic aggregation

changes. The MD-EXAFS gives an overall good agreement with the experimental spectra for both the amplitude and frequency of the oscillations.

In this thesis, the effect of the addition of molecular fillers and modifying chain stiffness to decrease the degree of polymer crystallinity were investigated by experiment and computer simulation, respectively. For experiments, material characterizations were done including the crystallization behavior and thermal properties of polymers which are related to their ionic conductivity. For computation, MC simulation was used to study polymer crystallization and chain dynamics to correlate experimental observation. To study a new polymer host, multiscale simulation for structural and material properties of amorphous perfluoro-poly(ethylene oxide), PF-PEO, was studied and compared with normal poly(ethylene oxide, N-PEO. In addition, the solvation structure of small molecule models *i.e.* dimethoxyethane (DME) and dimethylethylenediamine (DMEDA) which are represented to the repeating unit of PEO and PEI, respectively, complexed with salt were compared using the MD-EXAFS technique.

## 1.1    Research objectives

1.1.1    To understand the effect of adding molecular fillers on morphology and crystallization characteristics of the PEO-based electrolytes.

1.1.2    To investigate the effect of local chain stiffness on crystallization behavior by molecular simulation of coarse-grained polymer model.

1.1.3    To generate the bulk amorphous structure of a new polymer electrolyte matrix with a larger chain stiffness i.e., perfluoro-PEO, at the atomistic levels and predict their material properties.

1.1.4    To compare the solvation structure and dynamic of K ion between two model compounds of polymer electrolytes by combined methods of MD simulation and X-ray absorption spectroscopy.

## 1.2 Scope and limitation

### 1.2.1 Molecular simulation

**1.2.1.1** Multiscale molecular simulation will be developed to generate the amorphous structures of PEO and PF-PEO with and without KSCN salt.

**1.2.1.2** Molecular dynamic (MD) simulation will be used to investigate the polymer electrolytes doped with/without KSCN salt on the structural and dynamic properties, the solvation structures of small (DME and DMEDA with KSCN salt) with a combined method of MD and X-ray absorption spectroscopy.

**1.2.1.3** Monte-Carlo (MC) simulation of coarse-grained "polyethylene-like" models on the high coordination lattice will be developed to determine the chain stiffness effect on the structural properties and crystallization of the melts.

### 1.2.2 Experiments

PEO-based electrolytes and molecular fillers (urea and low Mw PEG) were prepared in a thin film form. The structure and properties of these samples will be characterized by various techniques such as

**1.2.2.1** **Differential Scanning Calorimeter (DSC):** to determine the miscibility and the crystallization behavior of K-doped PEO/molecular fillers blends.

**1.2.2.2** **Polarized Optical Microscopy (POM):** to investigate the crystallization kinetics and morphology of PEO/molecular fillers-based electrolytes.

**1.2.2.3** **Small-Angle X-ray Scattering (SAXS):** to study the crystal morphology of PEO/molecular fillers-based electrolytes.

**1.2.2.4** **Extend X-ray Absorption Fine Structure (EXAFS):** to determine the solvation structure of DME and DMEDA doped with $K^+$.

## CHAPTER II

## LITERATURE REVIEWS

## 2.1     Solid Polymer Electrolytes (SPEs)

Solid Polymer Electrolytes or SPEs are polymers with a high molecular weight that can dissolve salts and must consist of oxygen, nitrogen, or sulfur atoms because of their ability to make cations interact and the decomposed salt has a higher ionic conductivity. The characteristic understanding of these electrolyte systems has been devoted to an effort in considerable scientific. Many approaches have focused on increasing the ionic conductivities of SPEs at room temperature ($10^{-3}$ S cm$^{-1}$ or higher). In most of the methods reported, the metal salts with an alkali or alkaline earth are dissolved in the polymer (Bruce, 1995). The metal salts form complexes with monomers that are chelating ions or with the pendant moiety of a large molecule. Moreover, Wright and co-workers (Wright, 1975) studied the details of alkali salt and poly(ethylene oxide) or PEO complexes.

The SPEs and polyelectrolytes are common kinds of polymer electrolytes that have been studied the most. A typical SPEs contains a coordinating polymer which usually is a polyether with dissolved salt (Figure 2.1a). Both cations and anions can be moved in these SPEs. On the other hand, polyelectrolytes consist of charged groups, anions, or cations that can be covalently bonded with the polymers (Figure 2.1b), so they only have the movement of the counterion.
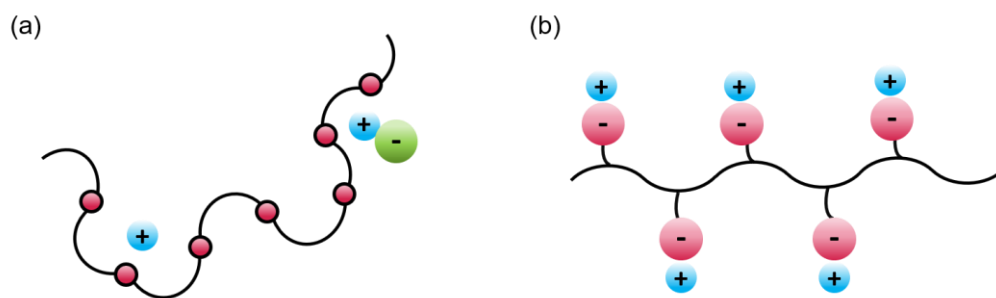
**Figure 2.1** An example system illustrates the difference between (a) SPEs containing salt and (b) polyelectrolytes consisting of ions attached to the polymer.

The advantages of replacing conventional battery liquid electrolytes with SPEs include:

1. Good chemical stability and no reaction with lithium of polyether being a very attractive battery anode due to its low equivalent weight and high reducing power.
2. The weight and volume of the battery dedicated to the electrolyte are decreased.
3. Very attractive mechanical properties such as flexible, deformable, and easily usual manufacturing processes. The typical battery based on a polymer electrolyte contains a thin film (~20-50 mm thick) with a layer structure that is sandwiched between an intercalation cathode and a lithium anode. Whole cells can be produced into continuous tape and can be rolled or folded as finished shapes (Mendolia, 1995).

The SPEs are formed when salts are dissolved into a polymer matrix. To produce these electrolytes, the polymer matrix should be polar and the salts must have low-lattice energy. The free energy change of salt dissolution can be written as:

$$\Delta G_m = \Delta H_m - T\Delta S_m \qquad (2.1)$$

where the $\Delta G_m < 0$ represented spontaneous reaction. $\Delta S_m$ is the mixing entropy composed of configurational and translational entropy. The addition of salt results in a reduction of the movement freedom in the polymer chain through bond formations between polymer and cation leading to a decrease in translational entropy. In contrast, the flexible polymer gives the possibility to adopt different structures appropriately used for the coordination of multidentate cations which may provide a positive configurational entropy. The total solvation entropy is believed to be a positive at first. However, it has been observed that SPEs behave oppositely in liquid electrolytes with the temperature. When the temperature increases, precipitation of salt is observed indicating that the entropy of solvation is negative. $\Delta H_m$ is mixing enthalpy including the lattice energies, starting components, the energy of the ion solvation, and the coulombic ion-ion interaction. The spontaneous solvation or a negative $\Delta G_m$ usually needs salts with low lattice energy that can be defeated by interactions between the ions and the solvent. For the ideal system, the cations in SPEs were dissolved through electrostatic interaction with the polymer backbone and it is believed that the anions have diffusion less or more freely in the matrix. For the non-ideal systems, ion pairs or complex species may be formed.

An aim of the investigation the effective SPEs is the higher transport of cations. To ensure high ionic conductivity, the local cell concentrations are avoided. The mechanisms of ion conduction for the cation and anion differ, the cation hops between polymer chains through the movement of the polymers segmental while temporarily bonded, while the anion diffuses less or more freely. The possibility of polymer structures in the locally obtained complex between cation and polymer is important for the solvation as in Eq. (2.1) and for the mechanism of ionic conduction.

## 2.2    Poly(ethylene oxide), PEO-based Electrolytes

Poly(ethylene oxide) or PEO has been focused on Initial studies of host polymers for ionically conductive. PEO can dissolve well in various common solvents such as methanol, benzene, dichloromethane, acetonitrile, tetrahydrofuran, and carbon tetrachloride at room temperature. In addition, PEO also interacts strongly with inorganic salts and can dissolve many types of salts despite the higher salt

concentration. The solvation structure of salts occurs by the coordination between the oxygens in the polyether backbone with the cations (Figure 2.2). In the polymeric solvent, the solvated ions are quite mobile and cause a significantly larger amount of ionic conduction.
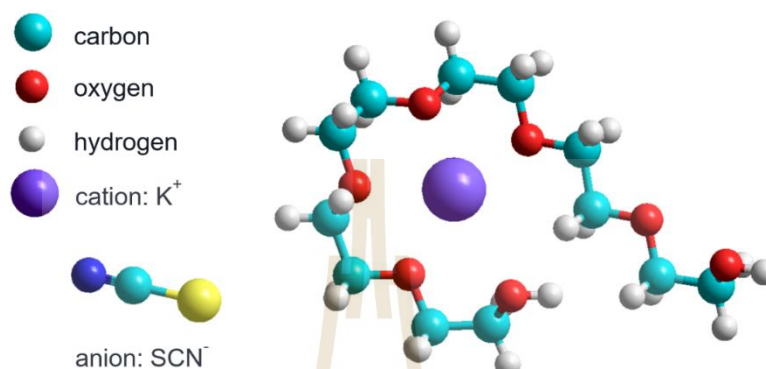


**Figure 2.2** Solvation structure of salts with the PEO chain by ether oxygens of PEO interacts with the cations.

PEO has both a crystalline and an amorphous phase at room temperature because it is a semicrystalline polymer. However, ions can move only significantly within the amorphous regions. At lower temperatures than the melting temperature of pure PEO ($T_m \sim 66°C$), It shows the decreases in ionic conductivity in various PEO-based electrolyte systems. The crystalline phase PEO is non-conductive and blocks the transport of ions. Therefore, the intrinsic crystallinity of the pure PEO is not attractively used in SPEs.

## 2.3    Improved Conductivity of Polymer Electrolytes

Unmodified or Pure PEO is not an ideal host polymer for SPEs at room temperature because of a barrier to ionic transport as a result of the crystalline nature of the PEO. Many researchers have efforts to enhance the efficiency of the salt-doped PEO system based on polymeric material as the following:

1.  Host polymer ought to be a complete amorphous phase due to being non-conductive in the crystalline region.

2. A polymer with a low glass transition temperature ($T_g$) results in easier ionic mobility at room temperature.

3. The system must provide a higher salt dissociation leading to a larger number of charge carriers.

4. The system should facilitate the transport of cations.

5. Electrolytes should have stability in thermal and mechanical properties.

At high temperatures, the PEO-salt electrolytes have pool mechanical properties in which the electrolyte begins to flow. Several mechanisms were used to enhance the mechanical properties of polymers for example by combining crystalline domains into the system, by maintaining the electrolyte component at least one part below $T_g$, by cross-linking polymers, or by using inert fillers. Methods for enhancing mechanical properties sometimes require a loss of ionic conductivity. Many electrolyte-based polymer systems have been studied over the years such as various simple homopolymers, copolymers, polymer blends, networks, polyelectrolytes, comb-branch polymers, plasticized polymers, and polymers with inert fillers. In each system, there are some improvements over conventional PEO salt systems.

However, the plasticized polymer is the most enhancement in the ionic conductivity of SPEs. The conductivities were improved by decreased crystallinity and $T_g$ than the unplasticized polymer. Adding plasticizers results in increasing the mobility of the polymer chain and decreasing the crystalline content which can lead to more ion separation, therefore gaining more charge carriers to transport ions. It may also increase the transport of cations.

## 2.4 Chain Stiffness Effect on Polymer Crystallization

The chain stiffness is an important factor in the polymer crystallization process. According to Flory's theory (Flory,1956), which is a lattice-based model used to investigate the thermodynamic transition in polymers. As the temperature is lower, the chains become stiffer, which leads to a larger amount of volume exclusion that facilitates the transition to the crystalline state. The ordering process of a stiff-chain polymer before cold crystallization was studied using dielectric spectroscopy and the simultaneous real-time wide- and small-angle x-ray scatterings to observe the kinetics

of the ordering process before crystallization (Ezquerra, 1996). The result suggests that the polymer is still in a disordered state during the induction period, which is the period before crystallization begins and the polymer chain segments are still able to move relatively freely.

In addition to experimental and theoretical methods, computer simulations can provide an alternative technique to gain molecular understanding during the process of polymer crystallization. Computational techniques for molecular modeling of polymer crystallization include Molecular dynamics (MD), Langevin dynamics, Brownian dynamics, and Monte Carlo (MC) simulations. Computer simulations based on these methods have been used to gain a molecular understanding of various issues such as structure formation from solutions, crystalline-amorphous interface, temperature protocol, molecular weight or bond stiffness (Yamamoto, 2009; Piorkowska, 2013; Luo, 2013 and 2016). Previous simulations were limited to studying systems with only a few thousand atoms due to the high computational cost. Despite recent advances in computing power, it is still impractical to simulate realistic physical systems at the atomistic level. To this limitation, the coarse-grained (CG) molecular models have been employed to study polymer crystallization at broader lengths and time scales. (Reith, 2001 and Meyer, 2001 and 2002). For instance, the chain stiffness was included in the MC simulation of polymer crystallization in a dilute solution (Chen, 1998). It has a significant effect on chain folding kinetics in the crystalline structure. When the polymers are semi-flexible, the resulting crystals are irregular and contain many defects such as holes and blocks of extended chains within the folded chain lamellae.

An alternative technique based on MC simulation of CG polymer models has been developed to study polymer crystallization (Baschnagel, 2000). Herewith, the rotational isomeric state (RIS) model and the Lennard-Jones (LJ) potential energy were used to treat the conformational statistics of polymers and the non-bonded interactions between monomer units, respectively. Unlike most other lattice-based MC simulations, this technique can be used to study real polymers. Additionally, this method has the advantage of the capacity to be reverse-mapped back to the fully

atomistic models from the underlying CG chains (Wichai, 2021 and Kusinram, 2022). Previously, this MC simulation had been reported for the investigation of polymer crystallization in different environments including nanofiber (Xu, 2002), nanoparticle (Vao-soongnern, 2004), cyclic vs linear chains in bulk (Jamornsuriya, 2022), and mono- vs bimodal mixtures (Vao-soongnern, 2023). In this report, we are interested in extending this technique to investigate the effect of chain stiffness on an initial stage of polymer crystallization upon step-wise cooling from the melts.

## 2.5    Multiscale Simulation for Polymeric Materials

The Monte Carlo (MC) simulation technique was developed in 1995, which used the modified RIS model of coarse-grained (CG) chains mapped onto the second nearest neighbor diamond (*2nnd*) lattice (Rapold, 1995). This technique consists of 3 steps: (1) a fully atomistic chain is mapped onto the CG model at an appropriate high coordination lattice, (2) the MC simulations have been used to perform, and (3) an atomistic model can be obtained by the reverse-mapping step for selected coordination of the high coordination lattice as shown in Figure 2.3. This simulation method had previously been created and used with PE (Rapold, 1996; Cho, 1997; Doruker, 1997), PP (Haliloglu, 1998 and 1998 and Clancy, 2000), PVC (Clancy, 2000 and 2001), and PEO (Helfer, 2003). However, the CG models have been used for most of the past results. Recently, this method has been extended to include the efficient steps to generate and equilibrate a fully atomistic model of the amorphous polymer at bulk density (Vao-soongnern, 2014; Wichai, 2021; Kusinram, 2022). There have been many studies for the simulation of multichain of the PEO such as a system of atomistic detail with short chains of the PEO at the bulk density (Bolodin, 2003 and Chen, 2006). The limitation for large systems is difficult to equilibrium the dense systems when fully atomistic detail is presented. The large system must be able to simulate while the model is represented by the CG chain that keeps contact with reality and permits the reverse-mapping procedure to an atomistic model.

RIS model of a single polymer chain

$$U_{cc} = \begin{bmatrix} 1 & \rho & \rho \\ 1 & \rho & \rho\omega' \\ 1 & \rho\omega' & \rho \end{bmatrix} \quad U_{co} = \begin{bmatrix} 1 & \sigma & \sigma \\ 1 & \sigma & \sigma\omega \\ 1 & \sigma\omega & \sigma \end{bmatrix}$$

$$U_{oc} = \begin{bmatrix} 1 & \rho & \rho \\ 1 & \rho & \rho\omega \\ 1 & \rho\omega & \rho \end{bmatrix}$$

Mapping

Coarse-grained chains mapped onto the *2nnd* lattice

Reverse-mapping

Reverse-mapping to **fully atomistic model** of bulk polymeric materials
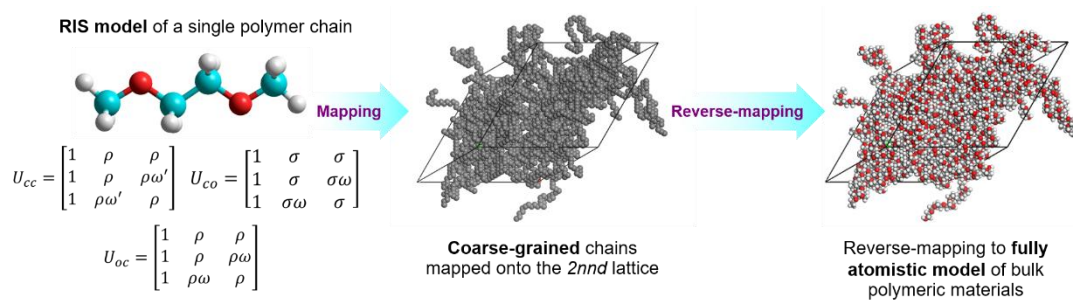
**Figure 2.3** Multiscale simulation with the coarse-grained and reverse-mapped method of PEO.

## 2.6    Structure and Dynamics of Solid Polymer Electrolytes

SPEs include a metal salt and polymer host which salt provides ions to move in the polymer host. A small lattice energy of salt leads to simplified salt dissolving in a polymer host. Polymers that coordinate salt cations should contain Lewis's base groups; O, S, and N atoms. Oligomers with a low molecular weight that is a similar structure to the PEO are extensively used in the model of salt-doped PEO electrolytes (Chaodamrongsakul et al., 2014). Oligomers are in a completely amorphous phase at any available temperature resulting in single-phase systems being prepared and analyzed easily. Alkali metal ions (Li, K, or Na) can be coordinated with the oxygen of the PEO chains, causing dissolute salt to form polymer-salt complexes. This interaction affects the solvation structure of a polymer electrolyte and can be investigated by many measurements for example X-ray diffraction (XRD), infrared and Raman spectra, and Extended X-ray Absorption Fine Structure (EXAFS).

The EXAFS technique has been used to investigate the atomic structure of PEO-salt complexes to gain information about the structure of amorphous material (Teo, 1986 and Linford, 1995) and the nearest-neighbor atoms around the referent element and their distances from the referent element. The difficulty of the EXAFS measurement is it requires high-intensity soft X-rays, therefore, most of the investigated PEO-salt complexes are mainly salts with heavy metals (Catlow, 1983 and McBreen, 1995).

The advances in the application of the MD simulation and EXAFS experiment or MD-EXAFS technique can provide to understanding of the solvated ion in solution (Bandara, 1994; Mancini, 2008; Migliorati, 2011). The atomistic details are fundamental to understanding the physical and chemical properties and ions transport mechanism in solution. The MD simulation is a powerful technique for probing the process of the environment in the condensed phase (Allen, 1987). The structural and dynamic properties of complex systems can be obtained by the MD simulation which may not be done by other techniques. Modern EXAFS approach and the availability of more accurate solvent and ion potential models resulted in many studies using the MD-EXAFS technique greatly increased (Chillemi, 2002; Merat, 2013; Chaodamrongsakul, 2013). For example, a combined MD and EXAFS measurement to characterize the local structure and dynamics of calcium ions in sulfonated polystyrene (Wichai, 2023).
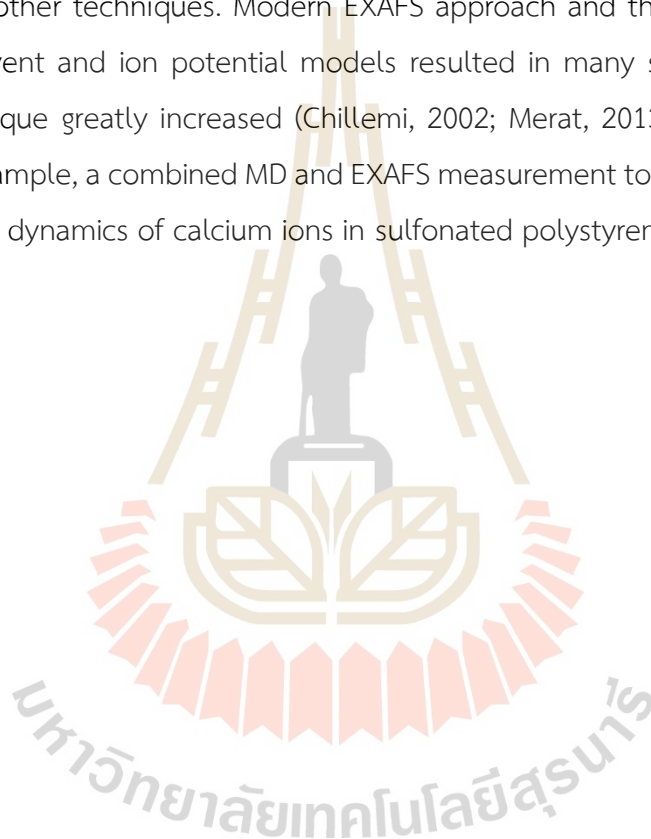
# CHAPTER III

# RESEARCH METHODOLOGY

## 3.1 The Effect of Adding Molecular Fillers on Polyethylene Oxide-based SPEs

### 3.1.1 Sample preparation

**PEO/PEG blends**

The PEO with a molecular weight of 4,000,000 g/mol and PEG with a molecular weight of 400 and 20,000 g/mol were dissolved in the solvent *i.e.*, methanol, and then continuously stirred for 24 hours at room temperature. After that, the solution was kept in the same condition in a fume hood to remove gas. A polymer gel solution was cast on a glass plate to gain a sample in a thin film. To remove the solvent, the film was then dried in a vacuum oven at 50 °C for 24 hours.

**PEO/Urea blends**

The PEO with a molecular weight of 4,000,000 g/mol was added to a saturated solution of urea in methanol at room temperature. The PEO-urea adducts were formed after a few hours of contact. After continuous stirring for 24 hours at room temperature, the solution was kept in the same condition in a fume hood to remove gas. A polymer gel solution was cast on a glass plate to gain a sample in a thin film. To remove the solvent, the film was then dried in a vacuum oven at 50 °C for 24 hours.

### 3.1.2 Differential Scanning Calorimetry (DSC)

DSC has been used to investigate the crystallization and thermal properties of the polymer samples such as the crystallization temperature ($T_c$), melting temperature ($T_m$), and crystallization kinetics. The samples of about 4-5 mg were sealed with an aluminum pan. Crystallization kinetics in Non-isothermal and isothermal processes of the samples were studied. The DSC measurements were performed using Perkin-Elmer Diamond DSC at Yamagata University (Figure 3.1) which was calibrated by the melting of indium and tin. The DSC scans were carried out in a flowing nitrogen atmosphere. For non-isothermal crystallization, the samples were heated from 40℃ to 90℃ at a heating rate of 20℃/min, held at 90℃ for 5 min to erase thermal history, and then cooled to 25℃ at various cooling rates 5, 10, and 15℃/min.
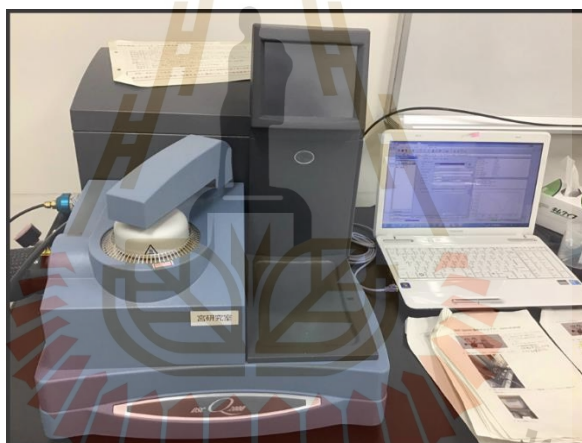


**Figure 3.1** Differential Scanning Calorimetry (DSC) instrument.

DSC measurements for isothermal crystallization, to completely delete the previous thermal history, the polymer samples were melted at 90℃ for 5 min. After that samples were cooled rapidly with a cooling rate of 160℃/min to obtain the temperature for isothermal crystallization DSC (48, 50, 52, and 54℃). Crystallization processes were continued until complete.

### 3.1.3 Polarized Optical Microscopy (POM)

POM measurement is used to determine the morphology of the samples using Olympus BX53M at Matsuba Laboratory, Yamagata University, Japan (Figure 3.2). A

small piece of the sample was sandwiched between two coverslips and was then heated from room temperature to 90°C at a heating rate of 50°C/min, isothermally maintained at 90°C for 3 min, and cooled rapidly with a cooling rate of 50°C/min to the temperature for isothermal crystallization at 48, 50, 52 and 54°C. Crystallization processes were kept until complete.



**Figure 3.2** Polarized Optical Microscopy (POM) instrument.

### 3.1.4 Small-Angle X-ray Scattering (SAXS)

SAXS was used to investigate the morphologies of polymer samples using the NANO-Viewer instrument at Matsuba laboratory (Figure 3.3), Yamagata University, Japan. The measurements were done at room temperature (19°C). The incident X-ray beam was generated by MicroMax-007HF, High Microfocus Rotating Anode X-ray Generator, tube voltage 40 kV, tube current 30 mA.



**Figure 3.3** Small-Angle X-ray Scattering (SAXS) instrument at room temperature.

### 3.2 Molecular Simulation for the Effect of Chain Stiffness on Polymer Crystallization from the Melts

#### 3.2.1 Monte Carlo Simulation

**Rotational Isomeric State (RIS) Model**

The rotational isomeric state model is very useful in the conformational characterization of polymer molecules. This method is based on statistical thermodynamics to determine the average properties of the ensemble derived from different conformations according to its energetics. RIS model employs a small segment, usually a dimer, to calculate statistical weight matrices for each polymer conformation and then employs a matrix multiplication to define the average conformational dependent properties (Flory, 1969).

The RIS model determines the discrete torsional states effect of the covalent bond in polymer chains under additional assumptions of fixed bond length and bond angle. This model determines the conformational partition function (Z) from the conformational energy map obtained from two consecutive torsion angles of the polymer segment in the unperturbed condition. The conformational partition function can be written as

$$Z = \sum_{\phi_1} \cdots \sum_{\phi_n} e^{[-E(\phi_1 \dots \phi_n)/RT]} \tag{3.1}$$

If the rotational states of all bonds were completely independent of others, this expression can be rewritten to a new equation that sums independently over the single torsion angle as

$$Z = \prod_i \left[ \sum_{\phi_i} e^{[-E_i(\phi_i)/RT]} \right] \tag{3.2}$$

where $E_i(\phi_i)$ single bond energy, independent of the states of all other bonds, which can be derived from the total energy of a polymer chain as follows

$$E(\phi_1 \dots \phi_n) = E_1(\phi_1) + E_2(\phi_2) + \dots + E_n(\phi_n) \tag{3.3}$$

However, most polymer chains are influenced by the second-order interaction of their neighbors. To find this interaction, the weight associated with a given conformation is

$$\prod_i e^{[-E(\emptyset_{i-1}, \emptyset_i)RT]} \tag{3.4}$$

The statistical weight of the conformational state for each bond pair is given by

$$u_i(\emptyset_{i-1}, \emptyset_i) = e^{[-E(\emptyset_{i-1}, \emptyset_i)RT]} \tag{3.5}$$

The sum overall rotational states of this product lead to the conformational partition function of a single polymer chain, which is expressed by

$$Z = \sum_{\emptyset_1} \cdots \sum_{\emptyset_n} \prod_i u_i(\emptyset_{i-1}, \emptyset_i) \tag{3.6}$$

$$Z = \prod_i U_i \tag{3.7}$$

where $U_i$ is the statistical weight matrice of bond *i*.

**Mapping of coarse-grained polymers on the *2nnd* lattice**

The second nearest neighbor diamond or "*2nnd*" lattice is a derivative of the diamond lattice where every second site on the diamond lattice is discarded. The result of this lattice is the same as the closest packing of a hard-sphere uniform. It maintains a CN of 12, which is twice higher than that of a cubic lattice. This coarse-grained (CG) lattice gives better calculation efficiency as it reduces the number of particles and the number of conformational states that are appropriate for application to large polymer systems.

For example, the PEO molecule has an "A-A-B" type of repeat unit resulting in the CG chain being a bit more complicated. In this, we make simulations for the PEO chain, which has a ($CH_2$-$CH_2$-O) repeating unit, and one of the $CH_2$ groups is represented as a single atom and O units. In Figure 3.4, every second bead on the backbone is removed, irrespective of C or O, and the residue of the combined atoms is connected. In this method, every single bead must be treated as the same. In other words, there is no difference between the C-C or C-O contacts in terms of the long-range (LR) interactions, but there exists little ambiguity regarding the short-range (SR) interactions. For a coarse-grained PEO chain, the *2nnd* lattice spacing, or step length is calculated as 2.4 Å. When the melt densities of PEO are contented at 373 K, the *2nnd* lattice has an occupancy of about 20% for dense melt systems.

Fully Atomistic Representation



Exclusion of Hydrogen Atoms

Coarse-Grained PEO Chain
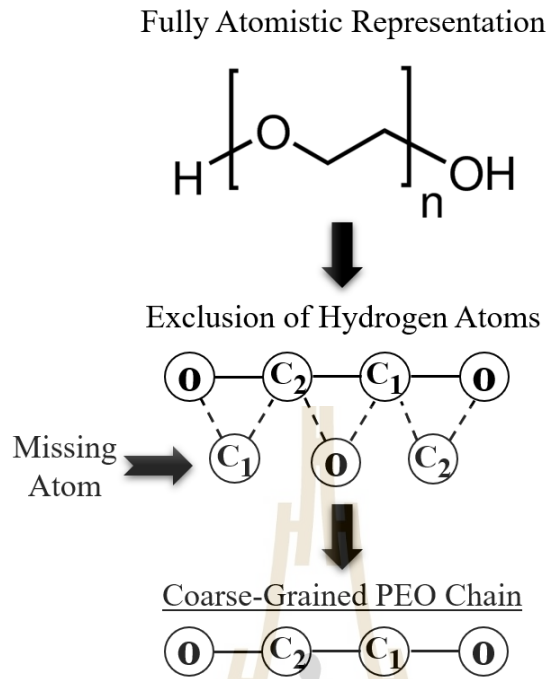
**Figure 3.4** An atomic detailed representation is transformed into a coarse-grained representation for PEO chains.

**Intermolecular and Intramolecular Interactions**

The long-range interaction is determined using a discretized form of the Lennard-Jones (LJ) potential with the second virial coefficient ($B_2$) for polymers which is estimated similarly to a nonideal gas by the Mayer $f$ function according to the imperfect gas theory as follows (Cho, 1997):

$$B_2 = \frac{1}{2} \int \{ \exp[-\beta u(r)] - 1 \} d\mathbf{r} = \frac{1}{2} \int f d\mathbf{r} \qquad (3.8)$$

where $\beta = 1/kT$, $f$ is the Mayer function and $u(r)$ is the inter-particle LJ potential of the form

$$u = \begin{cases} \infty & r < 2.4 \text{ Å} \\ 4\varepsilon\left[\left(\dfrac{\sigma}{r}\right)^{12} - \left(\dfrac{\sigma}{r}\right)^{6}\right] & r \geq 2.4 \text{ Å} \end{cases} \qquad (3.9)$$

where $\varepsilon$ and $\sigma$ are the good depth and the collision diameter, respectively. On the *2nnd* lattice, the prohibition of double occupancy of any site implies $u = \infty$, $r < 2.4$ Å, and $u$ at the remaining sites can be represented by a truncated Lennard-Jones potential energy function. $r$ is the spacing between two interacting beads. On the lattice, $B_2$ is converted in a discretized form by separating the integral into the sub-integral for each lattice cell and regrouping them for each neighbor.

### Types of MC move

Single bead and pivot movement are used to enhance simulation performance. The bond vector for the originally conformational sub-chain was reversed to generate a new configuration in a pivot move (Vao-soongnern, 2000). A sub-chain with 2 to 6 beads was applied for pivot moves. The moves are accepted or rejected according to the Metropolis criterion (Abe, 1976):

$$P_{move} = \min[1, P_{new}/P_{old}] \qquad (3.10)$$

where $P_{new}$ and $P_{old}$ are the probability of the configurations before and after the move made, respectively. The moves are accepted if they are generating a lower energy configuration. Otherwise, a move is accepted with the probability of $P_{new}/P_{old}$ *i.e.* with the Boltzmann factor representing the degree of increase in the conformation energy. The Metropolis criteria were applied to determine the move. For every Monte Carlo step (MCS), single-bead moves and multiple-bead pivot moves were performed randomly. Every bead was tried once in both single bead moves and pivot moves.

### 3.2.2   Chain Stiffness Effect on Polymer Melts

*PE-like* models were represented by the CG chains of 24 ethylene beads mapped onto the second nearest neighbor diamond (*2nnd*) lattice (Xu, 2002; Vao-soongnern, 2004; Wichai, 2021; Jamornsuriya, 2022; Kusinram, 2022; Vao-soongnern, 2023). There were 38 CG chains in the periodic box (16 units in each direction and equivalent to 4.0 nm in each side). The polymer fraction in the *2nnd* lattice is 0.225 equivalent to 0.95 g/cm$^3$ which is close to the density of crystalline PE (Xu, 2001).

Two energetics were used to describe intra- and inter-chain interaction of polymers based on the RIS model (Mattice, 1994) and the LJ potential energy, respectively (Cho, 1997). The conversion of the RIS model for PE chains to the CG version on the *2nnd* lattice can be represented as (Abe, 1965):

$$U_{PE} = \begin{bmatrix} 1 & \sigma & \sigma \\ 1 & \sigma & \sigma\omega \\ 1 & \sigma\omega & \sigma \end{bmatrix} \rightarrow U_{2nnd} = \begin{bmatrix} 1 & 4\sigma & 2\sigma\sigma(1+\omega) \\ 1 & 4a & 2b\sigma(1+\omega) \\ 1 & 4b & 2c(1+\omega) \end{bmatrix} \tag{3.11}$$

Where the first and the second order interaction parameters are calculated by $\sigma = \sigma_0\exp(-E_\sigma/k_BT)$ and $\omega = \omega_0\exp(-E_\omega/k_BT)$ with $k_B$ is Boltzmann's constant, $E_\sigma$, $E_\omega$= 2.1, 8.4 kJ/mol, respectively, and $a = \sigma\omega^{1/8}$, $b = \sigma\omega^{1/4}$ and $c = \sigma^2\omega^{1/2}$.

To model the chain stiffness, the RIS original parameters were multiplied by the constant $k$ which is used to modify the conformational characteristics of the PE chain as the new first ($\sigma' = k\sigma$) and the second order ($\omega' = k\omega$) parameters in statistical weight matrix ($U_{PE}$). For PE-like models with $k$ in the range of 0.5 – 1.5, chains can be regarded as more flexible to stiffer chains than the normal PE ($k = 1.0$).

The range of the chain stiffness parameter ($0.5 < k < 1.5$) is good enough to be able to observe the different behavior of an initial stage of polymer crystallization with step-wise cooling from the melts as will be seen in the Result and Discussion section. Next, the non-bonded interaction energy on the lattice was determined according to the second virial coefficient of the ethylene bead as the non-ideal gas. The LJ potential energy parameters of the CG beads are $\varepsilon/k_B$ = 185 K and $\sigma$ = 0.44 nm for ethylene units (Lavine, 2003).

The starting conformations of polymer in the simulation box were generated as random self-avoiding walks. Then, the intra- and intermolecular interactions were included. Polymer chains were randomly sampled using both single-bead and multiple-bead (pivot) moves to the empty position. The Metropolis rule was implemented for the move acceptance according to the energetic change in each bead move. Monte Carlo Step (MCS) is referred to when every bead was attempted to move once on average (Baschnagel, 2000; Xu, 2001; 2002; Vao-soongnern, 2004; Jamornsuriya, 2022). In this study, the crystallization was investigated at 298 K, much larger than the glass transition of PE (*ca.* 150 K) so that the structure formation can be observed within affordable computational time. Data were analysed for snapshots recorded every 10,000 MCS from the total trajectories of 90 million MCS which were composed of 10 million MCS at 473, 400 and 350 K followed by another 60 million MCS at 298 K.

## 3.3 Multiscale Simulation for Molecular and Material Properties of Perfluoro- and Normal Poly(ethylene oxide) Melts

### 3.3.1 Molecular Dynamic (MD) Simulation

Since every atom in polymer electrolyte materials always moves all the time at the working temperature, the data obtained from the X-ray absorption spectroscopy experiment both the distance between coordination number (CN) and atom pair are an ensemble average from all possible configurations. To gain a more accurate estimation, it is of interest to employ a computational molecular modeling technique that is capable of finding an ensemble average. Unfortunately, the quantum chemistry calculation is deficient in this case as it represents only a set of optimum

configurations. On the other hand, molecular dynamic simulation can solve this problem as the report values are usually averaged from the trajectory consisting of many configurations. The principle of molecular dynamics can be summarized as follows.

Molecular dynamic (MD) simulation is based on the statistical mechanic formalism that links the macroscopic properties of the bulk materials to their microscopic parameters. MD simulation will generate a series of configurations as a function of "time" each of them consisting of the kinetic energy, potential energy, thermodynamic properties, and the structure at a particular state or ensemble. This is because MD can change each configuration both the structure and momentum under thermodynamic equilibrium. If one gets enough number of these "snapshots", one can evaluate the macroscopic properties of the system of interest.

The main thrust of MD simulation is to solve the Newtonian equation of motion for the system composed of $N$ atoms that interact among themselves through the potential function called "force field". The interacting force ($F_i$) on each particle which is a function of time can be obtained from the derivative of the potential function (force field) to the position of this particle as the equation

$$F_{r_i} = -\frac{\partial U}{\partial r_i} \qquad (3.12)$$

where $F_{r_i}$ is the force acting on the $i$th particle, U is the function of potential energy and $r_i$ is the position of the $i$th particle.

The potential function or force field can be calculated from two parts: (1) the bonded energies: bond stretching, bending and torsional terms, and (2) the non-bonded energies: van der Waals, and electrostatic interaction.

The position and velocity of the particle at the next time step can be evaluated by extending the current position and velocity of the particle using Newtonian's equation of motion. This equation is originally written as $F_i = m_i a_i$ where the accelerator ($a_i$) for each particle can be calculated from the reaction force ($F_i$) and the mass of the particle according to the equation:

$$a_i = \frac{F_i}{m_i} \longrightarrow \frac{d^2 r_i}{dt^2} = \frac{F_i}{m_i} \tag{3.13}$$

The solution of this second-order differential equation with time $(\frac{d^2 r_i}{dt^2})$ can be determined by the integration of each particle throughout the time span as

$$\frac{\partial r_i}{\partial t} = \left(\frac{F_i}{m_i}\right) t + c_i \tag{3.14}$$

For the boundary condition, at t = 0, the initial velocity ($u_i$) will be a constant value of $c_i$ and the velocity at time t is $\frac{\partial r_i}{\partial t}$ = $a_i t + u_i$. If $a$ is also constant, one can further integrate to result in the following relation

$$S_i = u_i t = \frac{1}{2} a_i t^2 + c_2 \tag{3.15}$$

where $c_2$ is another constant that has a relation with the position at the resent time. Hence, all the changes can be obtained from the initial velocity $u_i$ and accelerator $a_i \frac{F_i}{m_i}$.

The format of the above equation is in accord with the approximation using Taylor's series expansion up to the second degree as the relation:

$$x(t+\Delta t) = x(t) + \left(\frac{dx}{dt}\right) \Delta t + \left(\frac{d^2 x}{dt^2}\right) \frac{\Delta t^2}{2} + ... \tag{3.16}$$

From this equation, if one knows the position (first term), the velocity (second term), and the accelerator (third term) at the time $t$, one can calculate the position and velocity for the time t+Δt (in practice, the time step Δt is the time interval at which the particles change their position. Usually, we set Δt in the range of femtosecond). There are many numerical algorithms used for solving this integration function of motion such as Verlet, Leap-frog and Beeman. All of them are similar as they consist of looping and changing coordinates for every atom in the system. A set of atomic configurations for the MD run can be averaged in an appropriate ensemble to result in some parameters of interest such as the average distance between atom pair and the coordination number of the reference atom. These data can be directed to the results obtained from EXAFS experiments for the polymer solid electrolyte sample.

**3.3.2   Multiscale Simulation of Perfluoro- and Normal Poly(ethylene oxide) Melts**

**RIS model**

A more complicated RIS model of the perfluoro-poly(ethylene oxide), PF-PEO, and normal poly(ethylene oxide), N-PEO, based on the *ab initio* electronic structure calculations on the conformational energy was suggested by Smith (Smith, 1993; 1995) using the 9 x 9 dimensions of statistical weight matrices to include the third-order interactions, the application of these large matrices to our simulation method needs a huge amount of computational time. In this section, just the first- and second-order interactions with the three rotating isomeric states ($t$, $g^+$, and $g^-$) are used in the typical RIS scheme for coarse-grained PEO. The statistical weight matrices for the skeletal bonds are all 3 x 3 dimensions, so to speak. The Smith model for C-O, O-C, and C-C bonds of PF-PEO and N-PEO can be used to obtain the new reduced forms of the 3x3 statistical weight matrices (while ignoring the third-order interaction) as follows:

For PF-PEO

$$U_{CC-CO} = \begin{pmatrix} 1 & \sigma_1 & \sigma_1 \\ 1 & \sigma_1\varphi_1 & \sigma_1\omega_1 \\ 1 & \sigma_1\omega_1 & \sigma_1\varphi_1 \end{pmatrix} \quad U_{CO-OC} = \begin{pmatrix} 1 & \sigma_2 & \sigma_2 \\ 1 & \sigma_2\varphi_1 & \sigma_2\omega_1 \\ 1 & \sigma_2\omega_1 & \sigma_2\varphi_1 \end{pmatrix}$$

$$U_{OC-CO} = \begin{pmatrix} 1 & \sigma_2 & \sigma_2 \\ 1 & 0 & 0 \\ 1 & 0 & 0 \end{pmatrix} \tag{3.17}$$

where $\sigma_1$ = 1.310, $\sigma_2$ = 0.034, $\omega_1$ = 1.717 and $\varphi_1$ = 1.500.

For N-PEO

$$U_{CC-CO} = \begin{pmatrix} 1 & \sigma & \sigma \\ 1 & \sigma & \sigma\omega \\ 1 & \sigma\omega & \sigma \end{pmatrix} \quad U_{CO-OC} = \begin{pmatrix} 1 & \rho & \rho \\ 1 & \rho & \rho\omega \\ 1 & \rho\omega & \rho \end{pmatrix}$$

$$U_{OC-CO} = \begin{pmatrix} 1 & \rho & \rho \\ 1 & \rho & \rho\omega' \\ 1 & \rho\omega' & \rho \end{pmatrix} \tag{3.18}$$

where $\sigma$ = 0.874, $\omega$ = 5.792, $\rho$ = 0.151 and $\omega'$ = 0.172.

In these matrices, the states of $i$ -1 and $i$ bonds are denoted by the rows and columns, respectively, with $t$, $g^+$, and $g^-$ conformation.

To compare these RIS models from Smith and the condensed forms in Eq. 3.17-

3.18, conformational properties such as the characteristic ratio, $C_n = \langle r^2 \rangle_0 / nl^2$ and the dipole moment ratio, $\langle \mu^2 \rangle_0 / nm^2$ for PF-PEO and N-PEO chain were determined using the usual matrix multiplication scheme (Table 3.1). Herewith, the proposed 3-state RIS model in Eq. 3.17-3.18 will be adopted in this work to describe PF-PEO and N-PEO chain.

**Table 3.1** Comparison of various PF-PEO and N-PEO conformation-dependent characteristics calculated and actual values.

| Polymer | | $\langle r^2 \rangle_0 / nl^2$ | $\langle \mu^2 \rangle_0 / nm^2$ |
|---|---|---|---|
| PF-PEO | Experiment (300 K)[a] | 4.9 | - |
| | Original Smith 6x6 (300 K) | 3.9 | - |
| | This work 3x3 (300 K) | 5.4 | - |
| N-PEO | Experiment | 4.0-5.6[b] | 0.48-0.53[c] |
| | Original Smith 6x6 | 4.5-5.0 | 0.27-0.29 |
| | Abe 3x3 (323 K)[d] | 5.2 | 0.35 |
| | This work 3x3 (323 K) | 6.8 | 0.13 |

[a] Reference (Cotts, 1994)

[b] The experimental $C_n$ of the PEO was determined from viscosity measurements at $\theta$ conditions in polar organic and aqueous inorganic salt solutions.

[c] The mean-square dipole moment data was determined in nonpolar solutions, and the reported mean-square dipole moment ratio was obtained assuming a C-O bond dipole moment of 1.07 D.

[d] Reference (Abe, 1985)

When the RIS model was mapped onto the *2nnd* lattice, it experienced additional modifications for the CG chains. Two backbone diamond; lattice grouping to bead can be attributed to the transition from the *2nnd* lattice. The 12 x 12 matrix can be used to derive and display the connection of two CG beads (Chen, 1991).

$$
\begin{bmatrix} A & B & A & B \\ B & A & B & A \\ A & B & A & B \\ B & A & B & A \end{bmatrix} \text{ and } A = \begin{bmatrix} a & b & c \\ c & a & b \\ b & c & a \end{bmatrix} \quad B = \begin{bmatrix} b & c & a \\ c & d & b \\ d & b & c \end{bmatrix} \quad (3.19)
$$

where $a$ = $tt$ or $g^+g^+$ state, $b$ and $c$ = $tg^+$, $tg^-$, $g^+t$, $g^-t$, $g^+g^+$, $g^-g+$, and *collapse* state, $d$ = $g^-g^-$ or *reverse* state.

Next, the intermolecular non-bonded energies for PF-PEO and N-PEO chains at the bulk density were calculated from the Lennard-Jones (LJ) potential on the *2nnd* lattice. For the CG beads on the *2nnd* lattice, the average bond length for PF-PEO and N-PEO is 1.46 Å. The LJ parameters for numerous small compounds are derived from viscosity measurements. Since the pairs of two backbone atoms are not always the same, the LJ parameters for two N-PEO backbone atoms ($\sigma$ = 3.76 Å and $\varepsilon/k_BT$ = 154 K) were estimated by Vao-Soongnern (Vao-Soongnern, 2014) while two PF-PEO backbone atoms are not known. Here, we propose a simple method to estimate the $\sigma$ and e values. The required value of $\sigma$ for a coarse-grained bead of PF-PEO can be estimated from the data for methane $CH_4$ ($\sigma$ =3.76 Å, $\varepsilon/k_BT$ = 148.6 K) and carbon tetrafluoride $CF_4$ ($\sigma$ =4.66 Å, $\varepsilon/k_BT$ = 134 K) (Poling, 2000) as

$$
\sigma_{\text{PF-PEO}} = \frac{\sigma_{CF_4}}{\sigma_{C H_4}} \times \sigma_{\text{PEO}} \quad (3.20)
$$

from which $\sigma_{\text{PF-PEO}}$ = 4.66 Å. The $\varepsilon$ for two backbone atoms of PF-PEO was estimated by fitting the experimental density of PF-PEO (1.8-1.9 g/mL) in a series of simulations of free-standing PF-PEO thin films that have different $\varepsilon$ values as shown in Figure 3.5. With this method, LJ parameters at the simulated temperature 373 K are: $\sigma$ = 4.66 Å and $\varepsilon/k_BT$ = 178 K. Since our main objective is to generate the fully atomistic of bulk PF-PEO and N-PEO, we are not trying to refine these LJ potentials.

The long-range interaction energies are produced by the discretization of this LJ potential. The parameters for the first three shells of PF-PEO (N-PEO) at 373 K are 14.588, 0.913, -0.712 kJ/mol (8.113, -0.213, -0.339 kJ/mol). Only the first three shells are used in the simulation of bulk systems to increase the speed of computation.
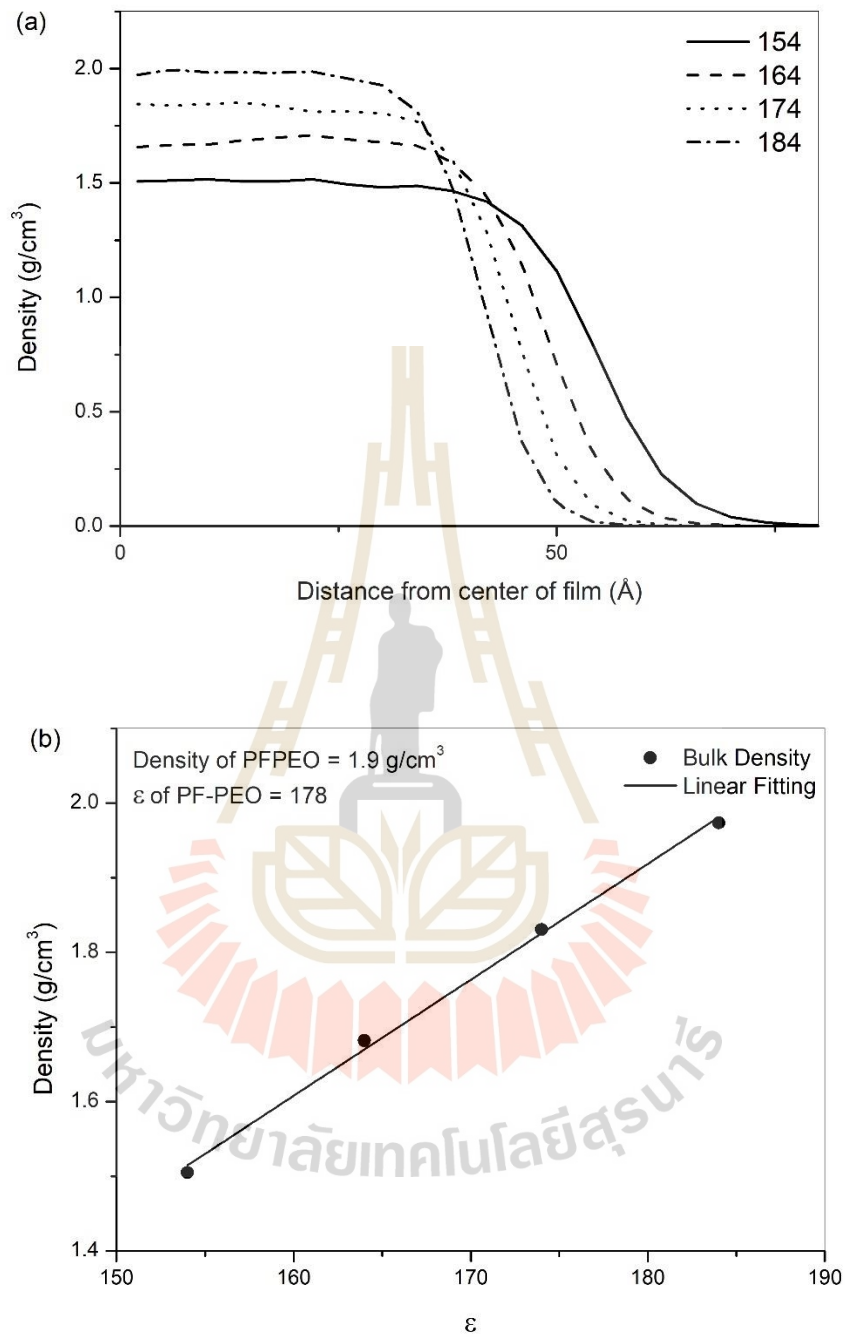
**Figure 3.5** The simulations of free-standing PF-PEO thin films that have different $\varepsilon$ values (a) the density profile and (b) fitting to estimate $\varepsilon$ from the experimental density of PF-PEO.

### Simulation of CG model

The simulations were performed in a periodic box with a length of 20 on each lattice side ($L_x = L_y = L_z = 20$) which is equivalent to 47.8 Å. The PF-PEO (N-PEO) systems consist of 19 (28) chains with $N = 60$ (60) placed in this periodic box to achieve the density of 1.92 (0.99) g/cm$^3$, close to the experimental density of PF-PEO and N-PEO. Each coarse-grained chain can be reverse-mapped to 120 backbone atoms as $CF_3(OCF_2CF_2)_{39} OCF_3$ for PF-PEO and $CH_3(OCH_2CH_2)_{39} OCH_3$ for N-PEO.

The simulation employed pivot (many beads) and single-bead motions. A sub chain of the original conformation containing 2–6 beads underwent a pivot motion to produce a new conformation (Clancy, 2000). The Metropolis criterion (Metropolis, 1953) was used to determine if a bead movement was acceptable or not. Every bead was typically tested once for each Monte Carlo step (MCS) using single bead motions and multiple bead pivot moves. The initial configuration of PF-PEO and N-PEO chains was randomly placed in the periodic box and then all chains in the structure were equilibrated. To ensure the equilibrium, about 90 million MCS was needed at 373 K. Data were recorded every 10,000 MCS for the analysis of polymer systems.

### Fully atomistic model

The CG model of PF-PEO and N-PEO chains on the *2nnd* lattice can restore the backbone C-C, C-O, and O-C bonds on the underlying diamond lattice. After having reverse mapped back onto the diamond lattice, the coordinates of the carbon, oxygen, and hydrogen or fluorene atoms in polymer chains were generated. With the PCFF force field and Xenoview (freeware for molecular mechanic/dynamic simulations), the geometry of the specified snapshots was optimized until the gradient was less than 0.1 kcal/(mol Å). If the gradient is more than 1000 kcal/(mol Å), the steepest descents approach is applied; otherwise, the conjugate gradient method is applied. The potential energy of both structures was again minimized after MD simulation at 373 K. Furthermore, *NVT* molecular dynamics runs for 1 ns at 373 K of the energy-minimized structures were performed to guarantee the structures with greater distribution of all atoms in the periodic box.

## 3.4 Molecular Dynamics (MD) Simulation and X-ray Absorption Spectroscopy to Characterize the Local Structure and Dynamics of Potassium ions in small molecules of SPEs

### 3.4.1 Molecular simulation of DME and DMEDA doped with KSCN salts

The MD simulation is completed by GROMACS 2021.4 with the OPLS-AA force field. The PolyParGen web server was used to generate the input files that include the force field parameters of the DME and DMEDA, while the KSCN system was from the literature (Chaodamrongsakul, 2014 and Wang, 2014). The simulation system consisted of 100 molecules of DME or DMEDA and 10 ions of $K^+$ and $SCN^-$ represented by 100DME10KSCN and 100DMEDA10KSCN. In this work, the structure of the local solvation of the probed ion (K from KSCN salt) is considered to be the main focus. Figure 3.6 shows the partial charge and structure of the DME and DMEDA segment from PolyParGen. The parameters for the non-bonded interaction of each component are listed in Table 3.2.
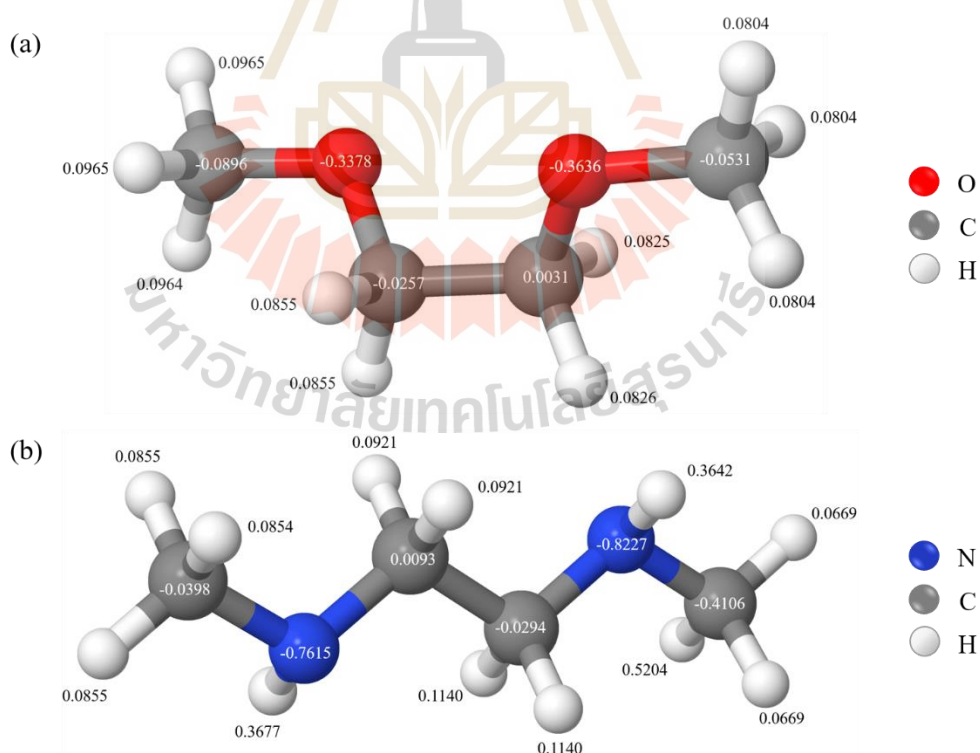


**Figure 3.6** The structure and partial charge of (a) DME and (b) DMEDA unit.

Table 3.2 Non-bond energy parameters of each component in the system.

| Atoms | $\sigma$ (nm) | $\varepsilon$ (kJ/mol) |
|-------|---------------|------------------------|
| DME | | |
| C | 0.350 | 0.276 |
| O | 0.290 | 0.586 |
| H | 0.250 | 0.126 |
| DMEDA | | |
| C | 0.350 | 0.276 |
| N | 0.330 | 0.711 |
| H | 0.250 | 0.126 |

The periodic boundary condition of the cubic cell was used to generate the bulk amorphous structure of DME/DMEDA molecules and KSCN salts and then the Steepest Descent with a toleration of 0.1 kcal.mol$^{-1}$ nm$^{-1}$ was used to perform the energy minimization. The box size was reduced by compression at a higher pressure (30 atm) using the MD simulation with an NPT ensemble for 10 ns and another NPT ensemble at 298 K and 1.0 atm for 10 ns was performed until no change in the box size to obtain the equilibrium density as shown in Figure 3.7. The final density is 0.84 g/cm$^3$ for both 100DME10KSCN and 100DMEDA10KSCN which increase from the pure system (0.82 g/cm$^3$ for both DME and DMEDA) due to interaction with salts but close to the experimental value (0.87 g/cm$^3$ and 0.82 g/cm$^3$ for DME and DMEDA, respectively). For the simulation by pressure and temperature control, the Berendsen barostat was employed. Particle Mesh Ewald (PME) technique was used to treat the long-range electrostatic interaction. The equilibrium systems were confirmed by the constant values of the potential energy and density of the systems. Finally, the MD simulation with NPT ensemble for 100 ns with the time step of 1 fs at 298 K and 1 atm was simulated and the trajectory was recorded for data analysis consisting of the coordination number (CN) and the radial distribution function (RDF) of the probed ions.
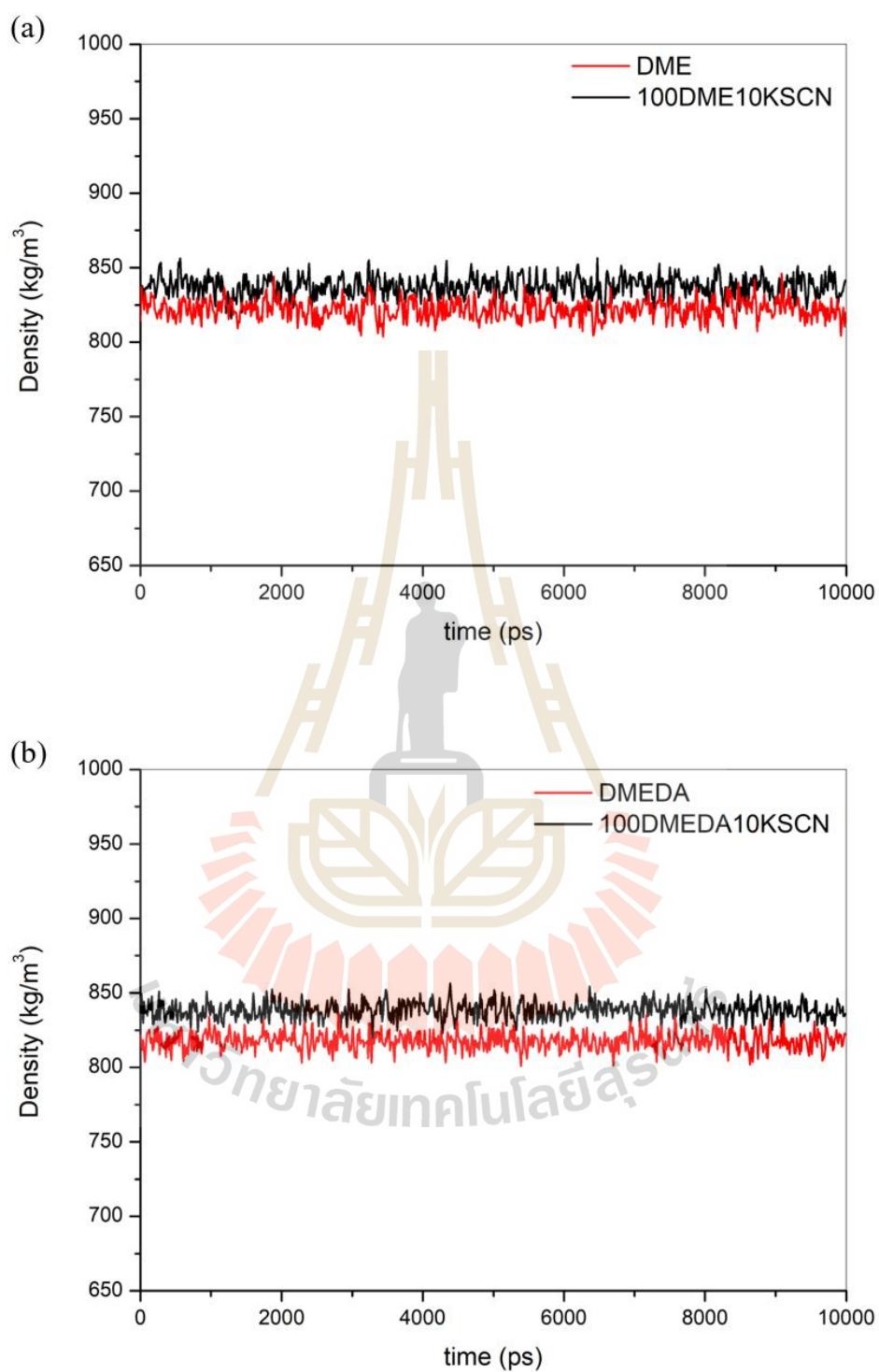
**Figure 3.7** Constant density of the molecule in the box when the simulation time increases for (a) DME and (b) DMEDA.

### 3.4.2 Extended X-ray Absorption Fine Structure (EXAFS) spectroscopy measurements and data analysis

The EXAFS technique details X-rays absorbed by atoms at energy near and above the atom's core binding energy. More specifically, EXAFS is the modulation of the probability of atomic X-ray absorption because of the physical and chemical state of the atoms. EXAFS spectra are particularly relative to the coordination chemistry, the formal oxidation state, and the species, distance, and CN of the atoms immediately surrounding the selected element result in the EXAFS method can provide a way to find the local atomic structure and chemical state of a selected atomistic species. The EXAFS measurement can be used in many systems and bulk physical environments and a wide range of scientific fields, such as material science, catalyst research, biology, and environmental science.

1,2-dimethoxyethane (DME or monoglyme, a 1-mers model compound of PEO) and N,N-dimethyl ethylenediamine (DMEDA) are used as received. KSCN salt is dried in the vacuum oven at about 100-140 °C for 48 hours and then kept in a desiccator. A stoichiometric amount of DME, DMEDA, and the desired KSCN (K:O ratio = 1:20) is dissolved and stirred continuously for 24 h at room temperature until a homogenous solution is formed.

The K-edge EXAFS of the absorbed cation (K from KSCN salt in this case) in samples were measured in the transmission mode at the absorption spectroscopy beamline, Synchrotron Light Research Institute, Thailand. The standard KSCN was used for the energy calibration by setting the K K-edge absorption to 3608.4 eV composed of 6 scans (around 10 min for each). The data were then averaged after $E_0$ determination to improve the signal-to-noise ratio before further analysis.

The EXAFS function $\chi(k)$ is defined as

$$\chi(k) = \frac{\mu(E) - \mu_0(E)}{\Delta\mu_0(E)} \tag{3.21}$$

where $k$ is the photoelectron wave vector given by $k = \sqrt{2E}$. $\mu(E)$ and $\mu_0(E)$ are atomic absorption coefficients for the atom in the material of interest and in the free state, respectively. Here, $\mu(E) = \ln\frac{I_0}{I}$ where I and $I_0$ are the measured incident and

transmitted photon flux. In general, the EXAFS data are usually presented as a function of wave number ($k$) rather than X-ray energy according to the definition:

$$k = \sqrt{\frac{2m(E-E_0)}{h^2}}$$  (3.22)

where $E_0$ is absorption edge energy and $m$ is electron mass.

The raw EXAFS data obtained from the experiment is represented by $\chi(k)$. This function is a waveform pattern with a decrease in its amplitude when the wave number ($k$) increases. To pronounce the data in the high $k$ region, EXAFS spectra are usually multiplied by $k^3$ to show more detailed information at a high $k$ value. The theory of EXAFS is based on the following equation

$$\chi(k) = \sum_j \frac{N_j}{kR_j^2} S_0^2(k) F_j(k) \exp\left(-2k^2\sigma_j^2\right) \exp\left(\frac{-2(R_j-\Delta)}{\lambda}\right) \sin\left[2kR_j+\delta_j(k)\right]$$  (3.23)

where $F(k)$ and $\delta(k)$ are the magnitudes of the backscattering of the neighbor atom and the electronic phase shift due to atomic potentials, respectively. $N$ is the number of neighboring atoms. $R$ and $\sigma^2$ are the mean and variance of the distance between absorbed atoms.

ATHENA software (Ravel, 2005) was used for data analysis including data alignment, background subtraction, normalization, and spline removal, and to convert the measured EXAFS oscillation from $\mu t$ vs E to $k^2\chi(k)$ vs k plot. The EXAFS oscillation was then Fourier Transformed for the k-range 3 - 6 Å$^{-1}$ to provide the radial structure function (RSF). The RSF is similar, but not the same, to the radial distribution function (RDF) because the peak position is shifted from the real distances.

### 3.4.3 MD-EXAFS Analysis

The EXAFS scattering path of the selected snapshots from MD trajectories can be generated by ARTEMIS and FEFF6 (Ravel, 2005). EXAFS spectra were defined using the user-supplied XYZ coordinates (usually from the standard crystal with a similar structure) by including the single and multiple scattering paths. In this work, the EXAFS scattering was generated using the atomic coordinates from MD snapshots of all species that fell within a 7 Å radius of the probed K$^+$ ion. At first, the EXAFS region generated only a single scattering contribution for each atom. Then, the most relevant multiple scatterings within 4.0 Å (the range correlated to the first dominant peak of

EXAFS data) were chosen to fit with the EXAFS spectrum from the experiment. The atomic coordinates were systematically chosen from the MD trajectories (based on the information of the K coordination distance and CN of the solvated atoms) and tested with the EXAFS fitting procedure until the best structure was found.
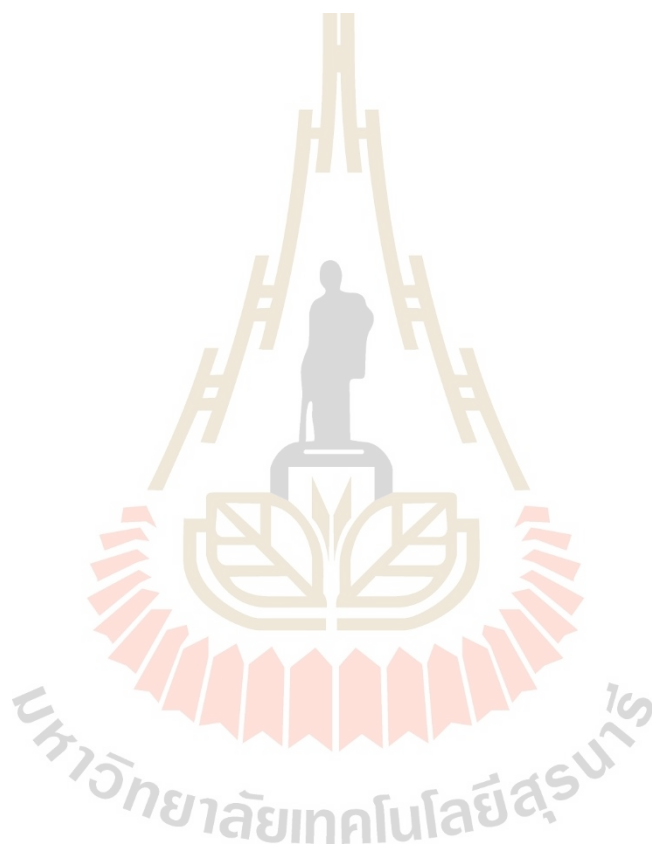
# CHAPTER IV

# RESULTS AND DISCUSSION

## 4.1 The Effect of Adding Molecular Fillers on Polyethylene Oxide-based SPEs

### 4.1.1 Differential Scanning Calorimeter (DSC)

**Isothermal crystallization**

The isothermal crystallization kinetics of PEO and their blends in the temperature range of 48-54°C were investigated and compared. Figure 4.1 presents the isothermal crystallization DSC of the PEO blend with filler samples at different crystallization temperatures. This result shows a decrease in the height of crystallization peaks and an increase in the complete crystallization time as increasing the crystallization temperatures. At the same isothermal crystallization temperature (50°C), the DSC thermograms for all samples are displayed in Figure 4.2. It can be concluded that the crystallization process was shifted to shorter times for the PEO blend with PEG with a molecular weight (Mw) of 20,000 g/mol and urea, indicating that both fillers can accelerate the crystallization process of PEO. In contrast, the crystallization process was slower for fillers that were PEG with Mw of 400 g/mol and mixed Mw of PEG.
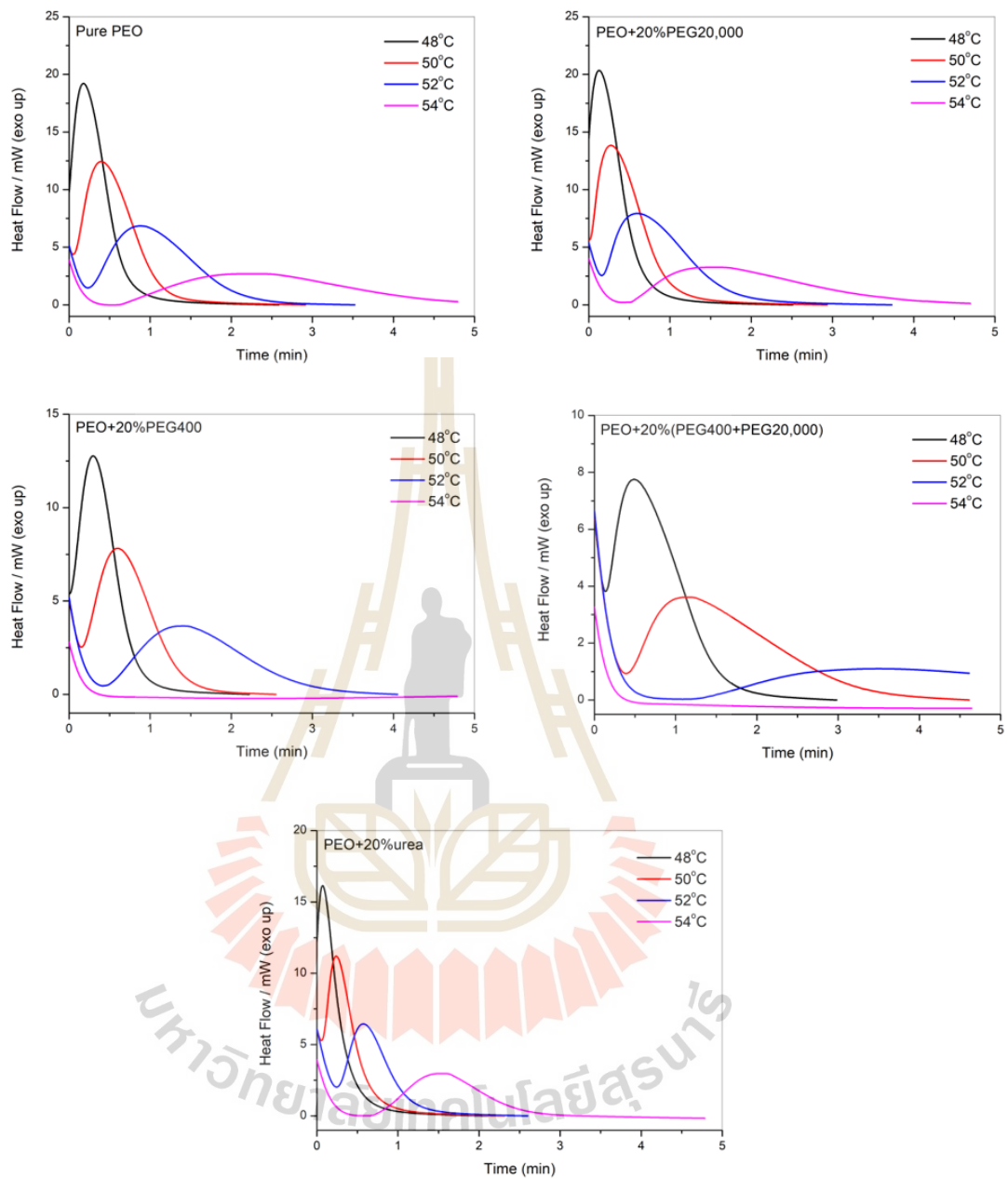
**Figure 4.1** Heat flow as a function of time during isothermal crystallization at different crystallization temperatures (48-54°C).
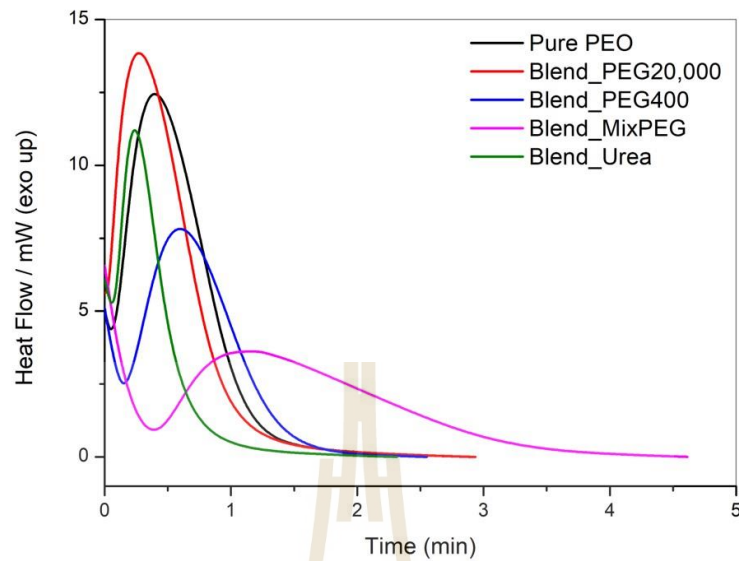
**Figure 4.2** Heat flow as a function of time during isothermal crystallization at 50°C.

In general, Avrami theory has been used to analyze the kinetics of the isothermal crystallization for polymer systems that relate to the degree of crystallinity as a function of time that can be obtained according to

$$\frac{\phi(t)}{\phi^\infty} = 1 - \exp\left[-k\left(t-t_0\right)^n\right] \tag{4.1}$$

$$\log\left[-\ln\left(1-\frac{\phi(t)}{\phi^\infty}\right)\right] = n\log(k) + n\log(t-t_0) \tag{4.2}$$

where $\phi^\infty$ is the degree of crystallinity after the crystallization process is complete. $t_0$ is the induction period for the crystallization, $k$ is the crystallization rate constant that is contributed from the growth of crystal and nucleation, and $n$ is the Avrami exponent which relates to the crystal growth dimension.

Figure 4.3 represents the Avrami plots for PEO and their blends at isothermal crystallization temperature (50°C). This result shows that the Avrami exponent ($n$) for all samples is in the range of 2-3 indicating that the crystal grows in two or three dimensions. Therefore, the inhomogeneous nucleation is obtained.
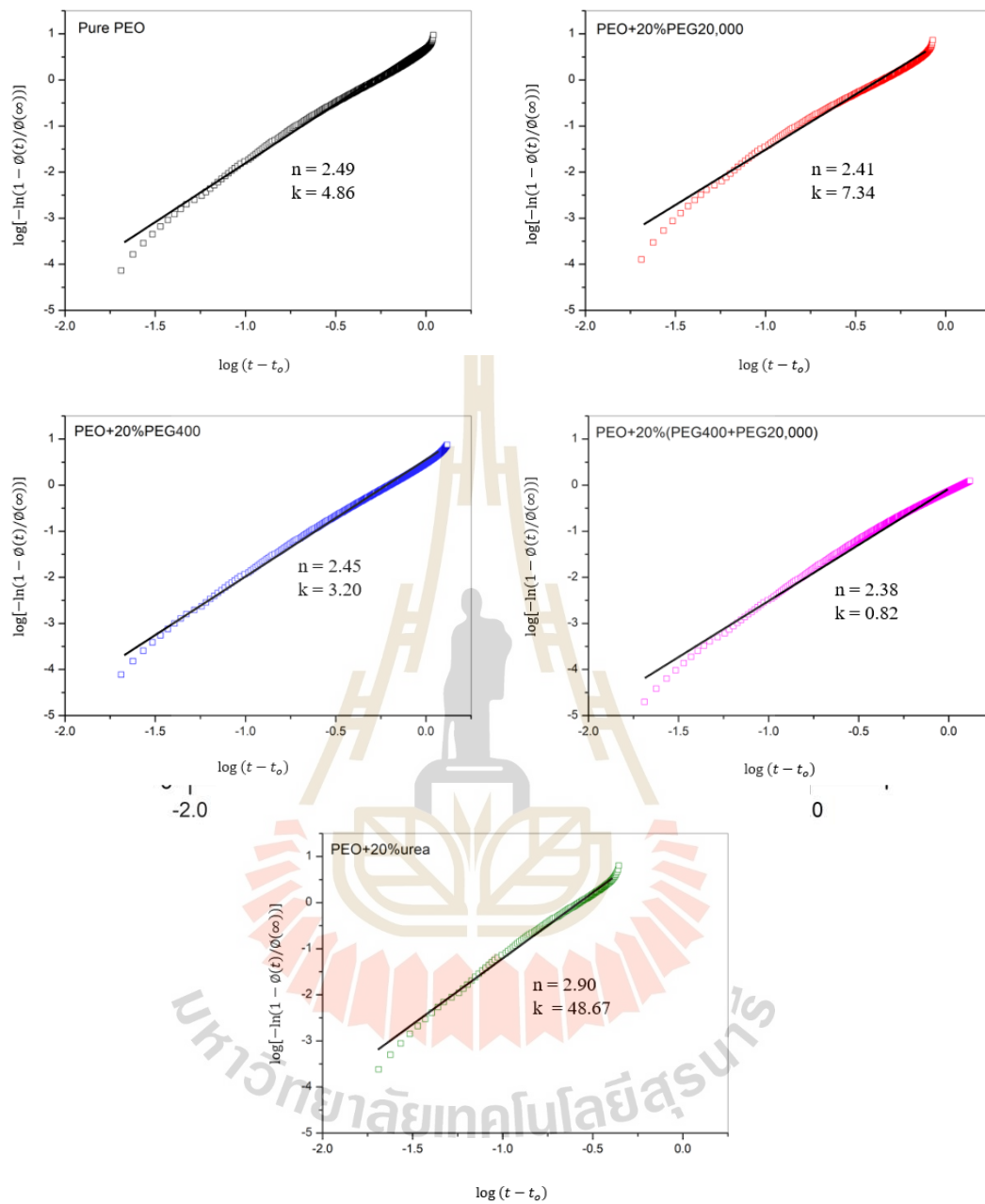
**Figure 4.3** Avrami plots at 50°C based on DSC results for all samples.

**Non-isothermal crystallization**

Continuously changing temperature crystallization is of practical interest (Li, 2014) because most industrial processes are generally performed under non-isothermal conditions. During this process, the crystallization kinetics have been studied by the heat flow as a function of temperature. DSC thermograms in the non-isothermal processes are shown in Figure 4.4 for the PEO and their blends at different cooling rates (5, 10, 20°C/min). At the faster cooling rate, both crystallization peak temperatures ($T_p$) and onset crystallization temperatures ($T_i$) tend to decrease. The relative degree crystallinity as a function of temperature, $X(T)$ with different cooling rates can be calculated as follows (Zeng, 2008):

$$X(T) = \frac{\int_{T_i}^{T} (dH/dT)dT}{\int_{T_i}^{T_\infty} (dH/dT)dT} \tag{4.3}$$

where dH is the crystallization enthalpy during an infinitesimal time interval dT, $T_i$ is the onset crystallization temperature and $T_\infty$ is the complete crystallization temperature. The $X(T)$ as a function of temperature relationship is presented in Figure 4.5. The percent of crystallinity is changed by dependent on the cooling rate for all samples. The temperature of the polymer sample is gradually decreased when the crystallization rate increase. These results suggest that a nucleation stage is slow while a primary crystallization stage is fast with different temperature ranges.
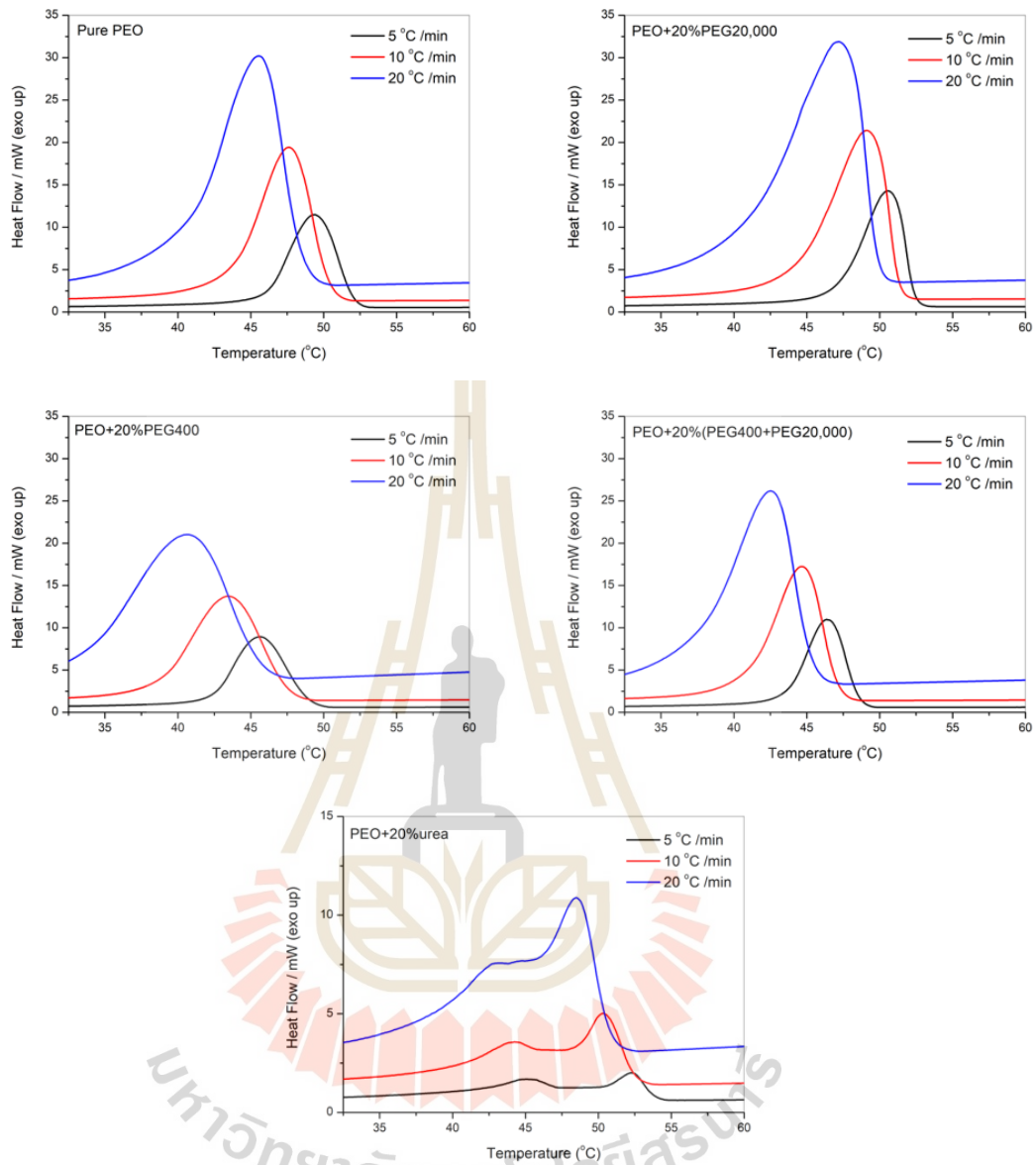
**Figure 4.4** DSC thermograms for non-isothermal melt-crystallization of samples at different cooling rates.
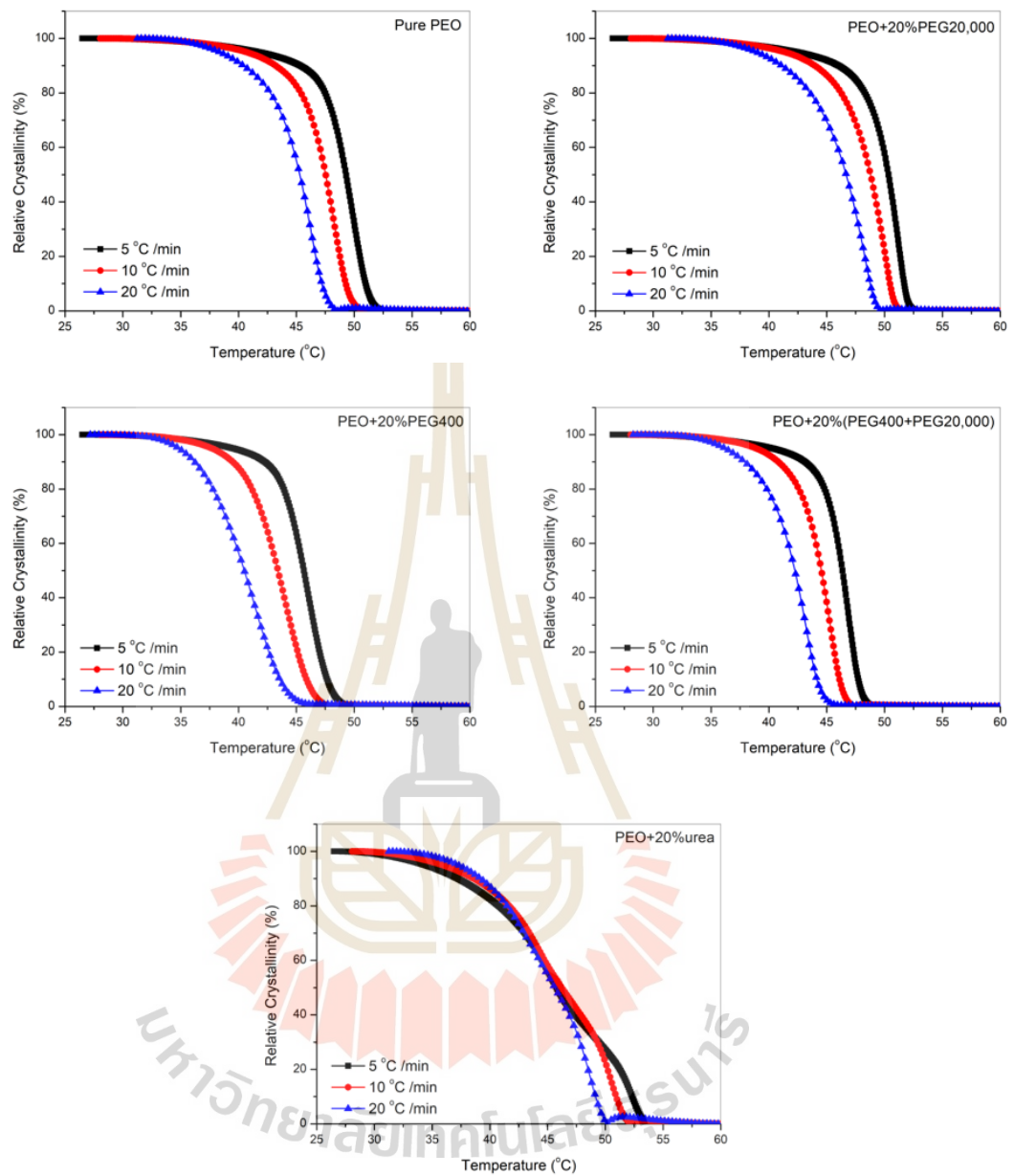
**Figure 4.5** Relative crystallinity versus temperature for samples at different cooling rates.

### 4.1.2  Polarized Optical Microscopy (POM)

Polarized Optical Microscopy is applied to investigate the morphology of the samples and the spherulite growth with time for the isothermal crystallization temperature at 50°C. Figure 4.6 presents the evolution of the spherulite growth processes for PEO. From Figure 4.6, the crystallization process starts quickly and it shows that PEO spherulites grow from the center which is the nuclei, gradually expanding over time. In addition, polarized optical micrographs of the filler-doped PEO samples, as Figure 4.7, were taken during the isothermal crystallization at 50°C. The crystals for the PEO blend urea sample are too small sizes to determine their spherulite growth by optical microscopy. Therefore, only its observable morphology can be represented.

The growth of the spherulite size for the samples is linearly relation to the crystallization time. The spherulite radius is changed with crystallization time, indicating the crystal growth process is dominated by nucleation. The crystalline growth rates of samples versus the crystallization temperature are represented in Figure 4.8. It indicates that the growth rate become slower for adding fillers that were PEG with Mw of 400 g/mol and mixed Mw of PEG. While the PEG filler with a Mw of 20000 g/mol increased the spherulite growth rate compared to pure PEO, this result is consistent with the data from isothermal crystallization DSC.
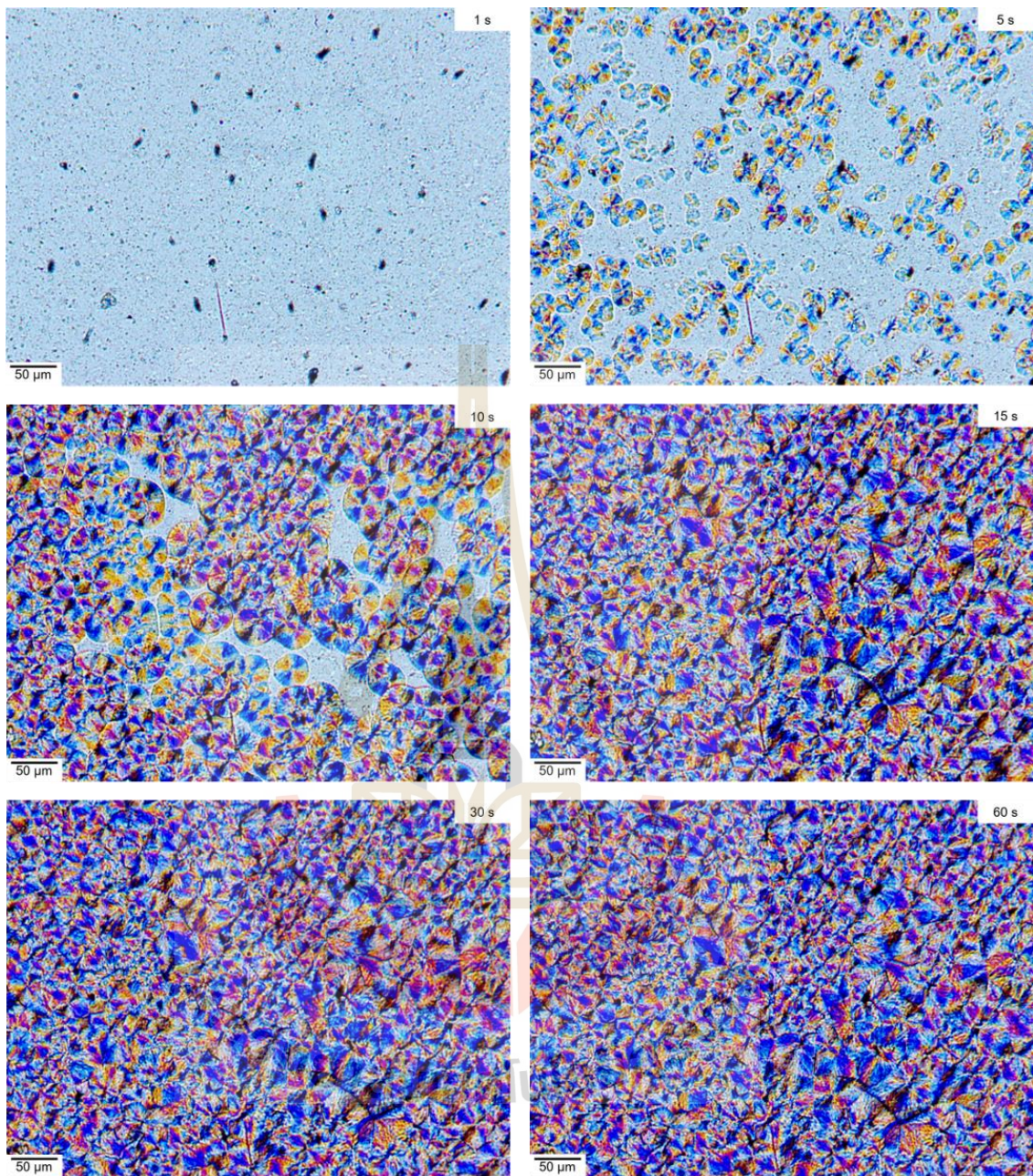
**Figure 4.6** Polarized optical micrographs as a function of time of PEO sample taken during the isothermal crystallization at 50°C.
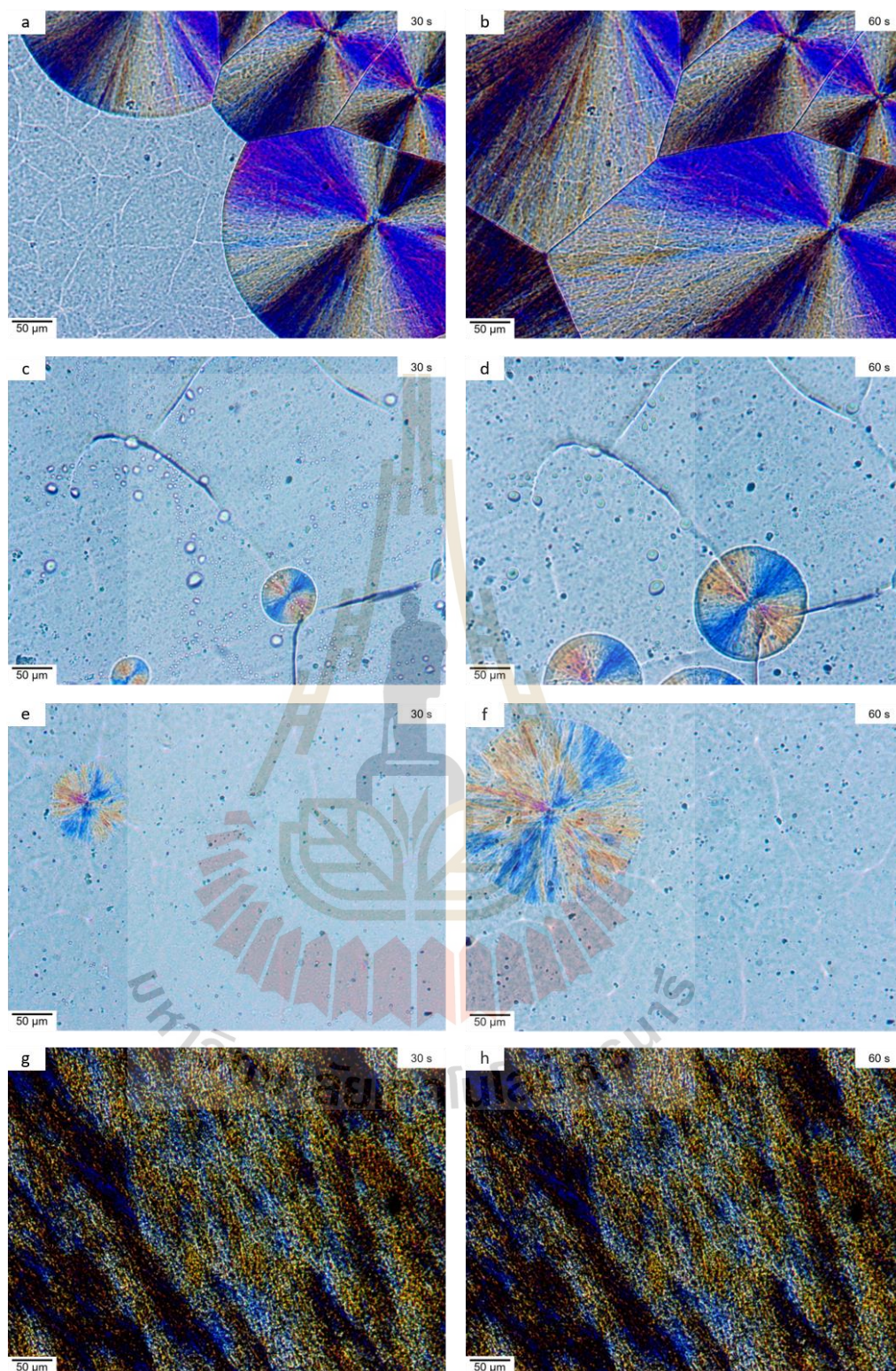
**Figure 4.7** Polarized optical micrographs of (a)-(b): PEO/PEG20,000, (c)-(d): PEO/PEG400, (e)-(f): PEO/MixPEG and (g)-(h): PEO/urea taken during the isothermal crystallization at 50°C at a different time (30 s and 60 s).
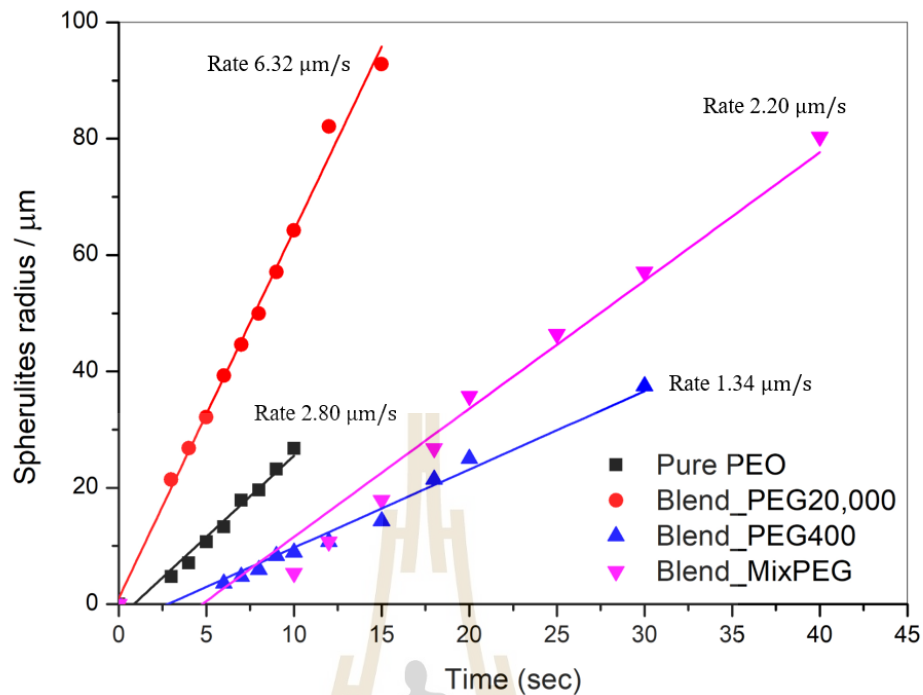
**Figure 4.8** The linear relationship between the spherulite radius and the crystallization time for samples determined from POM.

### 4.1.3 Small Angle X-ray Scattering (SAXS)

To study the morphology of polymer, the SAXS profile is corrected for beam intensity, sample transmission, and background scattering and then converted to Lorentz corrected SAXS profile by multiplying by $q^2$ (Vonk, 1967). The scattering vectors are defined as (Glatter, 1982):

$$q = (4\pi/\lambda)\sin\theta \tag{4.4}$$

Here, $q$ denotes the magnitude of the scattering vector, $\lambda$ is the wavelength of the X-ray and $\theta$ is the scattering angle. The SAXS profiles ($I(q)$ vs. $q$) for all samples are depicted in Figure 4.9 and the Lorentz-corrected SAXS profiles ($q^2I(q)$ vs. $q$) are presented in Figure 4.10. The SAXS data is collected in the range of $q$ = 0.15 nm$^{-1}$ to 2.55 nm$^{-1}$. The maximum peak intensities are at $q$ = 0.25 nm$^{-1}$ for pure PEO and $q$ = 0.32 nm$^{-1}$ for PEO blend urea. The location of the SAXS peak moves toward higher $q$ as the crystallization proceeds. On the other hand, PEG fillers increase the crystal size of PEO and therefore is not show a peak. This result is constant with the POM data.
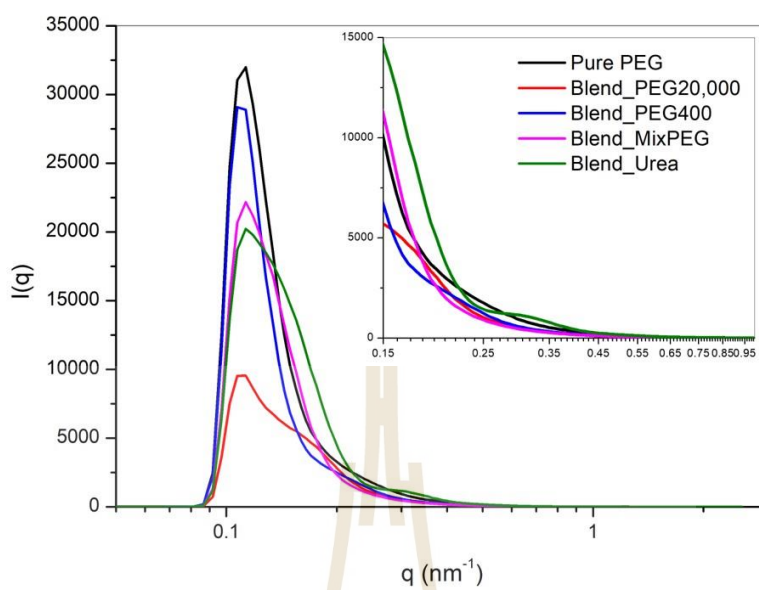
**Figure 4.9** The SAXS profiles (I(q) vs. q) for all samples at room temperature.
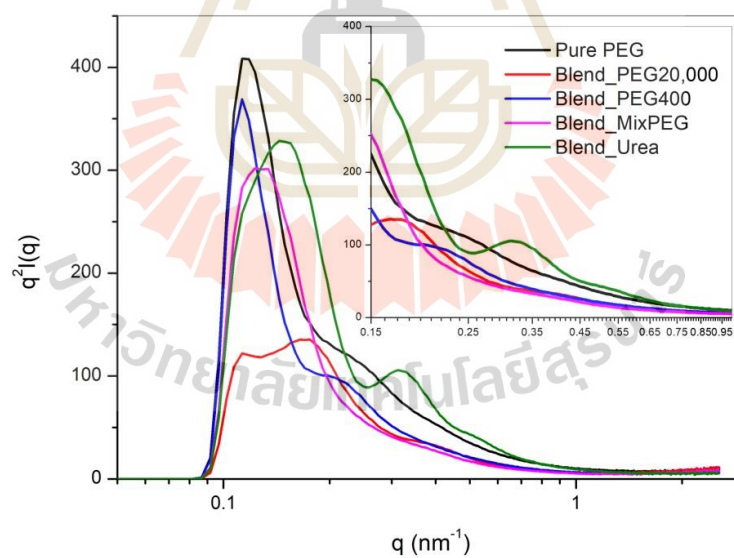


**Figure 4.10** The Lorentz-corrected SAXS profiles ($q^2 I(q)$ vs. q) for all samples at room temperature.

## 4.2 Molecular Simulation for the Effect of Chain Stiffness on Polymer Crystallization from the Melts

### 4.2.1 Equilibration

The intra- and intermolecular energies for PE chains upon stepwise cooling at each temperature: 473 K (0-10 x $10^6$ MCS), 400 K (10-20 x $10^6$ MCS), 350 K (20-30 x $10^6$ MCS) and 298 K (30-90 x $10^6$ MCS) are depicted in Figure 4.11. For PE-like models, chains can be regarded as more flexible chains ($k < 1.0$) and stiffer chains ($k > 1.0$) than normal PE ($k = 1.0$). The average intra- (interchain) energies at 298 K during 50-90 million MCS for $k$ = 0.5, 0.75, 1.0, 1.25 and 1.5 at 298 K are 2868.3$\pm$53.1 (-6317.5$\pm$50.6), 1763.2 $\pm$50.4 (-6945.2$\pm$50.6), 1653.4$\pm$50.9 (-6799.3$\pm$52.4), 1555.6$\pm$42.3 (-6721.0$\pm$38.0) and 1777.5$\pm$36.9 (-6362.9$\pm$30.5) kJ/mol, respectively.

At lower temperatures, polymers can be converted to more *trans* conformation resulted in lower intrachain energies. In addition, the interchain energies tend to be decreased as chains can move closer to each other. More flexible chains with lower stiffness parameters tend to have higher intramolecular energies due to a larger amount of *gauche* fraction. Exception for the stiffest chains ($k$ = 1.5), the conversion from *gauche* conformation to the *trans* state is too difficult and as a result the intramolecular energies for the stiffest chains are still high even at 298 K. Furthermore, the interchain energies for chains with $k$ = 0.5 and 1.5 are significantly higher suggesting the ordered structures at lower temperatures may be less densely packed as chains are too flexible or too stiff, respectively.
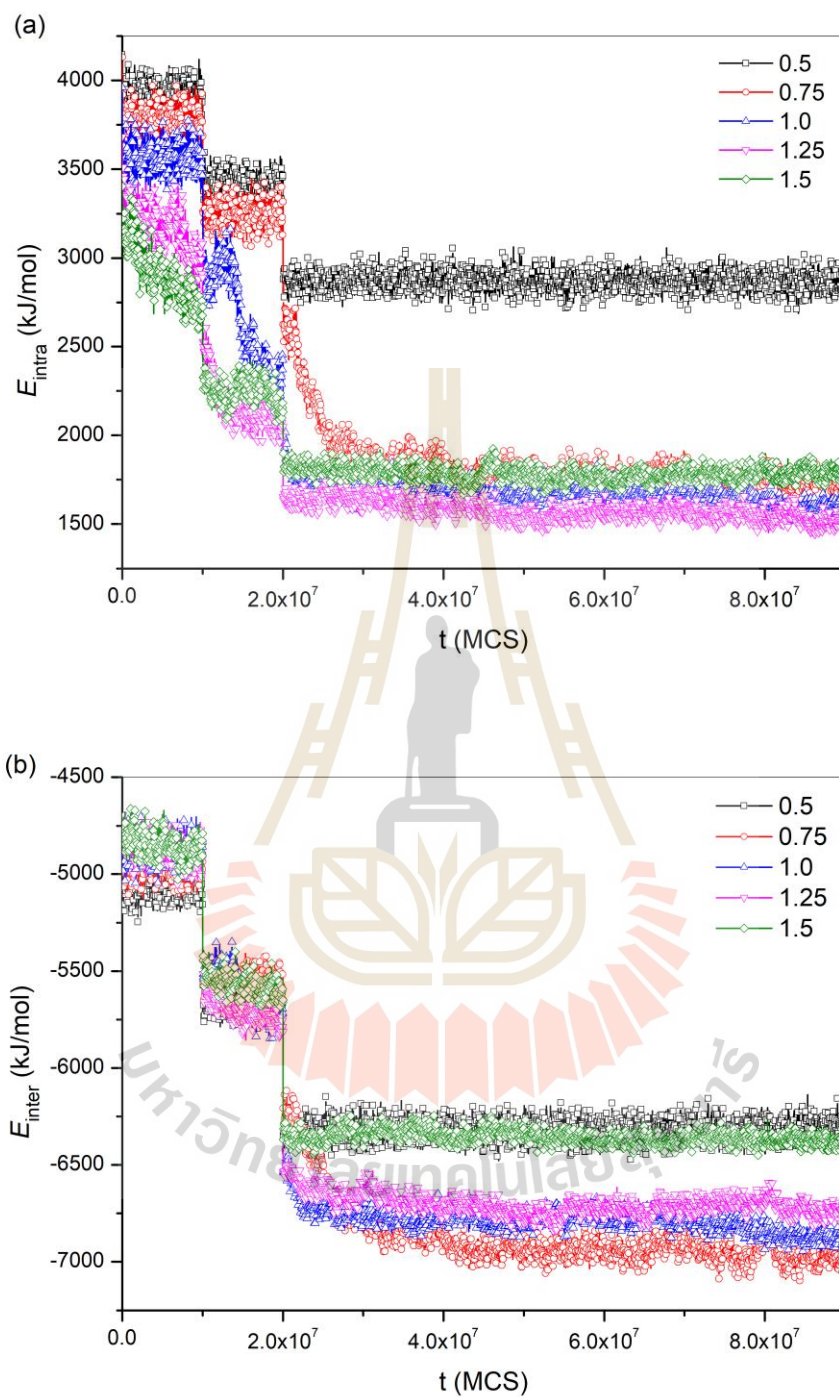
**Figure 4.11** The (a) intrachain energies ($E_{intra}$) and (b) interchain energies ($E_{inter}$) of PE-like models with different chain stiffness parameters.

The dynamic properties of polymers can be evaluated from the orientational auto-correlation function (OACF) of the normalized end-to-end vector, $<R(t).R(0)>/(R^2)$ and the mean square displacement (MSD) for the chain center of mass, $g_{cm}(t) = <[R_{cm}(t)-R_{cm}(0)]^2>$ where $R(t)/R(0)$ and $R_{cm}(t)/R_{cm}(0)$ are the end-to-end vector and the center of the mass of polymer chains at time $t/0$, respectively. Figure 4.12(a) shows the OACFs of the normalized end-to-end vector at 298 K which indicate that the more flexible chains tend to relax faster. From the MSD plots in Figure 4.12(b), the scaling exponents at 298 K are proportional to $t^{1.00}/t^{0.61}/t^{0.59}/t^{0.51}/t^{0.46}$ in the sub-diffusive regime and $t^{0.97}/t^{0.86}/t^{0.68}/t^{0.63}/t^{0.91}$ in the long-time limit for chains with $k = 0.5/0.75/1.0/1.25/1.5$, respectively. In general, the scaling exponents tend to be larger for more flexible chains. The scaling exponents of most systems are below 1 indicating the non-Fickian behavior at 298 K.

The local dynamics at the level of monomer units at 298 K are determined as the MSD of individual beads and presented in Figure 4.12(c). As expected, beads in the more flexible chains move faster. In addition, the dynamics increase exponentially for the beads near the chain ends. Note that the MC technique with this PE model exhibit the dynamic properties comparable to those of the MD simulation of all atomic models or experiments with real systems as discussed previously (Xu, 2002).
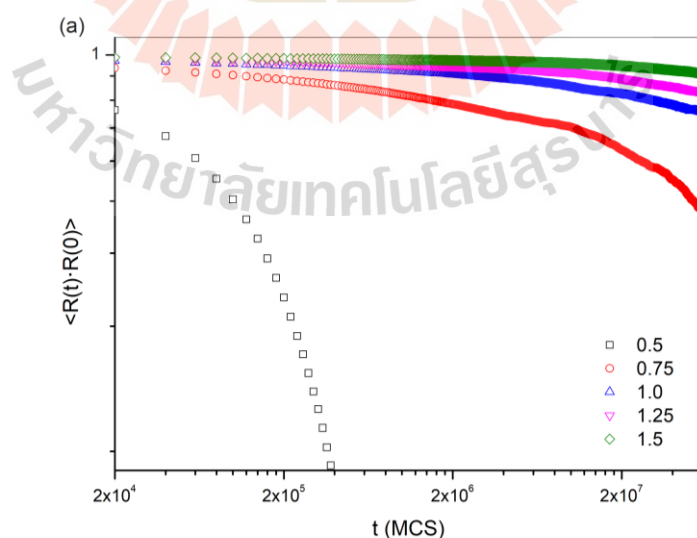


**Figure 4.12** (a) The orientational auto-correlation functions, the mean square displacements of (b) polymer chains and (c) individual beads of *PE-like* chains with different stiffness parameters ($0.5 < k < 1.5$) at 298 K.
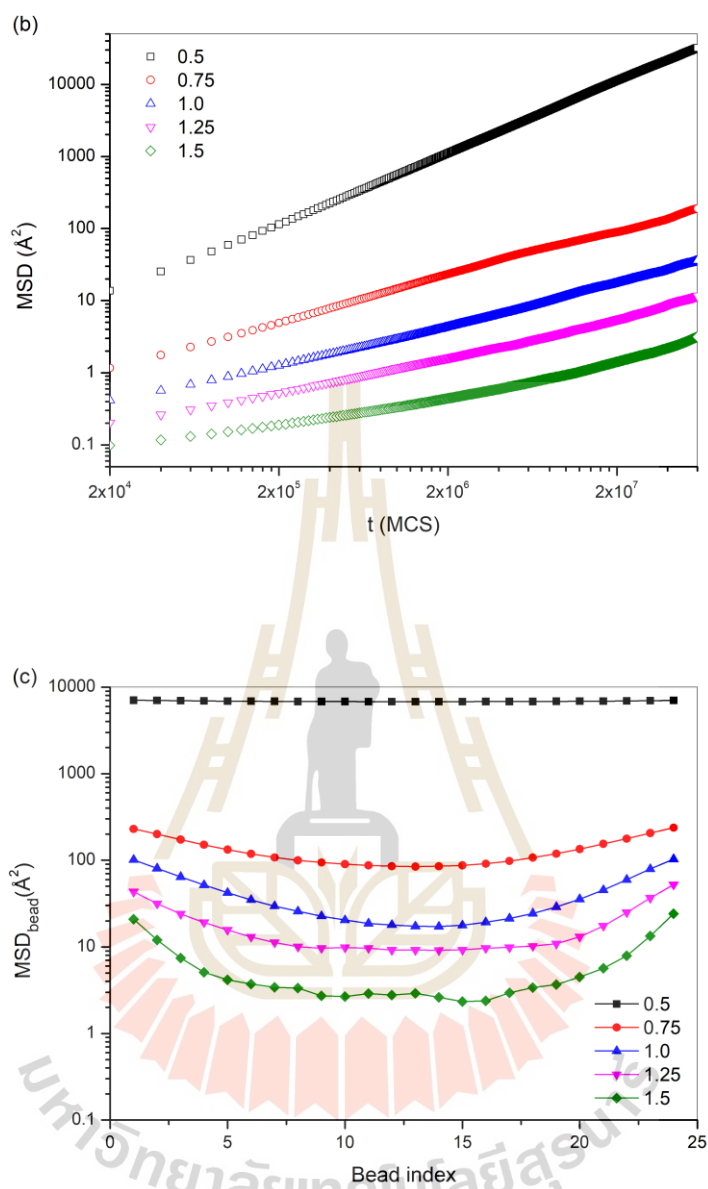
**Figure 4.12** (Continued) (a) The orientational auto-correlation functions, the mean square displacements of (b) polymer chains and (c) individual beads of *PE-like* chains with different stiffness parameters (0.5 < *k* < 1.5) at 298 K.

Figure 4.13 depicts the final snapshots at the end of trajectories at 298 K for each polymer system. Chains still can adopt the *gauche* conformation especially in the case of the most flexible and the stiffest chains (k = 0.5 and 1.5 respectively) while other systems have similar structures but can be oriented in different direction.
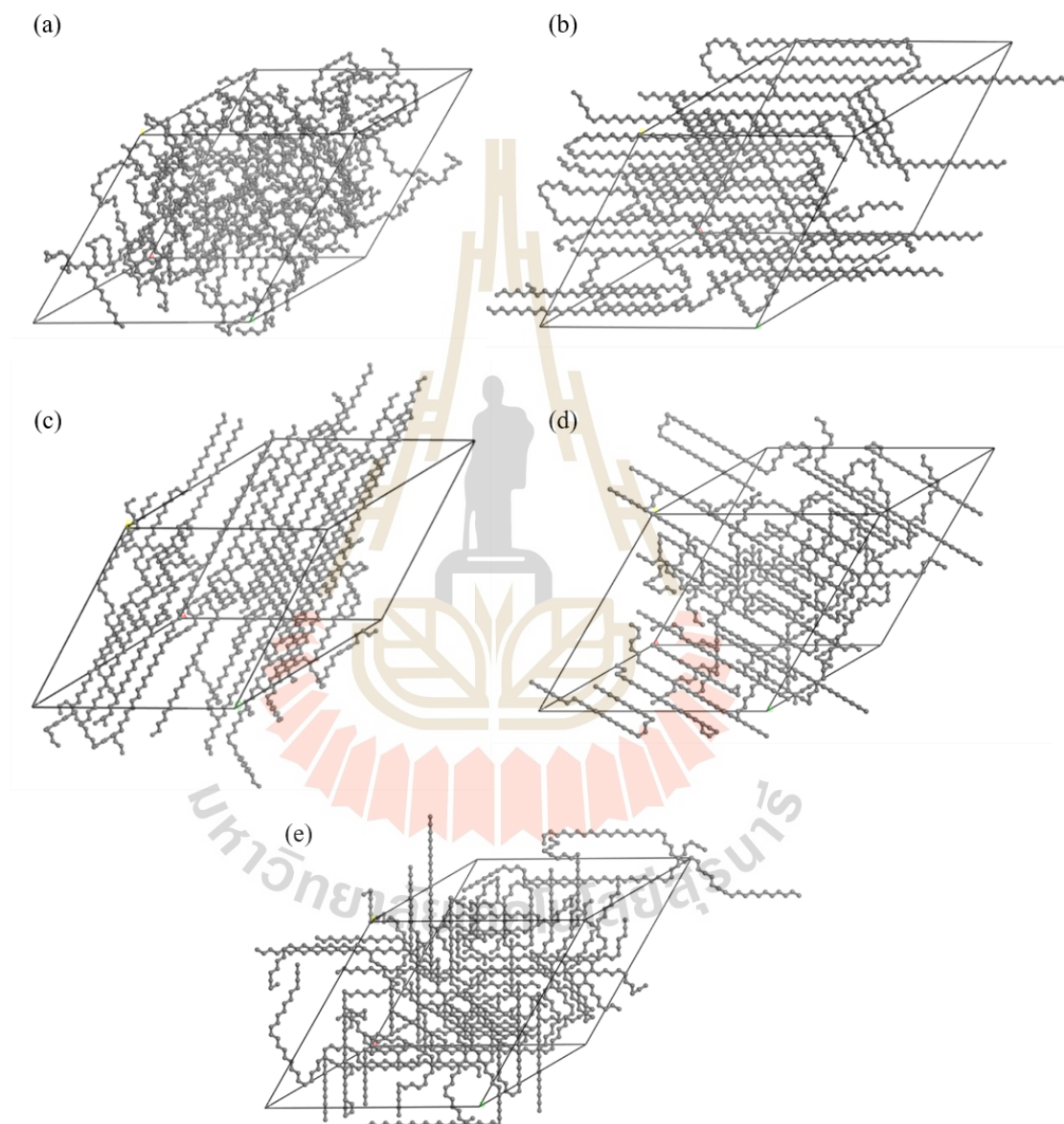


**Figure 4.13** The final structures of polymer models at 298 K with different stiffness parameters, *k* = (a) 0.5, (b) 0.75, (c) 1.0, (d) 1.25 and (e) 1.5.

### 4.2.2 Conformation

The evolution of the *trans* state upon step-wise cooling from the melts at each temperature is shown in Figure 4.14. At 473 K, the *trans* fractions have the lowest magnitudes and then steadily increases at lower temperature. At 298 K, the *trans* fractions, averaged after 50 million MCS, reach 0.54 ± 0.01, 0.82 ± 0.01, 0.83 ± 0.01, 0.84 ± 0.01 and 0.81 ± 0.01 for the polymer chains with $k$ = 0.5, 0.75, 0.1, 1.25 and 1.5, respectively. In general, the magnitudes of *trans* fraction in stiffer chains are relatively larger except for the stiffest chains ($k$ = 1.5) as they have the most difficulty to convert the *gauche* conformation to the *trans* state at 298 K. The growth and magnitude of the *trans* fraction can be seen at shorter MCS (higher temperature) for the chains with $k$ in the order as: 0.5 (no steep growth) < 0.75 (298 K) < 1.25 (350 K) $\leq$ 1.0 (350 K) < 1.5 (473 K).
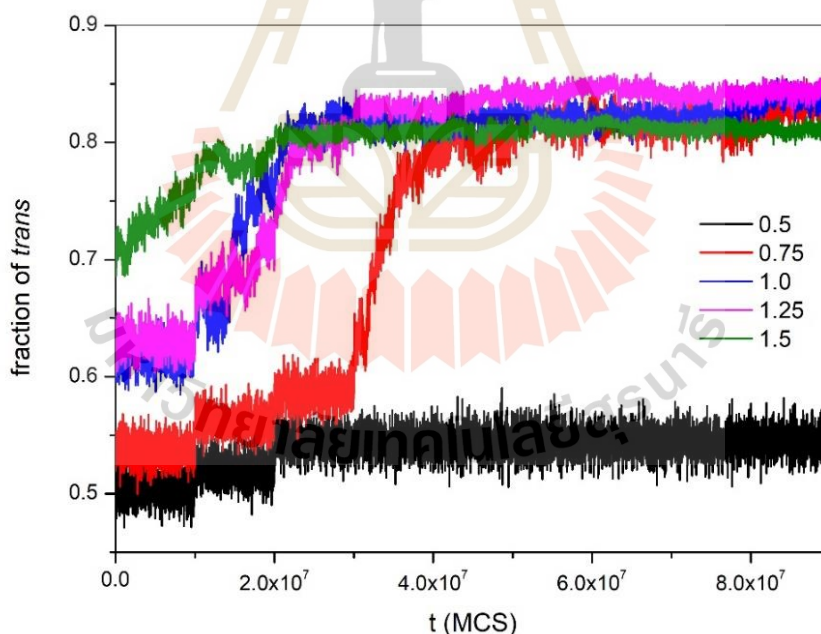


**Figure 4.14** The *trans* fraction of polymers with different chain stiffness parameters.

### 4.2.3  Chain dimension

Molecular dimensions can be represented by the mean square radius of gyrations, $<R_g^2>$, of polymer chains and are depicted in Figure 4.15. At high temperatures near the melts (400 K and 473 K), $<R_g^2>$ are quite constant and their magnitudes are larger for stiffer chains. Then, chain dimensions start to increase at 350 K (20 - 40 million MCS) for most systems except the case for the most flexible chain ($k$ = 0.5). Molecular dimension at 298 K for the chains with $k$ = 0.75 < $k$ < 1.25 are almost the same as normal PE ($k$ = 1.0). For too flexible or too stiff chains ($k$ = 1.5 and 0.5, respectively), they exhibit quite smaller magnitudes. These results indicate that only polymers with the appropriate chain stiffness can induce the large amount of *trans* conformation upon step-wise cooling from the melts.
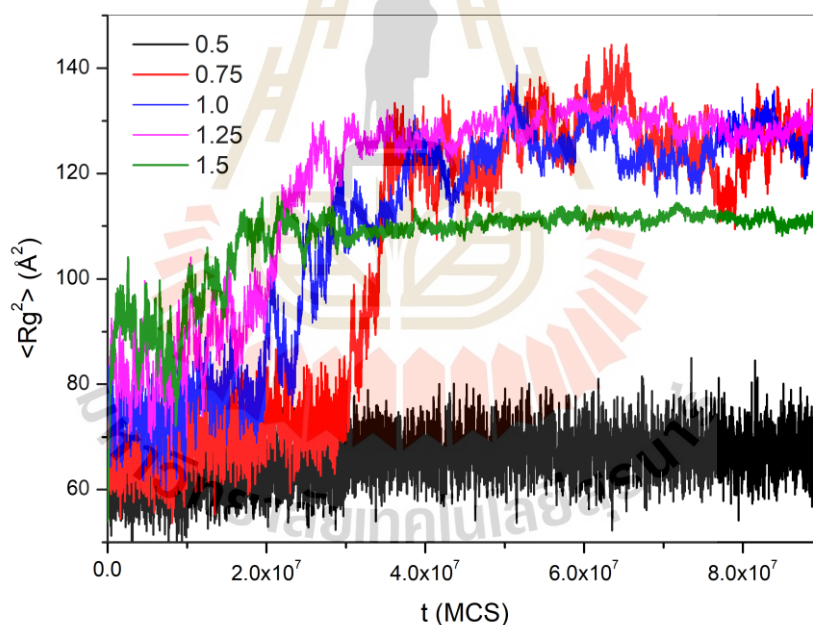


**Figure 4.15** The mean square radius of gyration of polymers with different chain stiffness parameters.

### 4.2.4 Molecular orientation

To evaluate the molecular orientation as the sign of polymer crystallization, the overall orientation order parameter, $S_G$, is determined by

$$S_G = \frac{1}{2}[3\langle\cos^2\theta\rangle\text{-}1] \tag{4.5}$$

Here, polymer chain can be represented as an equivalent ellipsoid with three main axes ($L_3 < L_2 < L_1$) determined from the diagonalization of the radius of the gyration tensor. The largest main ($L_1$) axis was selected to represent polymer orientation where the angle ($\theta$) is measured between two $L_1$ of different chains. Perfectly parallel and random orientation are related to $S_G$ = 1 and 0, respectively.

Form Figure 4.16, $S_G$ of both the most flexible and the stiffest chains (k = 0.5 and 1.5) are about 0.0 throughout simulation trajectories indicating that these polymer systems always have random orientation and cannot be crystallized. For the normal PE chain ($k$ = 1.0), $S_G$ is increased earlier (at 15 million MCS or 350 K) than the chains with $k$ = 1.25 and 0.75 (increase around 20 and 30 million MCS, respectively). However, PE chains with $k$ = 0.75 extend the highest magnitude of $S_G$ at the final stage. These results suggest that more flexible chains generally crystallize slower but can exhibit a higher amplitude of chain orientation.

As inferred from both Figure 1.14 and 1.16, the initial rates of molecular elongation and chain orientation are faster for polymer systems with $k$ equal or close to 1.0 because of the greater proportion of the length of the *trans* sequences. Nevertheless, the more flexible chains ($k$ = 0.75) can exhibit more anisotropy of molecular orientation at the late stage.
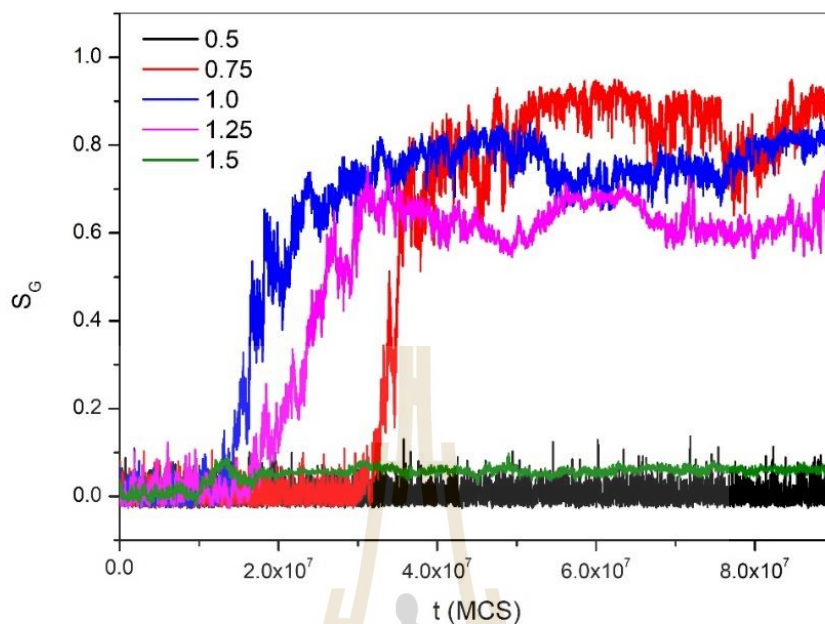
**Figure 4.16** The evolution of the chain orientation for polymer systems with different chain stiffness parameters.

When *PE-like* chains crystallize, they should adopt more *trans* fraction and the intramolecular bond correlation should be higher. To quantify the bond orientation within the same chain, the first order intramolecular bond order parameter, $M_1(j)$ is determined by

$$M_1(j) = <m_i.m_{i+j}> = < cos\ \theta_{i,i+j} > \tag{4.6}$$

Here, $\theta_{i,i+j}$ is the angle between $i$th and ($i+j$)th bonds in the same polymer chain. Figure 4.17 shows the behavior of $M_1(j)$ for bonds at 298 K. $M_1(j)$ evaluates the bond orientation which usually determined as a function of the bond index ($j$). At 298 K, $M_1(j)$ should drop slowly as polymer chains have a large fraction of *trans* state. For *PE-like* chains with $0.75 < k < 1.25$, they exhibit similar profiles for $M_1(j)$ up to $j = 10$ bonds whiles the most flexible and the stiffest chains ($k = 0.5$ and $1.5$) can decay faster because these chains have larger amount of *gauche* conformation than other systems. $M_1(j)$ for the most flexible chains drops to 0 or random orientation for $j > 7$ bonds. Compared for all polymer system at $j > 10$ bonds, the magnitudes of $M_1(j)$, which are the sign of anisotropy for intramolecular bond arrangement, can be ordered for $k$ of

1.0 < 0.75 < 1.25 < 1.5 < 0.5. These results imply that the anisotropy of bond orientation is related to the appropriate chain stiffness parameter. If the chains are too flexible or too stiff, the bonds tend to be oriented in the more disordered fashion.

To investigate the correlation for bond orientation in different chains, the local ($S_L$) intermolecular bond orientation order can be calculated as

$$S_L(n) = \frac{1}{2}[3<\cos^2 \psi(n)>-1] \tag{4.7}$$

where $\psi(n)$ is the angle for two bonds separated in the $n$th shell from *2nnd* lattice. Figure 4.18 depicts $S_L$ for each polymer system with different chain stiffness parameters at 298 K. In general, $S_L$ is close to zero or random orientation in the first shell while it exhibits the highest anisotropic orientation in the second shell. For further shell number, $S_L$ is decrease monotonically indicating that the more separated bonds become more isotropic orientation. The magnitude of $S_L$ for each polymer system with different stiffness parameter are 0.75 > 1.0 ≥ 1.25 >> 1.5 > 0.5. Large $S_L$ values (high bond correlation) are seen for the normal PE chains ($k$ = 1.0) and those with $k$ = 0.75 and 1.25. Again, if the chains have excessive stiffness or flexibility, the intermolecular bonds tend to be more isotropic orientation.
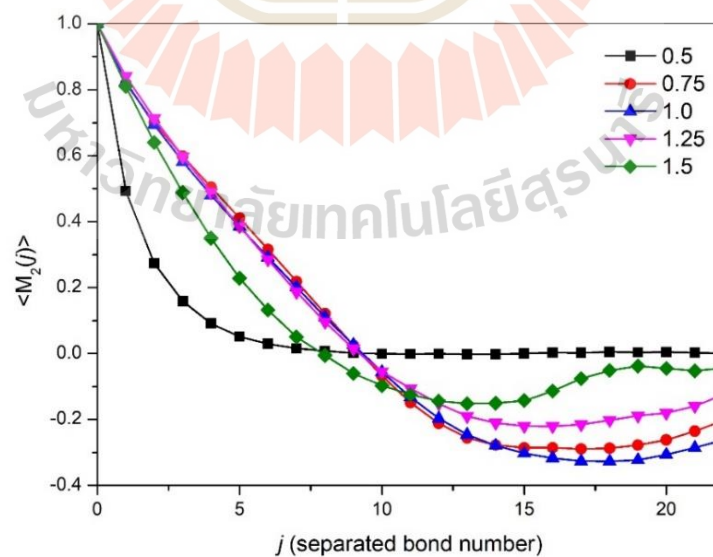


**Figure 4.17** Intramolecular bond orientation correlation functions for polymer systems with different chain stiffness parameters.
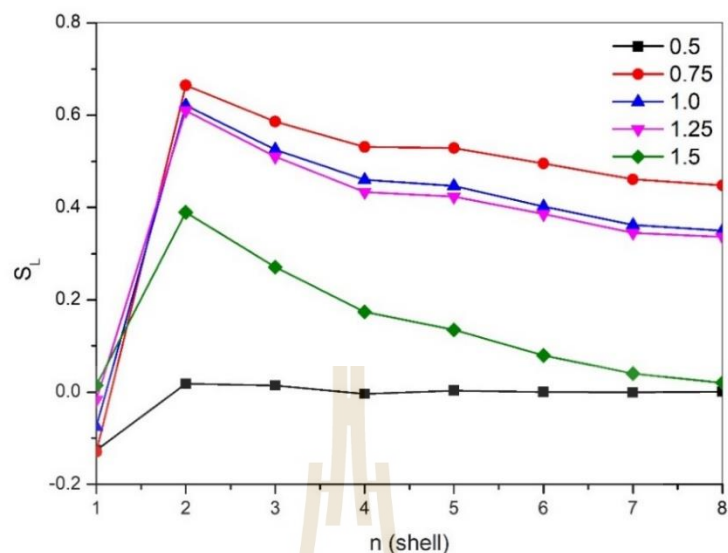
**Figure 4.18** Intermolecular bond orientation correlation function for polymer systems with different chain stiffness parameters.

### 4.2.5 Chain packing

The intermolecular pair correlation function (PCF), used to represent the chain packing, can be calculated in term of the probability to find two CG beads at the separated shells on the *2nnd* lattice as

$$g_{AA}(i) = \frac{\langle n_{AA}(i) \rangle}{(10i^2 + 2)V_A} \tag{4.8}$$

where, $n_{AA}(i)$ is a number of CG beads at the $i$th shell from the reference bead; $V_A$ is the volume fraction of CG beads. Figure 4.19 presents the PCFs for the PE chains with different chain stiffness parameters. The PCFs reach the highest values at the $3^{rd}$ shell because of the most attractive intermolecular interaction and then become lower for the further shells. The PCF can be generally ordered for the PE-like systems with $k$ as: $0.75 > 1.0 > 1.25 > 1.5 \geq 0.5$. These data suggest that the more flexible chains generally can better stay close to neighboring chains. If the chains are too flexible ($k = 0.5$) or too stiff ($k = 1.5$), the chains cannot be packed well compared to the case of $0.75 < k < 1.25$.
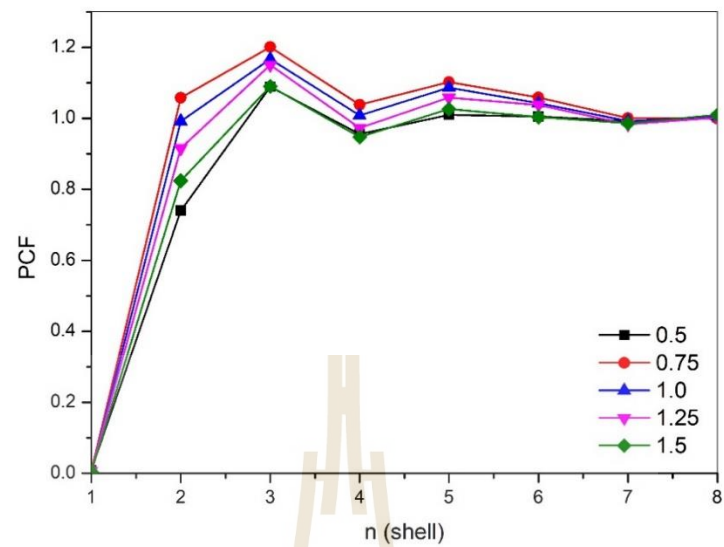
**Figure 4.19** The intermolecular pair correlation function for the *PE-like* chains with different chain stiffness.

## 4.3 Multiscale Simulation for Molecular and Material Properties of Perfluoro- and Normal Poly(ethylene oxide) Melts

### 4.3.1 Structural equilibrium

Structural relaxation and system equilibration of polymer chains are judged by the orientation autocorrelation functions (OACF), $\langle \vec{R}(t) \cdot \vec{R}(0) \rangle$, where $\vec{R}(t)$ and $\vec{R}(0)$ are the end-to-end vector at time $t$ and $0$, respectively; and the angle bracket means the ensemble average . As depicted in Figure 4.20(a), the OACF decays from 1 to almost 0 within 90 million MCS. Moreover, the equilibration is obtained by the mean square displacement of the chain center of the mass (MSD) defined as: $g_{cm} = \langle |(r_{cm}(t) - r_{cm}(0)|^2 \rangle$ where $r_{cm}(t)$ and $r_{cm}(0)$ are the coordinates of the chain center of the mass at time $t$ and $0$, respectively. In general, polymer chains are fully relaxed from their initial conformations when the MSDs are larger than their molecular dimension *i.e.,* about two times the root mean square radius of gyration of polymer chains ($2\langle R_g^2 \rangle^{1/2}$). As seen in Figure 4.20(b), the MSD exceeds the molecular dimension (25.8 and 25.9 nm for PF-PEO and N-PEO, respectively) within 90 million MCS. The local dynamics at the monomer unit level are determined as the MSD of individual beads and presented in Figure 4.20(c). Beads in the N-PEO chains move faster than PF-PEO chains. In addition, the dynamics increase exponentially for the beads near the chain ends. Based on these results, the PF-PEO system is fully relaxed slower than the N-PEO system. The PF-PEO model seems to be more rigid to fully equilibrate than the N-PEO model.

According to the behavior of MSD and OACF, the bulk PF-PEO and N-PEO models should be completely equilibrated. Thus, selected final structures from each MC simulation on the lattice were used for the reverse mapping procedures to the fully atomistic PF-PEO and N-PEO models. The final structures for the CG model before the reverse mapping and the fully atomistic model of PF-PEO and N-PEO after geometry optimization are shown in Figure 4.21.
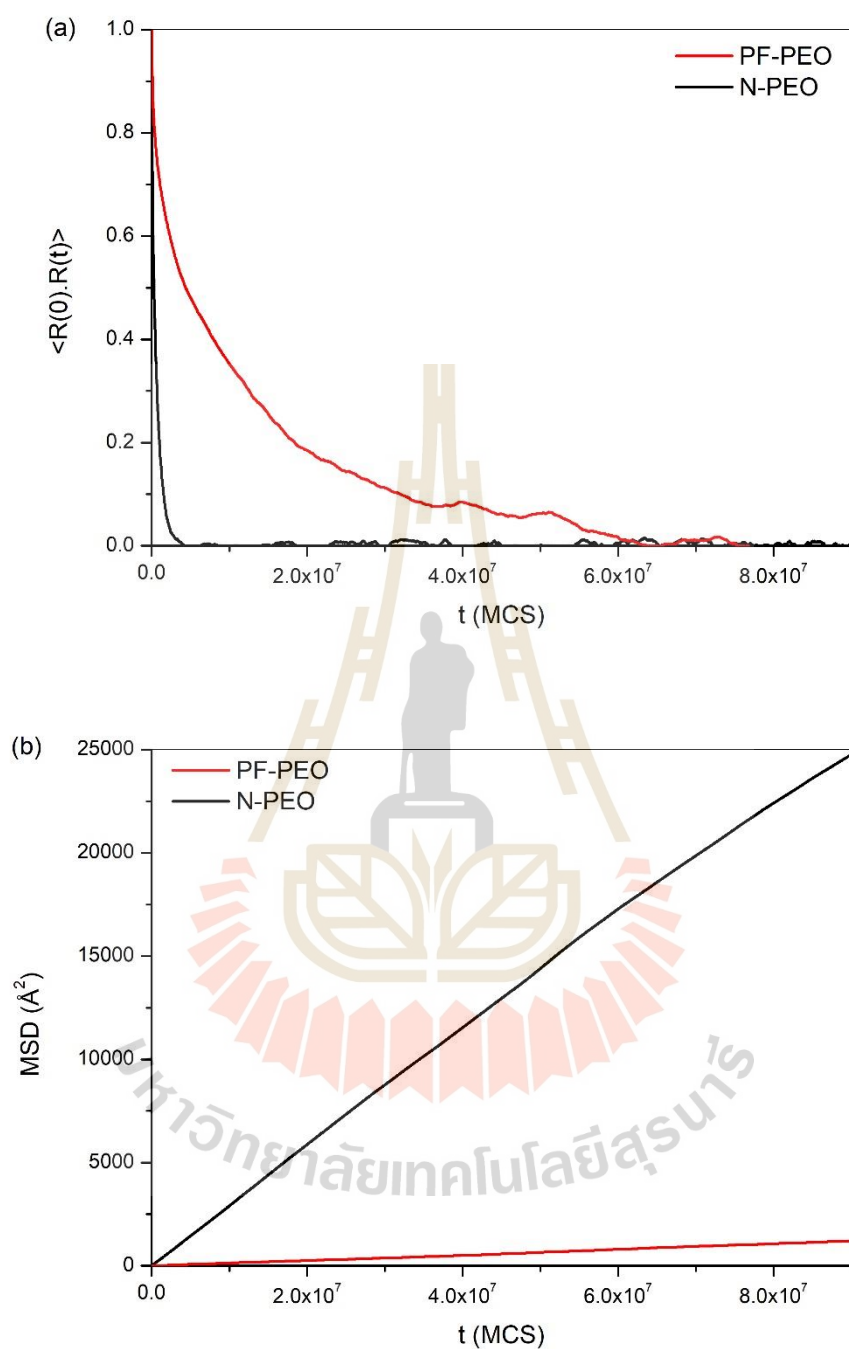
**Figure 4.20** (a) The orientation autocorrelation functions (OACF) of the end-to-end vector, (b) the mean-square displacement for the chain center of mass, and (c) the individual beads of PF-PEO and N-PEO chains.
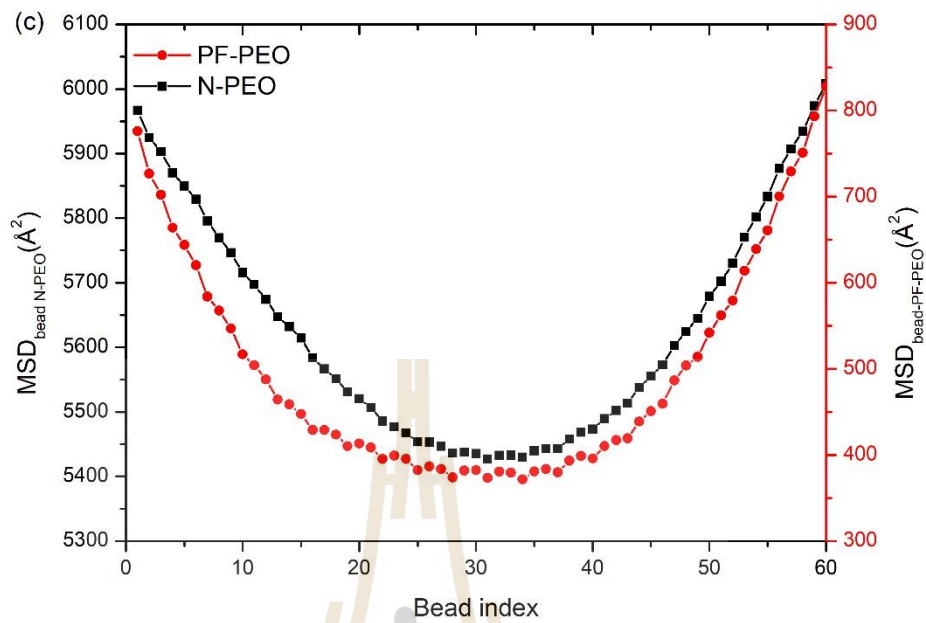
**Figure 4.20** (Continued) (a) The orientation autocorrelation functions (OACF) of the end-to-end vector, (b) the mean-square displacement for the chain center of mass, and (c) the individual beads of PF-PEO and N-PEO chains.

(a)
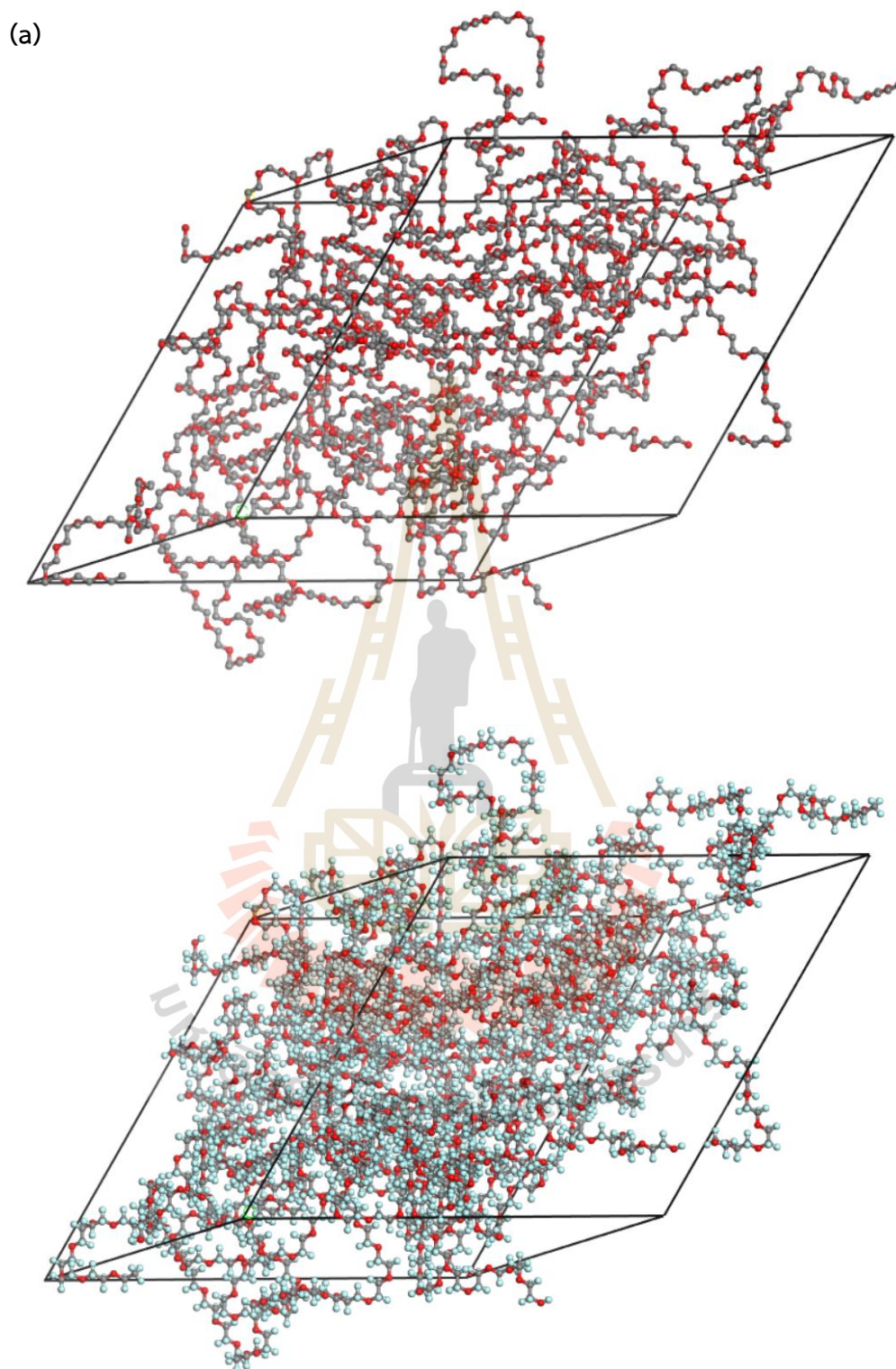


**Figure 4.21** Example of the snapshot of coarse-grained and fully atomistic (a) PF-PEO and (b) N-PEO models.

(b)
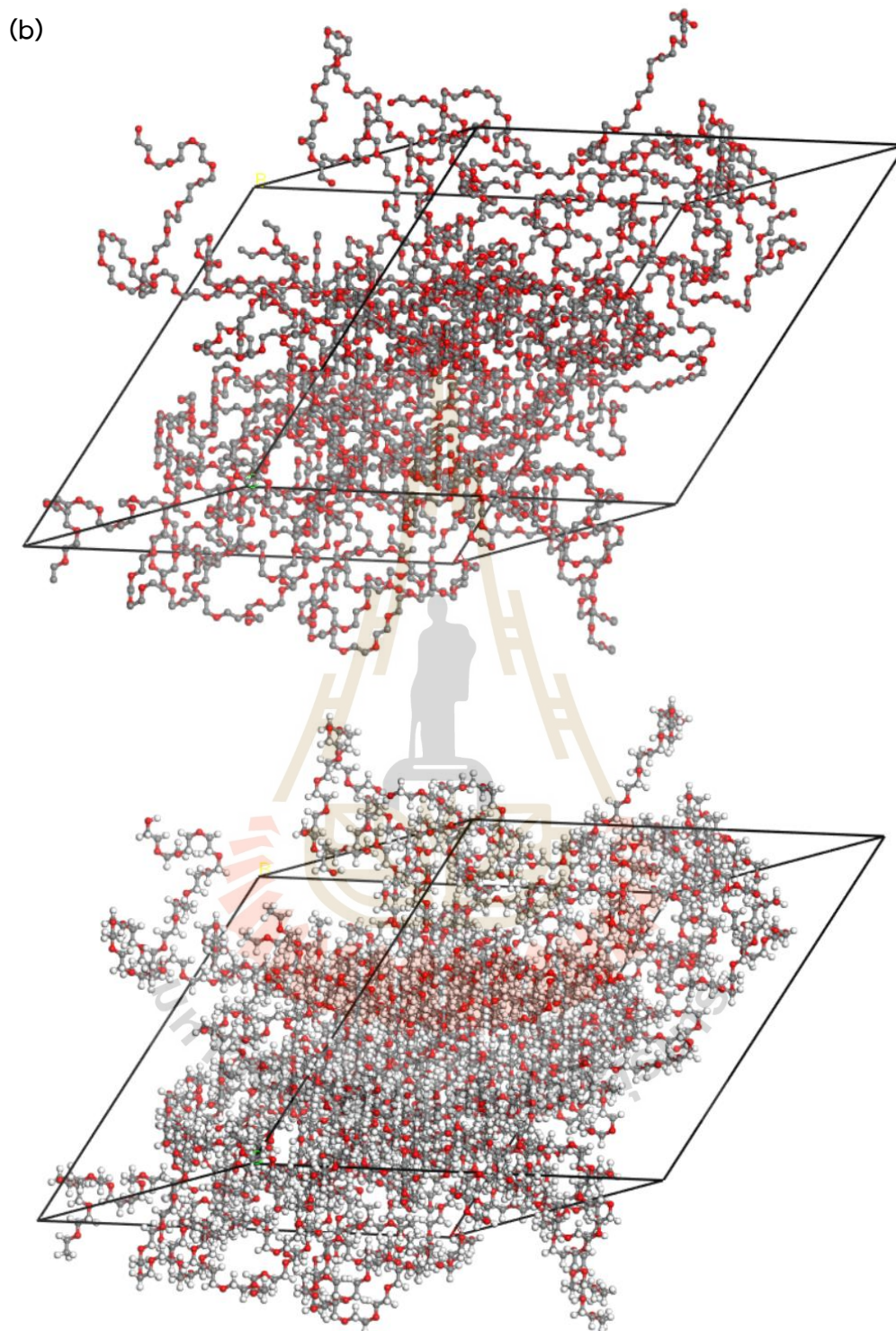


**Figure 4.21** (Continued) Example of the snapshot of coarse-grained and fully atomistic
(a) PF-PEO and (b) N-PEO models.

### 4.3.2 Chain dimension

Molecular dimension can be determined in terms of the root mean square end-to-end distance, $<R_E^2>^{1/2}$, and the root mean square radius of gyration, $<R_g^2>^{1/2}$, and results are presented in Table 4.1. Many parameters for PF-PEO and N-PEO become larger as most atoms can be displaced to off-lattice positions after reverse mapping with geometry optimization through energy minimization followed by structural refinement with 1 ns NVT-MD simulation. The overall shape for the coarse-grained model of PF-PEO chains is slightly smaller than N-PEO but larger on the fully atomistic chain because of the restoration of larger atoms in the reverse-mapping step. The simulation ratio of $<R_E^2>/<R_g^2>$ for coarse-grained PF-PEO and N-PEO are very close to the theoretical Gaussian model where $<R_E^2>/<R_g^2>$ approaches 6 for sufficient long-chain limit (Flory, 1969).

**Table 4.1** The root mean square end-to-end distance ($<R_E^2>^{1/2}$), The root mean square radius of gyration ($<R_g^2>^{1/2}$) and $<R_E^2>/<R_g^2>$ ratio of PF-PEO (N-PEO) models.

| Chain properties | Coarse-grained model[a] | Fully atomistic model[b] |
|---|---|---|
| $<R_E^2>^{1/2}$ (nm) | 31.02 ± 27.03 (32.21 ± 27.80) | 35.79 ± 12.35 (32.39 ± 11.09) |
| $<R_g^2>^{1/2}$ (nm) | 12.90 ± 8.30 (12.97 ± 8.56) | 14.32 ± 1.04 (12.84 ± 0.79) |
| $<R_E^2>/<R_g^2>$ | 5.78 (6.17) | 4.27 (4.60) |

[a] On-lattice structure of the Coarse-grained model

[b] Geometry optimization of the fully atomistic model (energy minimization + NVT-MD simulation)

### 4.3.3 Conformational statistics

The conformational state in the chain of polymer is usually determined via values of the torsional angles. Before the reverse mapping, the conformations of CC-OC, CO-CC, and OC-CO bonds are limited to the discrete states at $g+$, $t$, and $g-$ ($60^\circ$, $180^\circ$, and $300^\circ$), because of the diamond lattice. In the geometry optimization, the torsional angles are displaced from lattice sites and conformational distribution becomes continuous. The distribution of three different types of dihedrals along the main chain are presented and compared between CG and fully atomistic model of PF-PEO and N-PEO are presented in Figure 4.22 and the population for each conformation state are determined and listed in Table 4.2.

For the CG model at the bulk density during the reverse-mapping step before geometry optimization, the oxygen *gauche* effect is seen in the OC-CO conformation (the population is determined from the integrated areas after energy minimization of the fully atomistic model), especially in PF-PEO. After geometry optimization, the torsional angles around all these bonds of PF-PEO and N-PEO prefer the *trans* conformation.
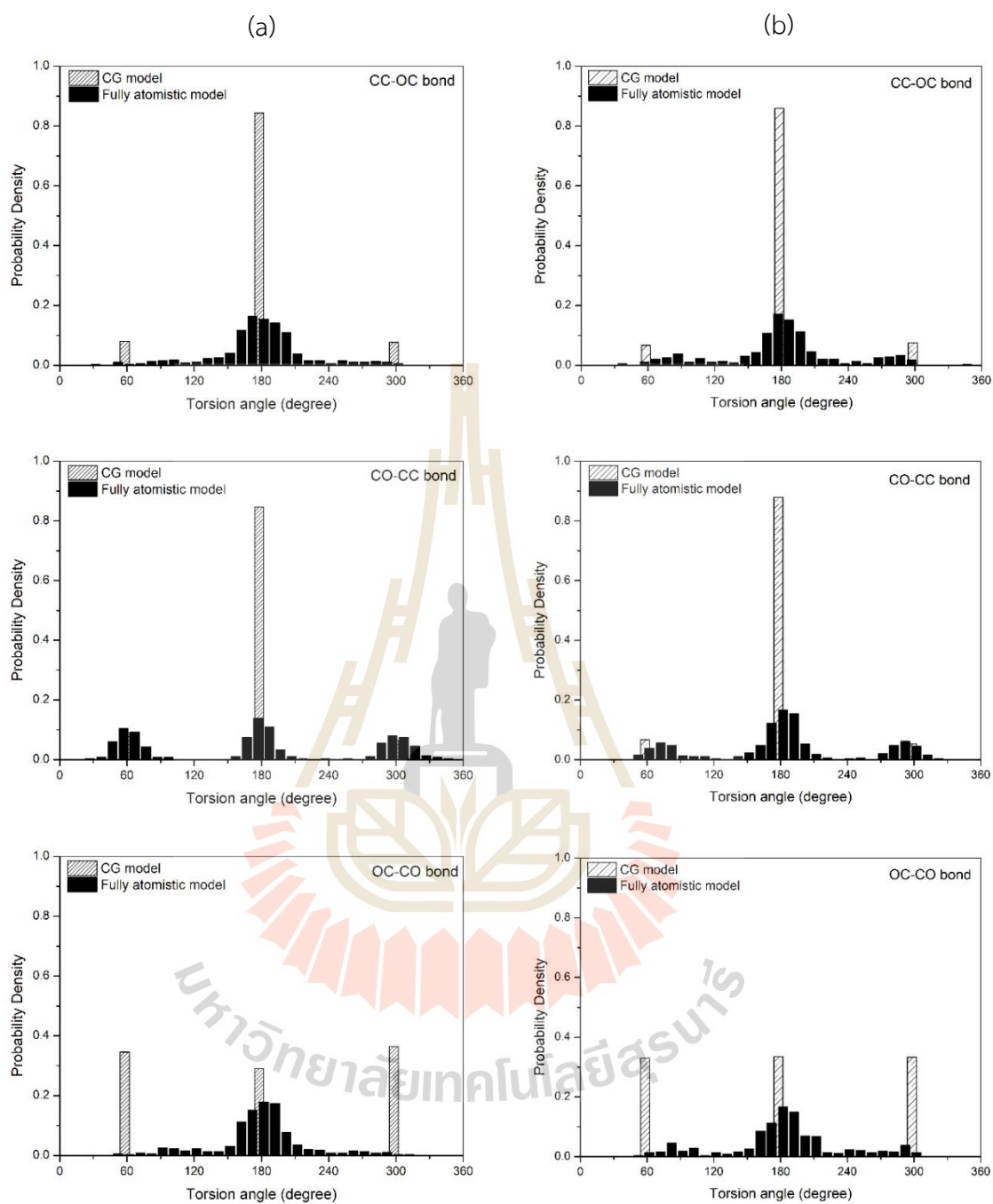
**Figure 4.22** Population of the backbone torsional angles for the CG and fully atomistic (a) PF-PEO and (b) N-PEO models at the bulk density during the reverse-mapping step before and after geometry optimization.

**Table 4.2** Population of the conformational states for PF-PEO and N-PEO models.

| Systems | Bond | CG model | | | Fully atomistic model | | |
|---|---|---|---|---|---|---|---|
| | | $g^+$ | $t$ | $g^-$ | $g^+$ | $t$ | $g^-$ |
| PF-PEO | CC-OC | 0.08 | 0.84 | 0.08 | 0.08 | 0.85 | 0.06 |
| | CO-CC | 0.09 | 0.85 | 0.06 | 0.33 | 0.38 | 0.29 |
| | OC-CO | 0.35 | 0.29 | 0.36 | 0.11 | 0.83 | 0.06 |
| N-PEO | CC-OC | 0.07 | 0.86 | 0.07 | 0.16 | 0.73 | 0.11 |
| | CO-CC | 0.07 | 0.88 | 0.05 | 0.19 | 0.61 | 0.20 |
| | OC-CO | 0.33 | 0.34 | 0.33 | 0.14 | 0.74 | 0.12 |

### 4.3.4   Solubility parameters

The Hildebrand's solubility parameter ($\delta$) can be calculated from the fully atomistic model based on the square root of the cohesive energy density as

$$\delta = (CED)^{1/2} = \left[\frac{U_{coh}}{V}\right]^{1/2} \tag{4.9}$$

where $V$ is the simulation box volume. The difference between the total energy of the model in the periodic box and that of the parent chains can be used to estimate $U_{coh}$, which is the cohesive energy. After reverse-mapping and energy minimization, the fully atomistic PF-PEO and N-PEO models' Hildebrand solubility parameters at the bulk density are $16.75 \pm 0.01$ $J^{1/2}/cm^{3/2}$ and $20.65 \pm 0.01$ $J^{1/2}/cm^{3/2}$, respectively. The experimental solubility parameter for N-PEO is 20.0 $J^{1/2}/cm^{3/2}$ which is close to our calculated value (Table 4.3). In addition, the solubility parameter of PF-PEO is smaller than that of N-PEO. In general, the calculated solubility parameters are quite sensitive to the quality of the forcefield used in the calculation of the atomistic model, especially the non-bonded interaction. Nevertheless, the calculated values from N-PEO models are very close to the experimental data.

**Table 4.3** Hildebrand solubility parameter of PF-PEO and N-PEO models.

| Polymer | Model | Cohesive Energy Density (J/cm$^3$) | Solubility parameter ((J/cm$^3$)$^{1/2}$) |
|---------|-------|-----------------------------------|-------------------------------------------|
| PF-PEO | Smith model | $2.81 \times 10^8 \pm 2.62 \times 10^5$ | $16.75 \pm 0.01$ |
| | Experiment | - | - |
| N-PEO | Smith model | $4.26 \times 10^8 \pm 4.47 \times 10^5$ | $20.65 \pm 0.01$ |
| | Experiment | - | 20.0 |

### 4.3.5 Structures

The radial distribution function (RDF), often known as $g(r)$, is a concept that can be used to characterize the structure of amorphous polymers. The static relationship of each given atom pair AB is averaged out to create the RDF.

$$g_{AB}(r) = \frac{\langle n_{AB}(r) \rangle}{4\pi r^2 \Delta r \rho_{AB}} \tag{4.10}$$

where $\langle n_{AB}(r) \rangle$ is the average number of atom pairs in the spherical shell between the distance $r$ and $r + \Delta r$, and $\rho_{AB}$ is the density of AB atom pairs. By definition, RDF gives the probability of finding the atom pairs that are separated at the distance $r$, normalized by the probability for a uniform distribution at the same density. The RDF function can be represented by total, inter-, and intramolecular components. The intra- and intermolecular RDF gives information about polymer conformation and molecular arrangement in the amorphous structure, respectively.

PF-PEO and N-PEO contain three different atomic species (C, O, and F or H). The intermolecular radial distribution function for three different pairs of elements (C⋯C, O⋯O, and C⋯O) for PF-PEO and PEO were calculated and shown in Figure 4.23. The RDF for these different pairs exhibits the first peak occurs between 4 and 6 Å indicating the nearest neighbor chain packing. The results suggest that N-PEO has a denser structure and decreased chain dimension than PF-PEO due to the smaller size of hydrogen compared to fluorine atoms.
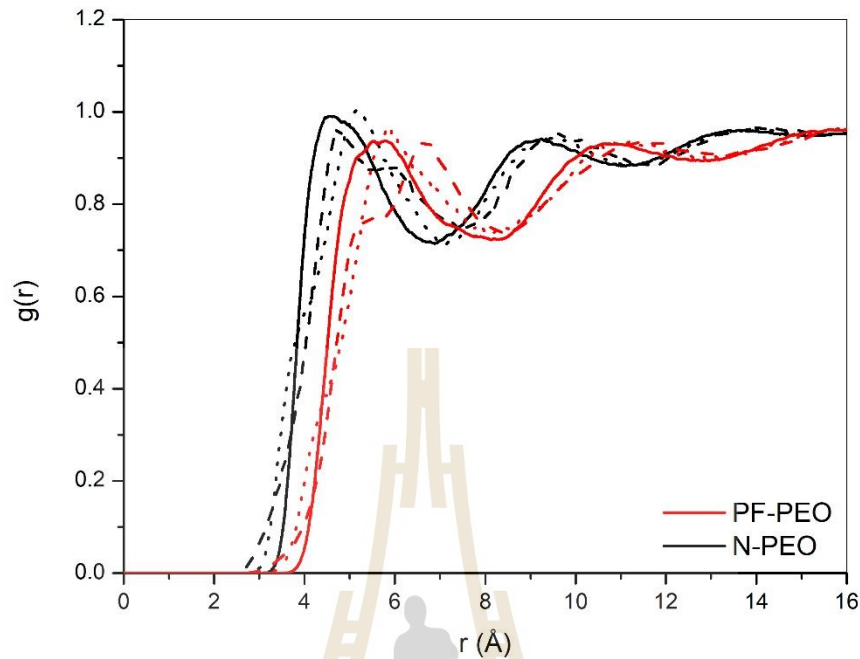
**Figure 4.23** The intermolecular radial distribution function for different pairs of elements (——) C⋯C, (-----) O⋯O and (⋯⋯) C⋯O for the atomistic PF-PEO and N-PEO model.

### 4.3.6 Chain packing

The intermolecular pair correlation function (PCF), used to represent the chain packing, can be calculated in terms of the probability of finding two CG beads at the separated shells on the *2nnd* lattice as

$$g_{AA}(i) = \frac{<n_{AA}(i)>}{(10i^2+2)V_A} \tag{4.11}$$

where, $n_{AA}(i)$ is the number of CG beads at the $i$th shell from the reference bead; $V_A$ is the volume fraction of CG beads. Figure 4.24 shows the intermolecular pair correlation function (PCF) to characterize the local intermolecular interaction. In the first two shells, the PCF is very small due to the positive intermolecular potential energy function in the discrete form. The maximum PCF value occurs in the third shell as the most negative intermolecular potential energy result in the attraction force. The PF-PEO and N-PEO models exhibit the maximum peak at the third shell of PCFs. These data suggest that the PF-PEO chains can better stay close to neighboring chains than

N-PEO. The effect of intermolecular packing is the reason why PF-PEO chains are more difficult to move.
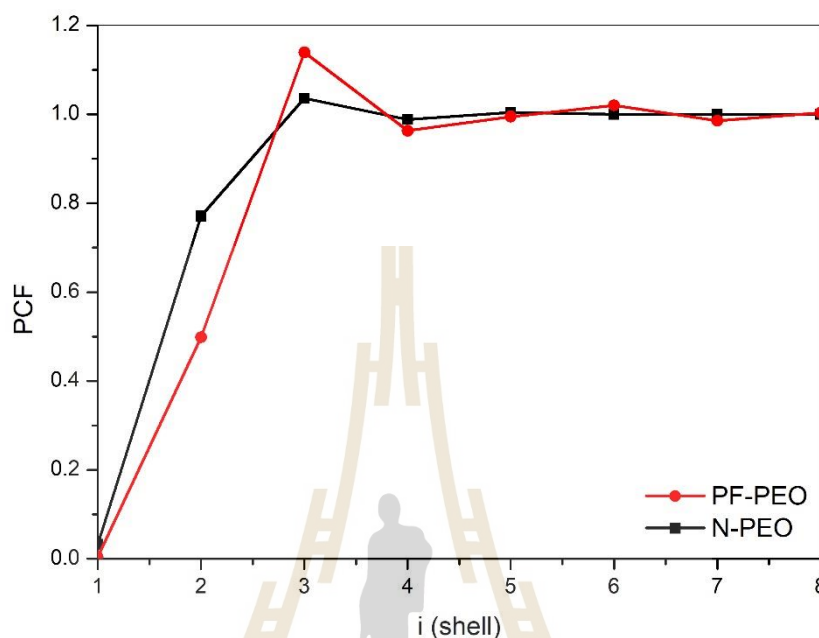


**Figure 4.24** The intermolecular pair correlation function (PCF) for the PF-PEO and N-PEO.

### 4.3.7 Scattering

Scattering experiments were useful techniques for investigating the amorphous polymer structure to determine the chain packing. The neutron elastic structure factor $S(Q)$ was calculated as the function of the magnitude of scattering vector $Q = (4\pi/\lambda)\sin(\theta)$, where $2\theta$ is the scattering angle and $\lambda$ is the wavelength of scattered radiation. The structure factor was calculated from the elemental pair distribution functions. Other parameters were the coherent scattering amplitudes, $f_\alpha$, and a Debye-Waller type root-mean-square displacement of atoms due to thermal vibration. The scattering curve, $I(Q)$, is related by a Fourier transform operation to the radial distribution function. The calculated spectrum of neutron scattering exhibits good agreement for the first three peaks at $Q$ = 1.3 (1.7), 3.0 (3.0), and 5.4 (5.5) $\text{Å}^{-1}$ for PF-PEO (N-PEO) as illustrated in Figure 4.25. These locations agree with the experimentally

observed peaks (Borodin, 2003) quite well for N-PEO. The difference between the prediction and experiment lies in the intensity and the shape of the signal especially after the third peak. The scattering results indicate reasonable agreement to some extent between the computed and the actual structure.
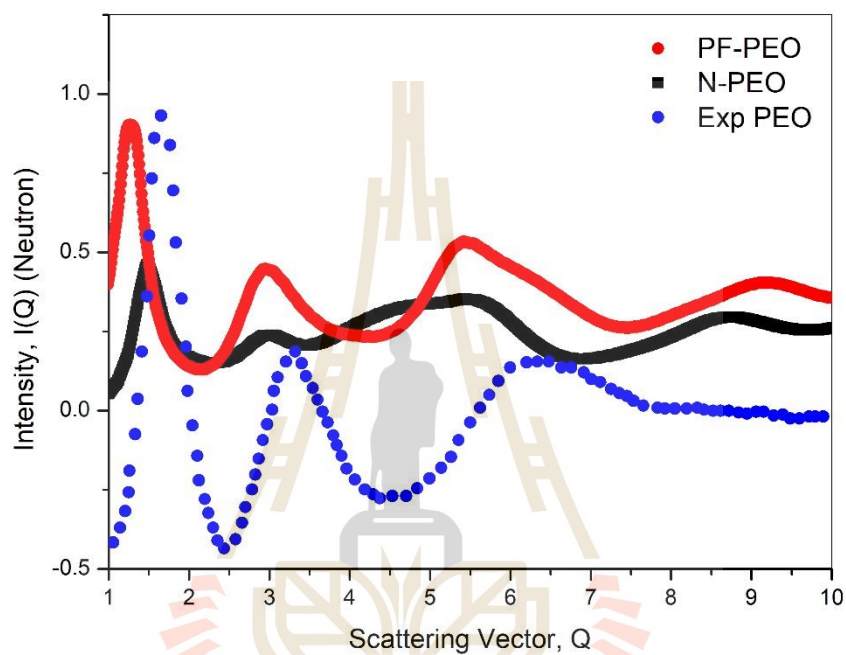


**Figure 4.25** Neutron scattering for PF-PEO and N-PEO models.

## 4.4 Molecular Dynamics (MD) Simulation and X-ray Absorption Spectroscopy to Characterize the Local Structure and Dynamics of Potassium ions in small molecules of SPEs

### 4.4.1 Molecular Dynamics (MD) simulation

The MD simulations have been used to determine the solvation structures at the atomistic level of the K-doped DME/DMEDA. The structural equilibration of the systems was judged by the constant in energy and density in the trajectories. The initial and final structure of MD snapshots in both systems is presented in Figure 4.26-4.27. After the equilibrium step, the $K^+$ ions are surrounded by neighboring anions and oxygen atoms. The solvation structure of the $K^+$ ion was estimated using the radial distribution functions (RDF) from trajectories of MD simulation. As shown in Figure 4.28, the RDF and coordination number (CN) are represented by the solid and dashed lines, respectively, for cations with DME/DMEDA and cations with anions. The characterized RDF parameters for the overall solvation structure of $K^+$ from the trajectories of MD simulation including integration range, peak position $R_0$, and CN are listed in Table 4.4. There is the first shell of K···O interactions at $r$ = 2.68 - 4.42 Å and K···N interactions at $r$ = 2.80 - 4.28 Å in Figure 3(a). The oxygen coordination is closer to the $K^+$ ion than nitrogen coordination because of the effect of the *gauche* conformation in DME and the steric effect of the nitrogen atom in DMEDA. The cation-anion correlation shows only one important peak at $r$ = 3.00 – 6.30 Å for K···S-SCN and 2.70 – 6.44 Å for K···N-SCN with a shoulder around 6.0 Å (Figure 28(b)). The peak position and CN of both K···S-SCN and K···N-SCN are quite no different for each system. These results suggest that the anions coordinate with the $K^+$ ion in a bidentate whereas the nitrogen atoms are closer than the sulfur atoms.
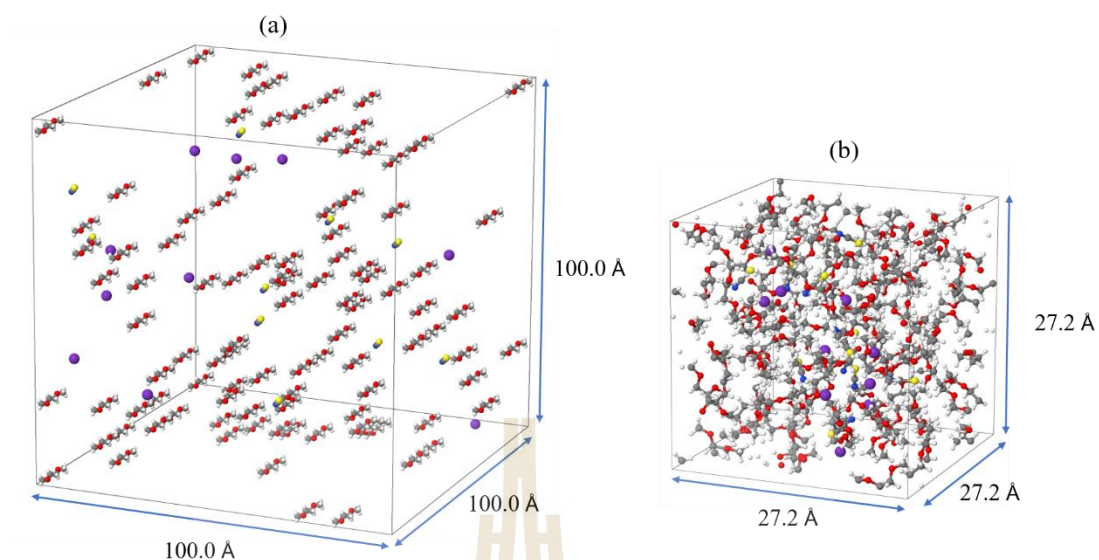
**Figure 4.26** (a) The initial and (b) final structures 100DME10KSCN from MD trajectories. The K$^+$, oxygen, carbon, sulfur, nitrogen, and hydrogen atoms are represented in purple, red, grey, yellow, blue, and white colors, respectively.
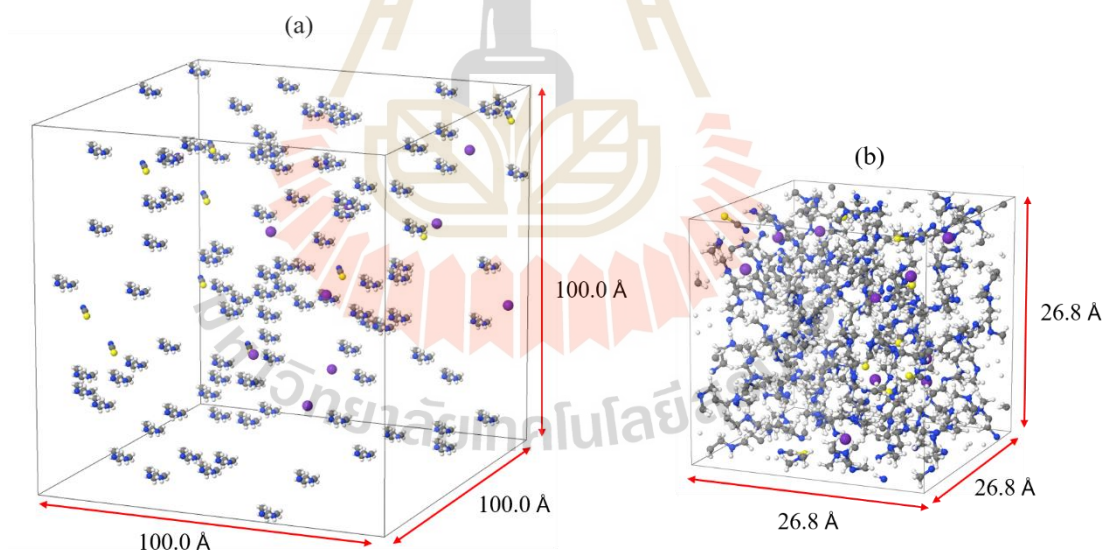


**Figure 4.27** (a) The initial and (b) final structures 100DMEDA10KSCN from MD trajectories. The K$^+$, nitrogen, carbon, sulfur, and hydrogen atoms are represented in purple, blue, grey, yellow, and white colors, respectively.
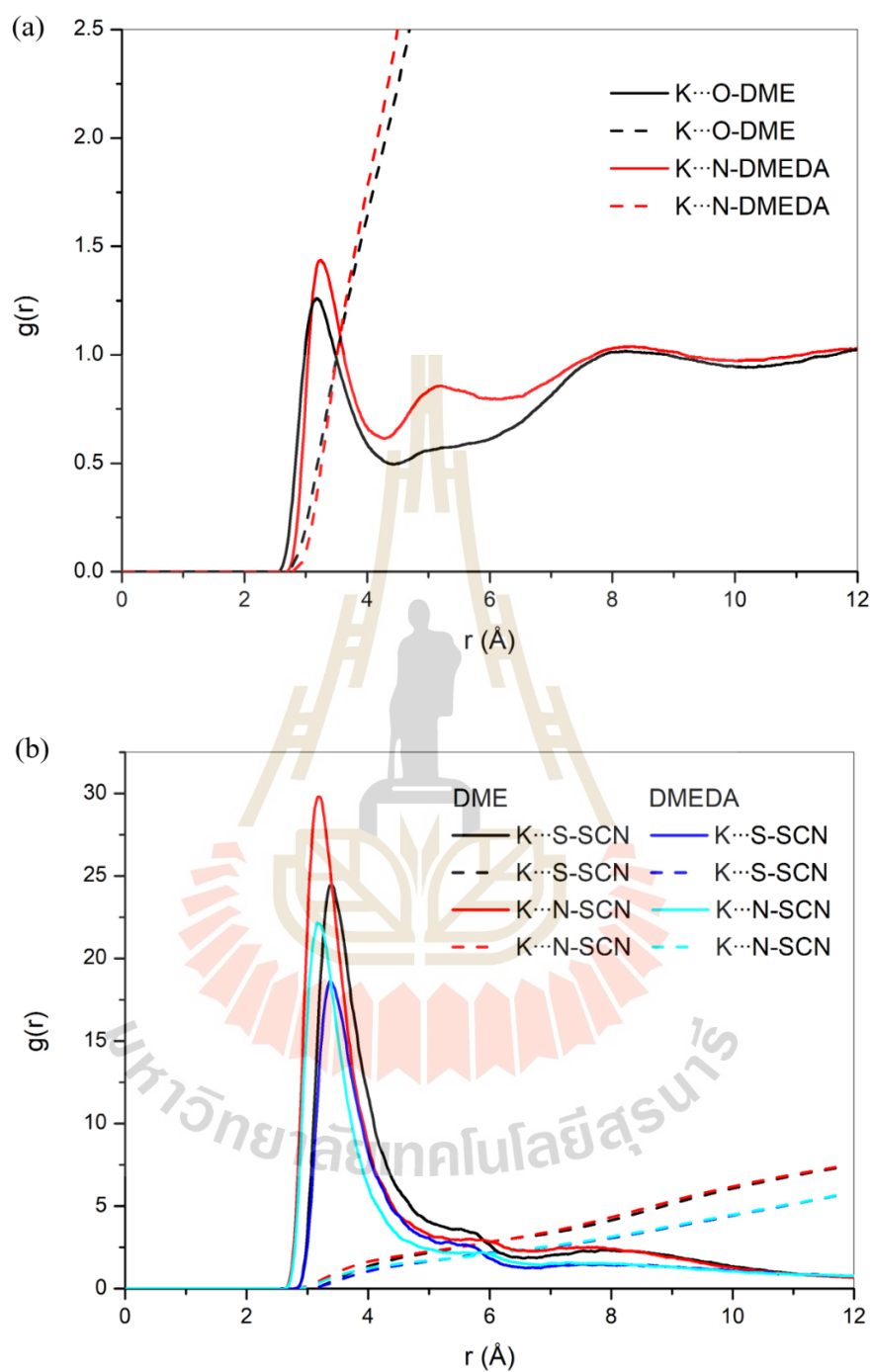
**Figure 4.28** The RDF of (a) K···O-DME and K···N-DMEDA correlation and (b) K···S-SCN and K···N-SCN correlation for 100DME10KSCN and 100DMEDA10KSCN systems.

**Table 4.4** Solvation structural parameters of the first shell determined from MD simulation.

| Coordination type | Integration range (Å) | Peak position $R_0$ (Å) | Coordination number (CN) |
|---|---|---|---|
| 100DME10KSCN | | | |
| K···O-DME | 2.68 - 4.42 | 3.18 | 2.1 |
| K···S-SCN | 3.00 – 6.30 | 3.40 | 3.0 |
| K···N-SCN | 2.70 – 6.44 | 3.20 | 3.1 |
| 100DMEDA10KSCN | | | |
| K···N-DMEDA | 2.80 - 4.28 | 3.24 | 2.7 |
| K···S-SCN | 3.00 – 6.30 | 3.36 | 2.3 |
| K···N-SCN | 2.70 – 6.44 | 3.20 | 2.3 |

For the probability distribution of solvated cations, Figure 4.29 represents the distribution of CN of the oxygen and nitrogen atoms coordinated with the $K^+$ ions in the first shell (4.42 Å and 4.28 Å for 100DME10KSCN and 100DMEDA10KSCN, respectively). The range in the CN of K···O coordination is 0 to 7 in the first shell as depicted in Figure 4.29(a). This result shows that the most probable structure for the K···O coordination in 100DME10KSCN consists of two oxygen atoms. For K···N correlation in 100DMEDA10KSCN, the CN ranges from 1 to 6 with three nitrogen atoms are the most probable structure (Figure 4.29(b)). Therefore, the most probable solvation structure should be composed of 1-3 oxygen atoms or 2-4 nitrogen atoms of DME and DMEDA, respectively, which is important in determining the most probable solvation structure to solvate $K^+$ ions.
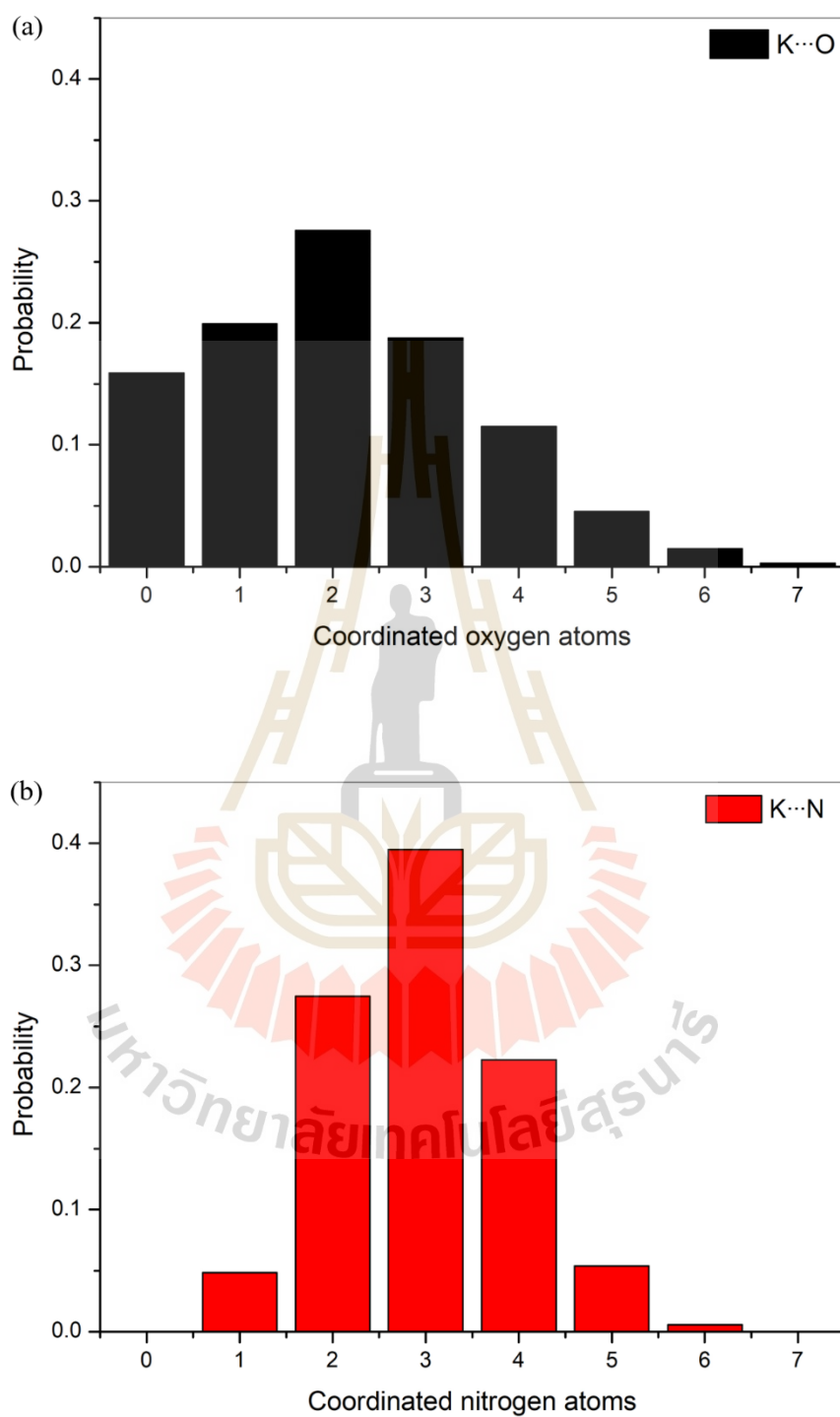
**Figure 4.29** Distribution of the CN of (a) the K···O and (b) K···N coordination for solvation structures determined from MD simulations.

From the RDF analysis and distribution of the CN, there have to be around 2 oxygen atoms of DME and 3 nitrogen atoms of DMEDA to coordinate the $K^+$ ion. To define whether these atoms are from different or the same chains, the selected MD snapshot of the 100DME10KSCN and 100DMEDA10KSCN models is depicted in Figure 4.30. These results suggest that oxygen atoms correlated with $K^+$ ions in the first coordination shell with a CN of 2, whereas nitrogen atoms have a CN of 3. When considering a probable solvation structure of $K^+$ ion, occurs in both intra- and inter-molecular interaction for both DME and DMEDA chains.
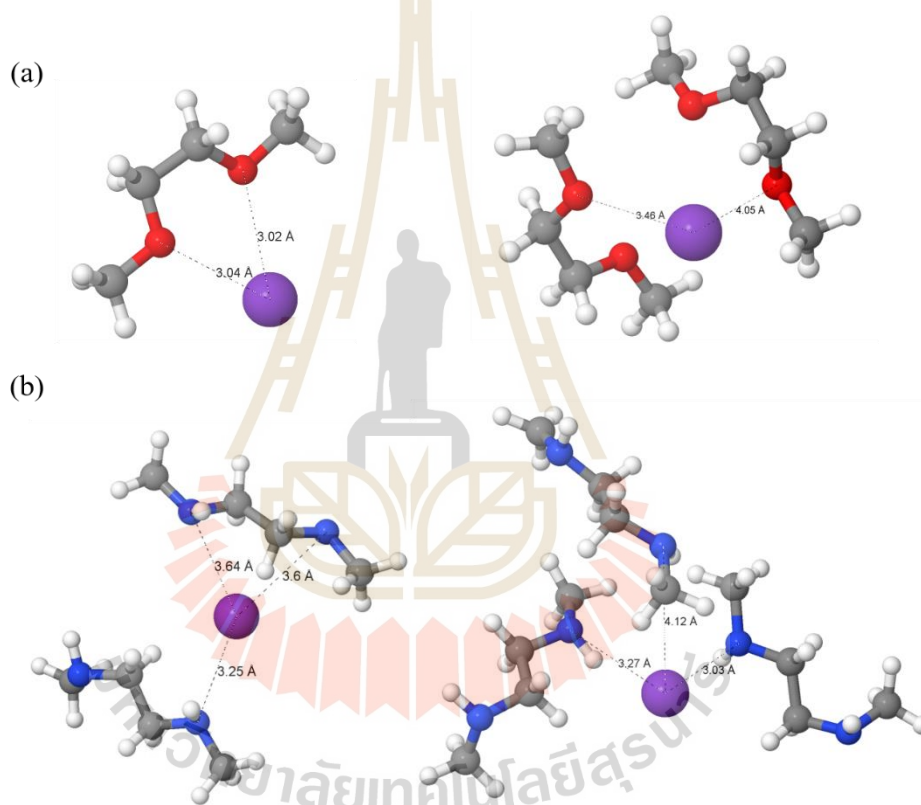


**Figure 4.30** The coordination structure from the selected MD snapshot of (a) 100DME10KSCN and (b) 100DMEDA10KSCN models ($K^+$, oxygen, nitrogen, carbon, and hydrogen atoms are represented in purple, red, blue, grey, and white colors, respectively)

### 4.4.2 Short-time dynamics

Figure 4.31 presents the MD simulation of the selected K$^+$ ion, oxygen/nitrogen atom of DMD/DMEDA, and anion (S and N atom) recorded every 500 ps. The movement of all selected atoms is seen similarly. The absolute displacement of oxygen/nitrogen atoms, K$^+$ ion, sulfur anion, and nitrogen anion were calculated in the short-time dynamics as shown in Figure 4.32. From Table 4.5, the absolute displacement of oxygen atoms (0.473 nm) and K$^+$ ions (0.420 nm) in 100DME10KSCN system are slightly higher than that of nitrogen atoms (0.368 nm) and K$^+$ ions (0.376 nm) in 100DMEDA10KSCN system but smaller than that of the anion (S and N atom) for both two systems. The magnitude of absolute displacement and their standard deviation suggest the flexibility of the solvation structures. These results indicate that K$^+$ ions have strong interaction with the nitrogen atoms of DMEDA and nitrogen atoms move more slowly than oxygen atoms of DME while anions have larger amplitudes of displacement suggesting that anions are quite weaker interacting with K$^+$ ions in the 100DMEDA10KSCN system.

Figure 4.33 displays the mean-square displacement (MSD) of K$^+$ ion, pure and K-doped DME or DMEDA molecules, and anions. The magnitudes of MSDs for all species are quite similar in the 100DMEDA10KSCN system while that of DME is much higher than that of K$^+$ ion. The diffusion coefficient (D) can be calculated by Gromacs software using the equation:

$$D = \frac{\lim\limits_{t \to \infty} \langle \| r_i(t) - r_i(0) \|^2 \rangle}{6t} = \frac{MSD}{6t} \tag{4.12}$$

where $r_i(0)$ and $r_i(t)$ are the positions of species $i$ at the time = $0$ and $t$, respectively. Table 4.6 presents the estimated diffusion coefficients for each species. The diffusion of DMEDA is slower than that of DME because of relatively stronger interaction with other components (cation and anion).

(a)



(b)
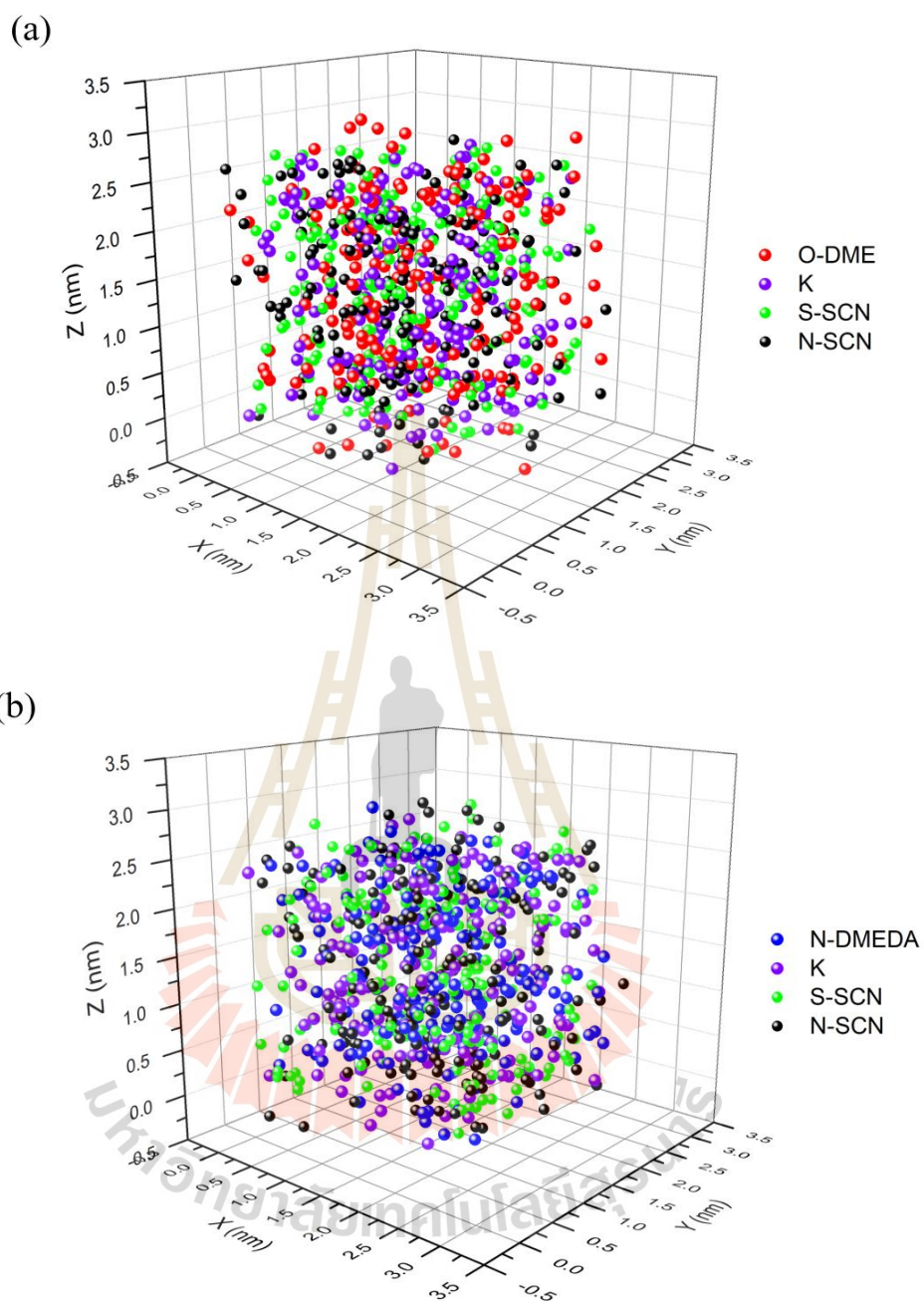
**Figure 4.31** Trajectories of oxygen/nitrogen atom, K$^+$ ion, and anion (S and N atom) for the (a) 100DME10KSCN and (b) 100DMEDA10KSCN systems recorded every 500 ps.
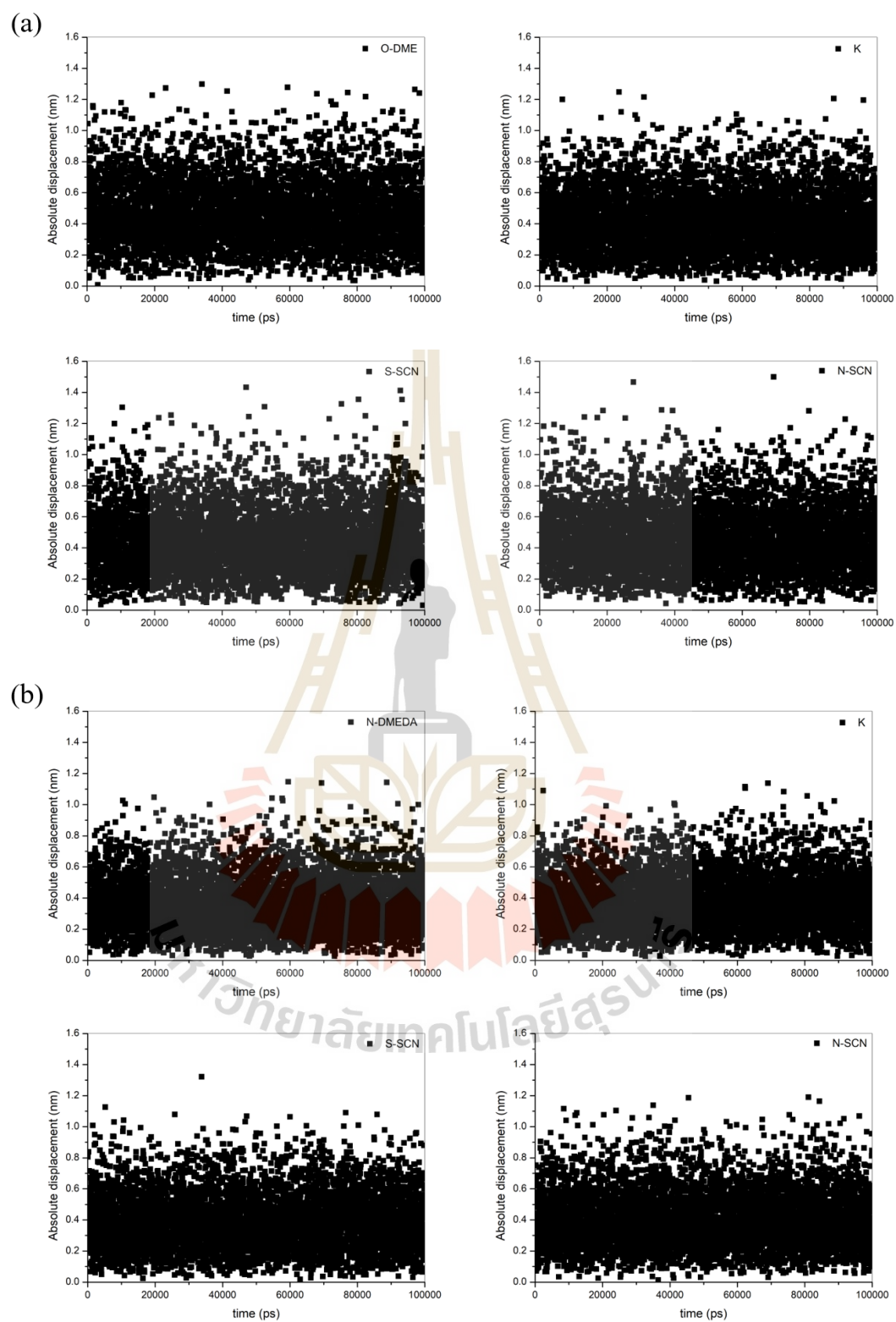
**Figure 4.32** The absolute displacement of oxygen/nitrogen atom, K$^+$ ion, and anion for the (a) 100DME10KSCN and (b) 100DMEDA10KSCN systems.

**Table 4.5** The absolute displacement and standard deviation of oxygen/nitrogen atom of DME/DMEDA, K$^+$ ion, and anion (S and N atom).

| Specie | Absolute displacement (nm) | Standard deviation |
|---|---|---|
| **100DME10KSCN** | | |
| O-DME | 0.473 | 0.209 |
| K | 0.420 | 0.190 |
| S-SCN | 0.452 | 0.203 |
| N-SCN | 0.462 | 0.203 |
| **100DMEDA10KSCN** | | |
| N-DMEDA | 0.368 | 0.169 |
| K | 0.376 | 0.170 |
| S-SCN | 0.394 | 0.180 |
| N-SCN | 0.411 | 0.180 |
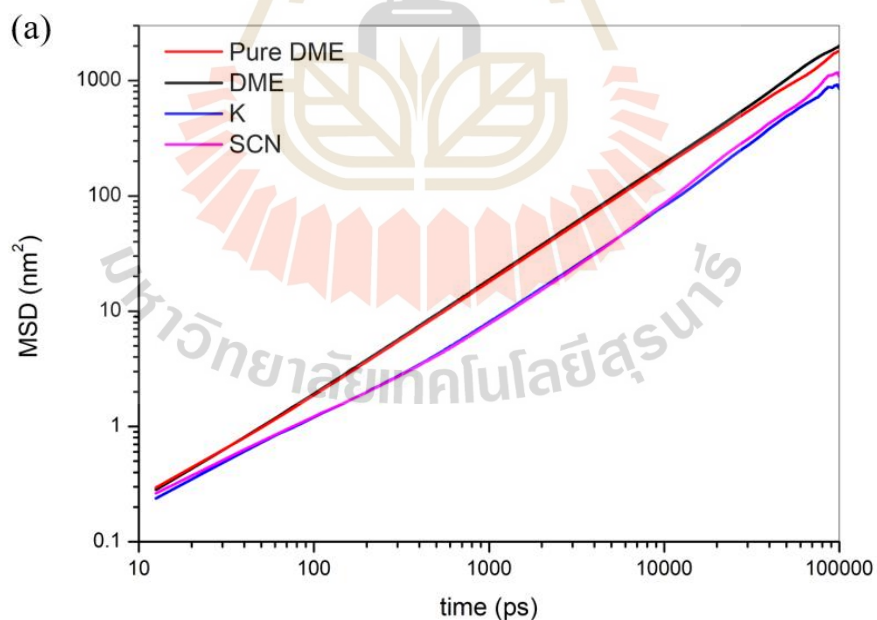


**Figure 4.33** The MSD of K$^+$ ion, pure and K-doped of DME or DMEDA molecules, and anions for the (a) 100DME10KSCN and (b) 100DMEDA10KSCN systems.
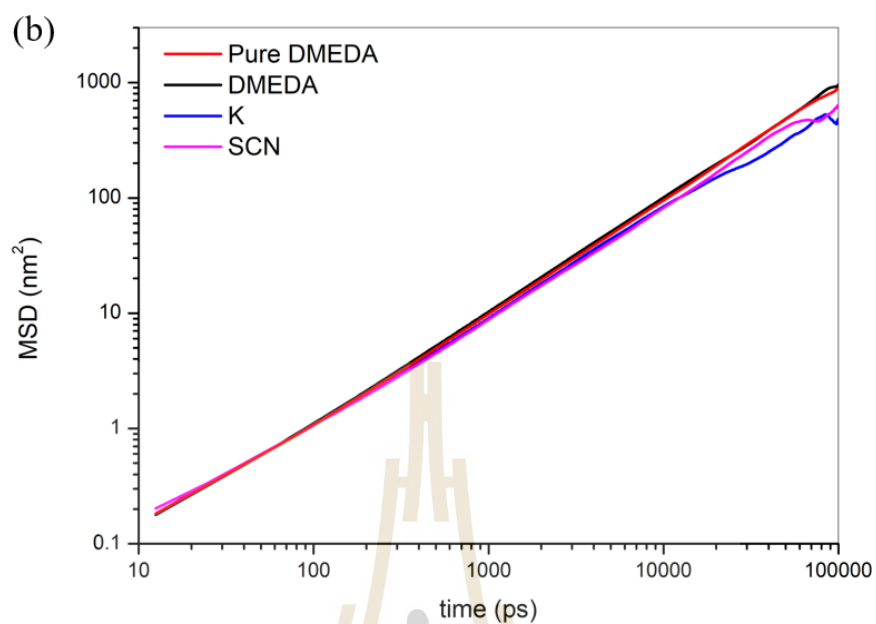
**Figure 4.33** (Continued) The MSD of $K^+$ ion, pure and K-doped of DME or DMEDA molecules, and anions for the (a) 100DME10KSCN and (b) 100DMEDA10KSCN systems.

**Table 4.6** The diffusion coefficient of $K^+$ ion, pure and K-doped DME and DMEDA molecules, and anions.

| Specie | Diffusion coefficient x $10^{-13}$ (cm$^2$/s) |
|---|---|
| Pure DME | 2.933 |
| DME | 3.483 |
| K | 1.683 |
| SCN | 1.850 |
| Pure DMEDA | 1.617 |
| DMEDA | 1.600 |
| K | 0.967 |
| SCN | 1.350 |

### 4.4.3   Solvation Structure by MD-EXAFS

Extend X-ray absorption fine structure (EXAFS) method was used to investigate the solvation structure of $K^+$ ions in K-doped DME/DMEDA samples. The standard KSCN and samples are plotted in Figure 4.34 for the subtracted background and normalized EXAFS spectra of the probed potassium. The EXAFS provides an oscillation pattern of spectra in the $k$ range of 3 - 6 with a noise signal as $k$ increases. The radial structure-function (RSF) generated from the Fourier transform procedure to convert data from $k$ to $r$ space is shown in Figure 4.35. The RSF from EXAFS is correlated to the RDF from MD simulation but difference in the coordination distance ($r$). The first dominant coordination shell is around 2 Å. The coordination number in the K⋯O and K⋯N solvation shell were determined using the selected atomic coordinates from the MD trajectory. The goodness of fitting of these two systems is described next.

In the first fitting step, the KSCN was the standard material to model the solvation structure of samples. The crystal structure of KSCN (Klug, 1933) was used as a reference structure to fit the EXAFS of the standard KSCN. EXAFS spectra of KSCN were fitted with the KSCN crystal structure to determine the crude amplitude ($S_0^2$) of standard material. In the fitting step, the amplitude ($S_0^2$) was fixed while other parameters were adjusted for the energy shift ($E_0$), the distance shift ($\Delta R$), and the Debye-Waller factors ($\sigma^2$). Then the fixed amplitude of standard material is used to calculate the coordination number of K-doped DME/DMEDA samples. The fitting results are presented in Figure 4.36 for k- and r-space. The fitting is quite good with an R-factor of 0.025 and an amplitude of 1.009.

(a)



(b)
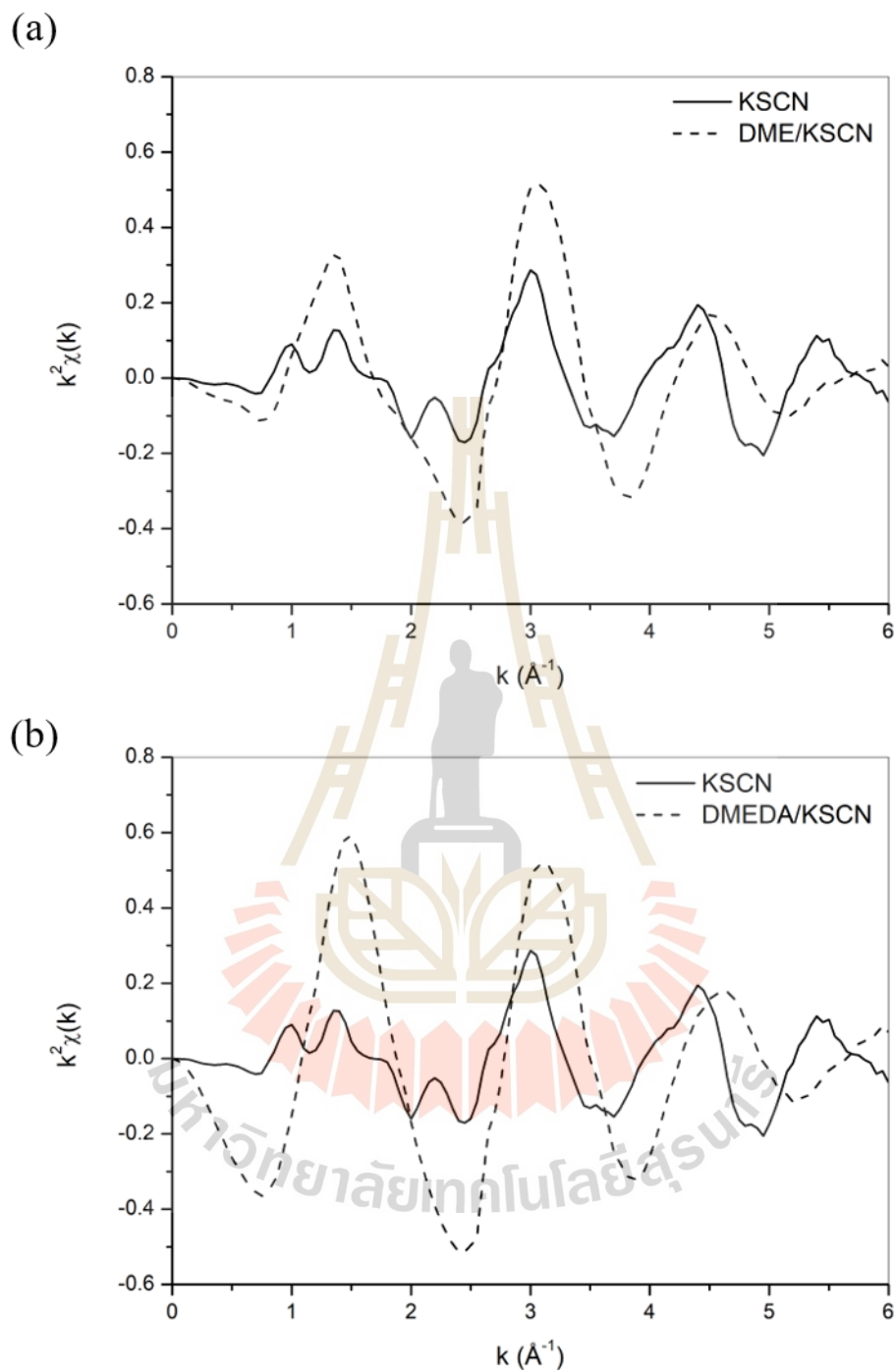


**Figure 4.34** The first coordination shell of the standard KSCN and samples in the wave vector space ($k^2\chi$) for K-doped (a) DME and (b) DMEDA.
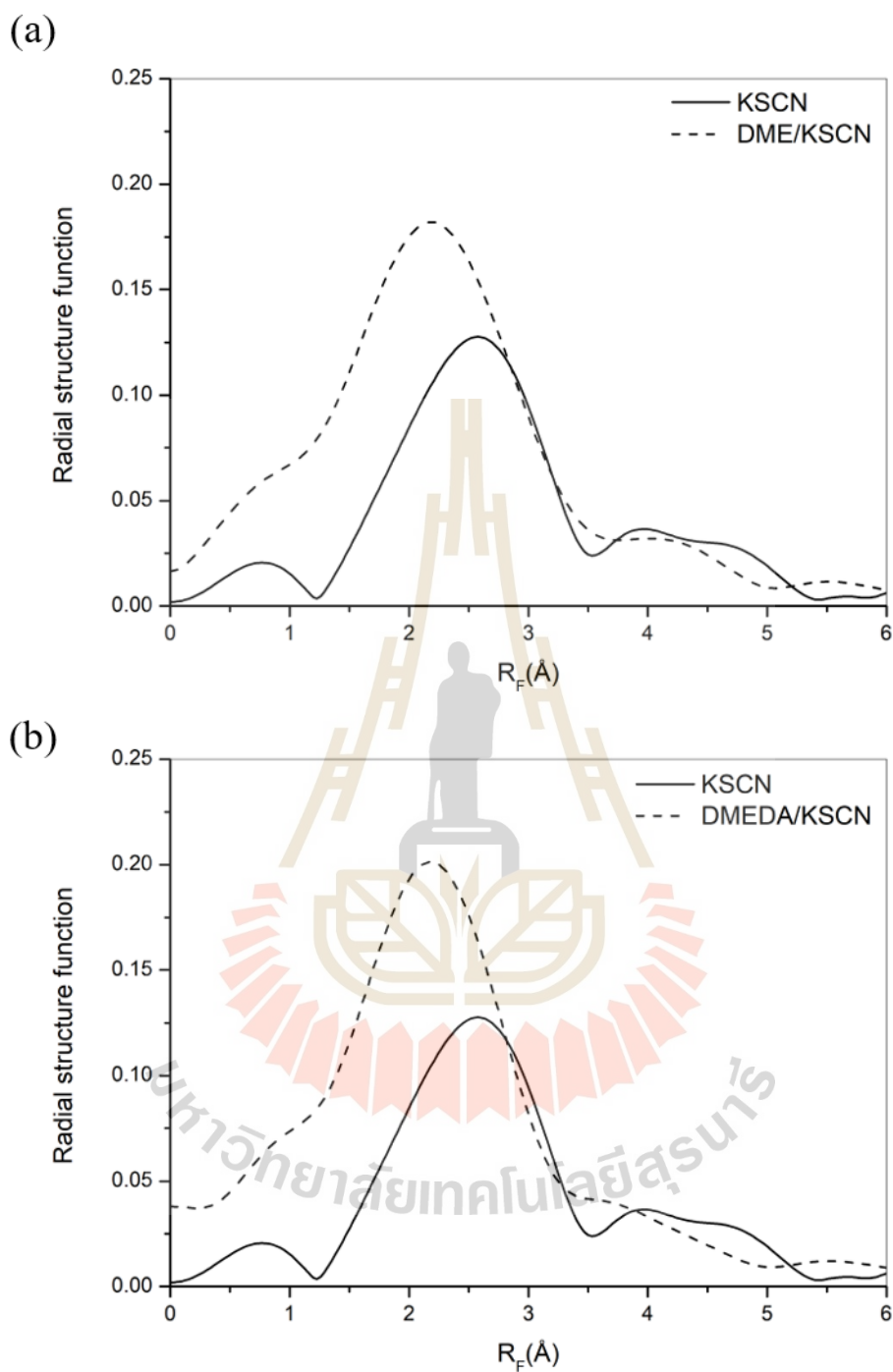
**Figure 4.35** The first coordination shell of the standard KSCN and samples in the real space (the radial structure function) for K-doped (a) DME and (b) DMEDA.
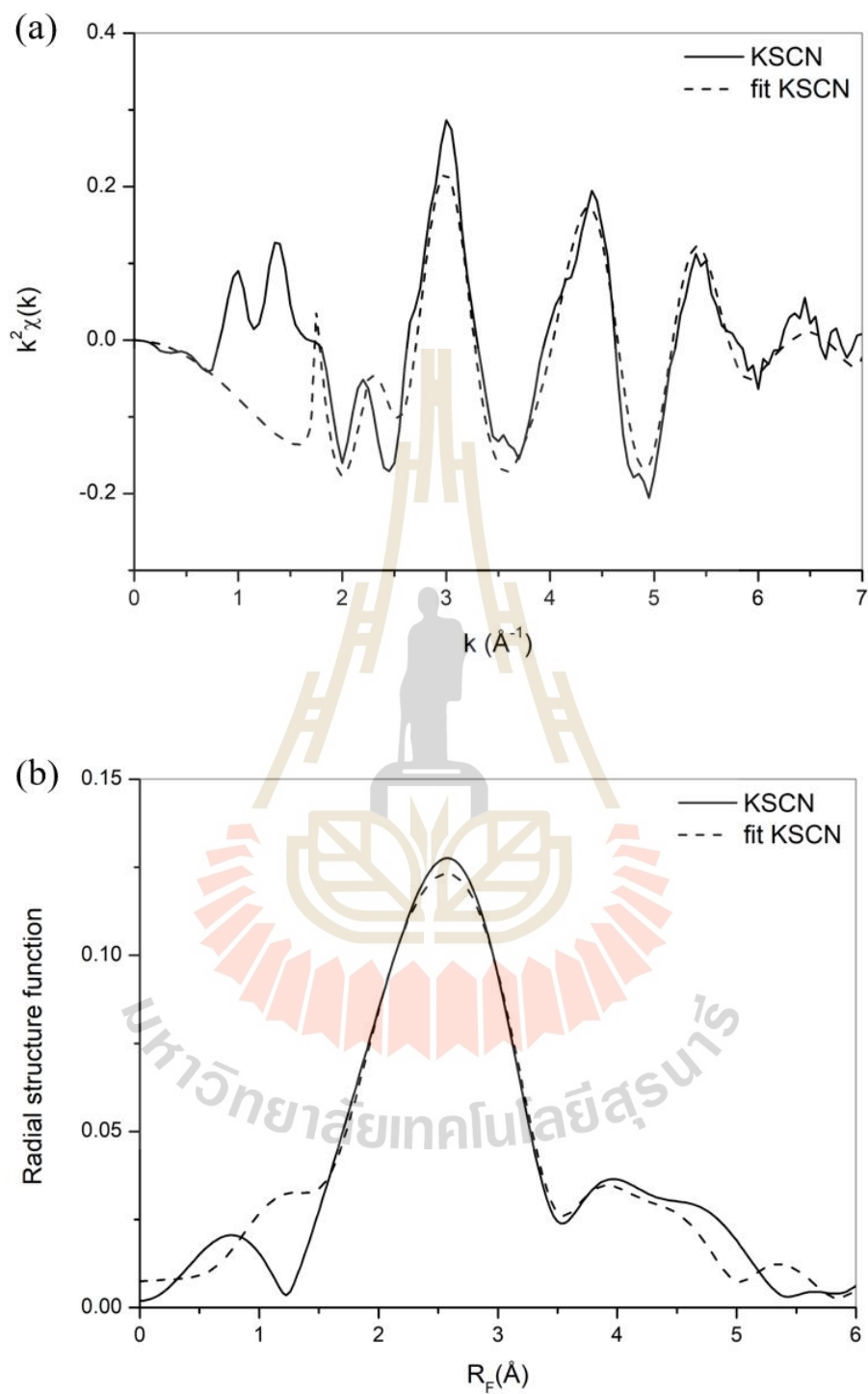
**Figure 4.36** Fitting the first coordination shell of the standard KSCN with KSCN crystal structure (a) $k^2\chi$ and (b) radial structure-function.

        The atomistic coordination of the selected MD snapshot (Tables 4.7 and 4.8)
was used to fit with the EXAFS spectra. The proposed solvation structure of $K^+$ by
oxygen and nitrogen atoms from MD simulation is represented in Figure 4.5. The
parameters that were used in the fitting step included the amplitude reduction factor
($S_0^2$), the energy shift ($E_0$), the distance shift ($\Delta R$), and the Debye-Waller factors ($\sigma^2$).
Figures 4.37 and 4.38 present the best fits using a combination method of the atomic
coordinates from the selected MD trajectories and experimental EXAFS spectra in both
$k$- and $r$-space. All of the fitting parameters are listed in Table 4.9. The quality fitting is
well and quite no different for the MD-EXAFS method of K-doped DME (R-factor =
0.015) and DMEDA (R-factor = 0.022). The distance shift is quite small, which suggests
that the K···O distance from the MD simulation is close to experimental data. $K^+$ ions
stay closer to the nitrogen atoms of DMEDA than oxygen atoms of DME because $K^+$
ions strongly interact with nitrogen atoms to neutralize the charge.

        For the advantage of the fitting by MD-EXAFS technique, it can be used to fit
with highly disordered materials and specify more details about the solvated atoms.
For example, the solvation of $K^+$ ions by nitrogen atoms can be identified from both
DMEDA and anion. Dynamics information in a short time scale for the solvation
structure can be determined from the MD trajectory while experimental EXAFS spectra
can provide only the structure information without dynamic information.

**Table 4.7** Atomic coordinates from MD snapshot of 100DME10KSCN.

| X (Å) | Y (Å) | Z (Å) | Atom type | distance |
|-------|-------|-------|-----------|----------|
| 0 | 0 | 0 | K | 0 |
| -0.36 | -3.04 | 1.15 | O | 3.270 |
| -2.16 | 1.11 | -2.28 | N-SCN | 3.331 |
| 0.89 | 2.79 | 1.61 | C-SCN | 3.342 |
| 1.05 | 2.05 | 2.48 | N-SCN | 3.385 |
| 0.39 | -1.57 | -3.15 | O | 3.541 |
| 0.45 | 3.79 | 0.36 | S-SCN | 3.834 |
| 3.65 | -0.53 | -1.22 | O | 3.885 |
| -0.5 | -2.62 | -2.84 | C | 3.896 |
| 2.24 | -2.66 | 1.95 | O | 3.987 |
| -3.22 | 1.4 | -1.93 | C-SCN | 4.007 |
| -1.42 | -3.26 | 2.05 | C | 4.104 |
| 0.53 | -4.14 | 1.04 | C | 4.301 |
| 4.09 | 0.81 | -1.15 | C | 4.325 |
| 1.22 | 0.73 | -4.45 | O | 4.672 |
| 1.65 | -3.94 | 2.05 | C | 4.738 |
| 0.74 | -1.62 | -4.51 | C | 4.849 |
| 3.44 | -2.5 | 2.68 | C | 5.027 |
| 3.64 | -3.37 | -1.07 | O | 5.075 |
| 1.76 | -0.52 | -4.79 | C | 5.13 |
| -4.73 | 1.85 | -1.43 | S-SCN | 5.276 |
| 4.07 | -2.69 | -2.22 | C | 5.360 |
| -2.28 | 4.59 | -1.74 | K | 5.412 |
| -1.58 | 3.75 | 3.77 | C | 5.547 |
| 1.79 | 1.91 | -4.98 | C | 5.626 |
| -4.94 | -2.67 | 0.6 | C | 5.647 |
| -5.53 | -1.36 | 0.09 | C | 5.695 |
| 3.29 | -4.73 | -1.22 | C | 5.889 |
| -0.45 | -1.08 | 5.9 | C | 6.015 |

**Table 4.7** (Continued).

| X (Å) | Y (Å) | Z (Å) | Atom type | distance |
|-------|-------|-------|-----------|----------|
| 3.44 | 4.82 | -1.25 | C | 6.052 |
| -2.63 | -1.42 | 5.38 | C | 6.154 |
| 2.84 | 1.59 | 5.38 | K | 6.288 |
| 3.2 | 4.72 | -2.76 | C | 6.335 |
| -3.04 | 2.44 | 5.24 | C | 6.531 |
| -2.46 | 3.67 | 4.87 | O | 6.576 |
| -3.17 | -5.75 | -1.5 | C | 6.735 |
| -2.99 | -1.49 | -5.87 | C | 6.754 |
| -6.63 | -1.02 | 0.9 | O | 6.768 |
| -0.41 | -6.47 | -1.96 | C | 6.773 |
| -2.14 | 3.58 | -5.36 | C | 6.792 |
| -1.72 | -1.29 | 6.46 | O | 6.808 |
| -6.8 | 0.35 | 1.19 | C | 6.912 |
| -5.79 | -3.79 | 0.56 | O | 6.943 |
| -4.5 | 0.31 | -5.32 | C | 6.975 |
| 3.44 | 4.82 | -1.25 | C | 6.052 |
| -2.63 | -1.42 | 5.38 | C | 6.154 |
| 2.84 | 1.59 | 5.38 | K | 6.288 |
| 3.2 | 4.72 | -2.76 | C | 6.335 |

**Table 4.8** Atomic coordinates from MD snapshot of 100DMEDA10KSCN.

| X (Å) | Y (Å) | Z (Å) | Atom type | distance |
|-------|-------|-------|-----------|----------|
| 0 | 0 | 0 | K | 0 |
| 0.8 | 2.3 | -2.15 | N | 3.248 |
| -1.83 | -1.06 | 2.89 | N-SCN | 3.581 |
| 1.24 | 1.61 | 3.03 | S-SCN | 3.648 |
| -2.88 | 1.94 | 1.31 | C | 3.711 |
| 3.41 | -1.65 | -0.09 | N | 3.789 |
| 0.41 | 3.53 | -1.36 | C | 3.805 |
| 2.25 | 2.23 | -2.43 | C | 3.993 |
| 3.97 | -0.31 | 0.3 | C | 3.993 |
| -1.5 | -0.7 | -3.69 | C | 4.044 |
| -3.32 | 2.48 | -0.03 | N | 4.144 |
| -3.44 | -2.39 | 0.66 | C | 4.240 |
| 1.83 | -2.83 | 2.77 | C | 4.362 |
| 2.68 | 1.08 | -3.34 | C | 4.416 |
| -2.14 | -1.38 | 3.95 | C-SCN | 4.700 |
| 0.37 | -1.81 | -4.45 | C | 4.818 |
| -0.55 | -0.75 | -4.78 | N | 4.870 |
| 4.28 | -2.79 | -0.43 | C | 5.127 |
| 1.68 | 2.96 | 3.87 | C-SCN | 5.154 |
| -3.71 | 3.89 | 0.03 | C | 5.376 |
| 3.3 | 4.09 | 1.19 | C | 5.388 |
| 1.27 | -3.45 | 3.96 | N | 5.403 |
| 4.13 | 1.07 | -3.37 | N | 5.437 |
| -4.84 | -2.53 | 0.11 | N | 5.462 |
| -4.94 | -2.08 | -1.29 | C | 5.513 |
| 4.35 | -0.36 | 4.11 | C | 5.995 |
| -3.94 | 4.39 | -1.39 | C | 6.060 |
| 1.44 | -2.13 | -5.5 | C | 6.071 |
| 4.24 | 4.44 | 0.05 | N | 6.140 |

**Table 4.8** (Continued).

| X (Å) | Y (Å) | Z (Å) | Atom type | distance |
|-------|-------|-------|-----------|----------|
| 1.97 | -3 | 5.15 | C | 6.277 |
| 1.97 | 3.86 | 4.55 | N-SCN | 6.284 |
| -2 | -5.64 | 2 | N | 6.309 |
| -2.49 | -1.84 | 5.51 | S-SCN | 6.320 |
| -0.86 | 5.59 | 2.9 | C | 6.356 |
| 2.19 | -3.32 | -5.09 | N | 6.460 |
| -2.36 | 5.41 | 2.83 | N | 6.546 |
| -0.02 | -5.33 | -3.81 | N | 6.552 |
| -1.53 | 3.39 | -5.52 | N | 6.656 |
| -1.8 | -5.59 | 3.5 | C | 6.837 |
| -2.87 | 4.73 | 4.03 | C | 6.845 |
| -3.84 | 2.51 | -5.11 | C | 6.867 |
| -0.5 | 4.45 | -5.21 | C | 6.870 |
| -2.35 | -4.94 | -4.17 | C | 6.879 |
| -2.9 | 3.71 | -5.09 | C | 6.934 |

**Table 4.9** Fitting parameters of the first solvation shell: coordination number (CN), the amplitude reduction factor ($S_0^2$), the shift of energy ($E_0$), the shift of distance ($\Delta R$), and the first-shell oxygen Debye-Waller factors of K-doped DME and DMEDA.

| Sample | atom | CN | $S_0^2$ | $E_0$ (eV) | $\Delta R$ (Å) | R (Å) | $\sigma^2$ (Å$^2$) |
|--------|------|-----|---------|------------|----------------|-------|---------------------|
| K-doped DME with MD | O | 1 | 1.009 | -3.407 | -0.614 | 2.66 | 0.03481 |
| | O | 1 | 1.009 | -3.407 | -0.614 | 2.93 | 0.03481 |
| K-doped DMEDA with MD | N | 3 | 1.009 | -5.935 | -0.655 | 2.59 | 0.00966 |

**Figure 4.37** The first coordination shell of the K-doped DME in (a) the wave vector space ($k^2\chi$) and (b) the real space (the radial structure function) from the experiment and the best fit using the MD-EXAFS method.
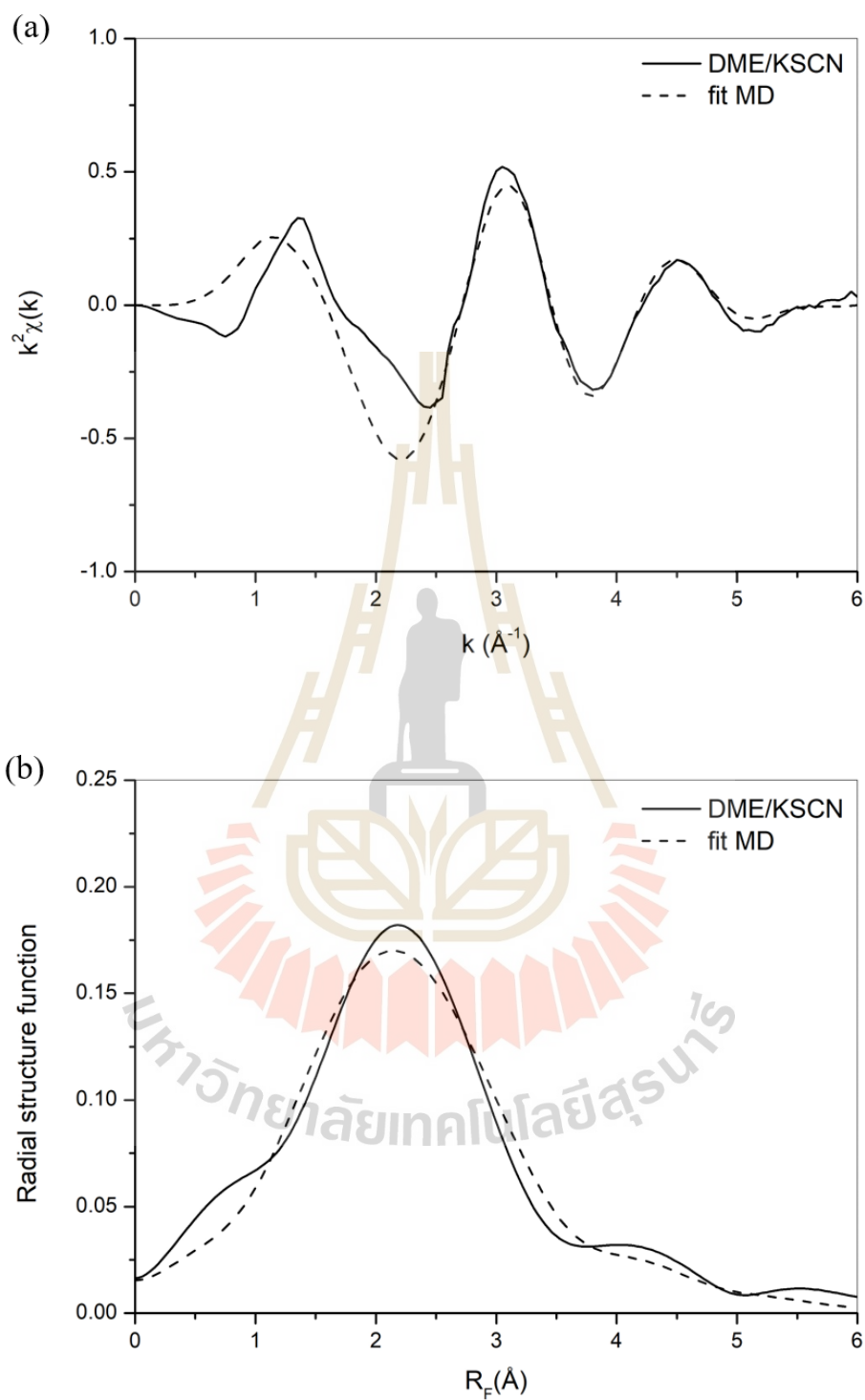
**Figure 4.38** The first coordination shell of the K-doped DMEDA in (a) the wave vector space ($k^2\chi$) and (b) the real space (the radial structure function) from the experiment and the best fit using the MD-EXAFS method.
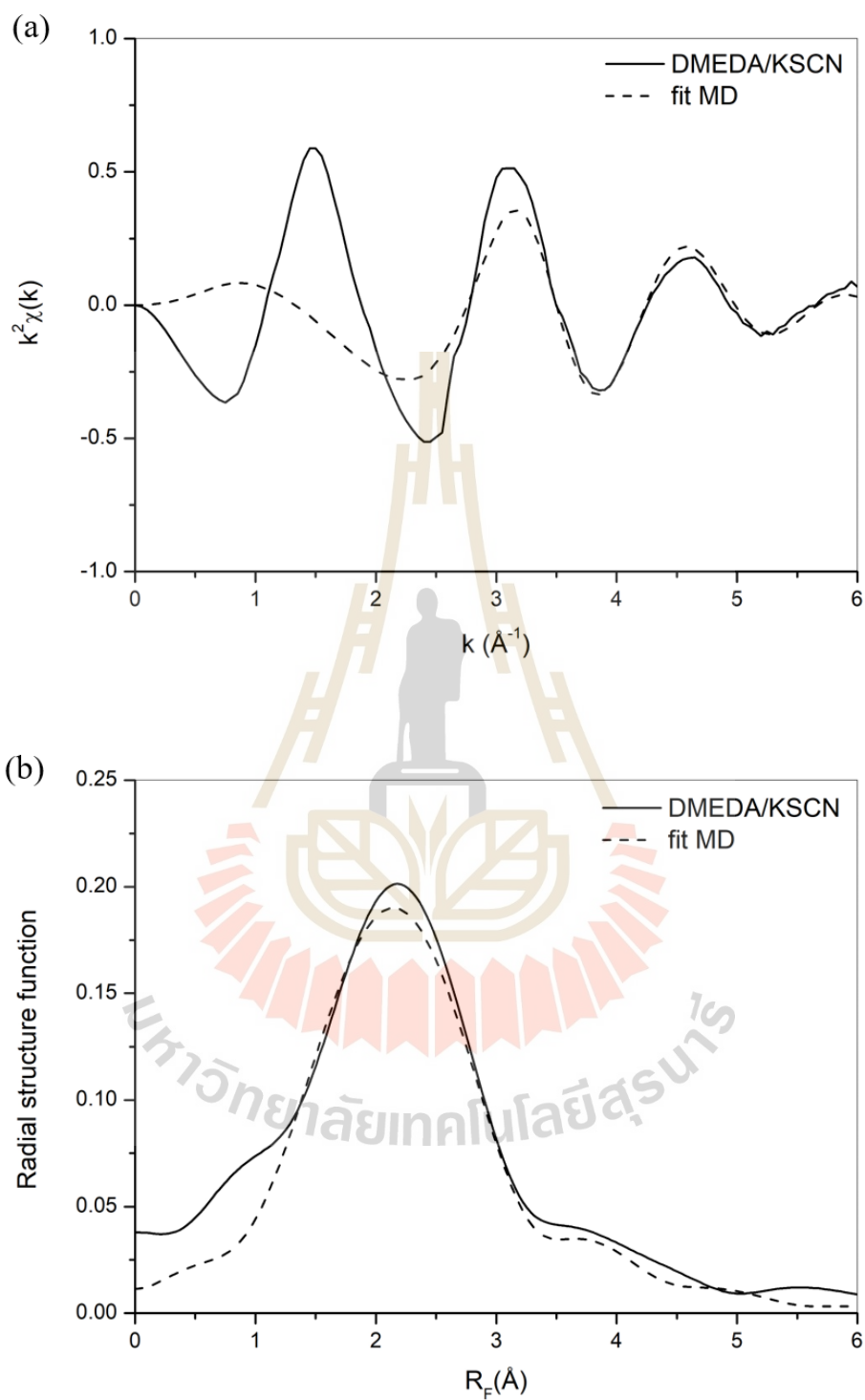
# CHAPTER V

# CONCLUSIONS

This work illustrates the structures and properties of polymer electrolytes based on both computer simulation and experiments. This thesis consists of four main parts: the effect of adding molecular fillers on polyethylene oxide-based SPEs, molecular simulation for the effect of chain stiffness on polymer crystallization from the melts, multiscale simulation for molecular and material properties of perfluoro- and normal poly(ethylene oxide) melts and MD simulation and X-ray absorption spectroscopy to characterize the local structure and dynamics of potassium ions in small molecules of SPEs.

For the first part, the effect of adding molecular fillers such as low molecular weight PEG (400 and 20,000 g/mol) and urea was studied on the crystallization and morphology. The isothermal crystallization was investigated using differential scanning calorimetry (DSC). Both PEG with a molecular weight of 20,000 g/mol and urea fillers can accelerate the crystallization of the PEO while crystallization was slower mixing with PEG at a molecular weight of 400 g/mol and with a mixed molecular weight of PEG. The isothermal crystallization kinetics of these samples were described by the Avrami model and the result suggests that the crystallization rate ($k$) tends to increase for PEG with a molecular weight of 20,000 g/mol and urea fillers while it was decreased for other fillers. The morphologies and spherulite growth as a function of the time of samples were investigated by polarized optical microscopy (POM). It can be seen that the growth rate becomes slower for the system with PEG at a molecular weight of 400 g/mol and with a mixed molecular weight of PEG. While the spherulite growth rate for the system with PEG at a molecular weight of 20,000 g/mol is increased compared to neat PEO. For SAXS analysis, the result suggests that the PEG fillers affect to increase crystal size of PEO.

In the second part, MC simulation of CG PE-like models was employed to study the effect of chain stiffness on polymer crystallization during an initial stage upon step-wise cooling from the melts. The change in conformational statistics, the orientation at bond and chain scale, chain packing, and intra- and intermolecular bond order parameters were determined. Simulation data show that the rate of structural formation and chain ordering is generally faster for chains with the stiffness parameter close to the normal PE. The chains with excessive flexibility or stiffness exhibit poorer crystallization. For highly flexible polymers, chains can adopt larger amounts of gauche conformation and find it difficult to form the ordered structure. For very stiff chains, they still have some gauche conformation which is hardly converted to the *trans-state* during the stepwise cooling from the molten state resulting in more difficulty in forming the ordered structures.

For the third part, a multiscale simulation technique of molecular models has been used to generate and equilibrate the polymeric materials in an amorphous structure. The systems of PF-PEO and N-PEO structures were studied by a combination of Monte Carlo (MC) simulation in high coordination lattice and Energy Minimization (EM)/Molecular Dynamic (MD) simulation techniques for mapping and reverse-mapping steps between coarse-grained chains and fully atomistic model. The local interaction parameters of polymer segment derived from both *ab initio* quantum chemistry to refine the RIS models used in the description of the conformational energies for each RIS of polymer chains. The bulk amorphous PF-PEO and N-PEO structure was generated and equilibrated by this lattice simulation technique with a great reduction of simulation time. The equilibrated structures from MC were reverse-mapped to a fully atomistic structure. Chain dimension, conformational characteristics, and structural and thermodynamic properties were determined. The calculated results were in good agreement with those obtained by the experiment.

In the final part, A combination of EXAFS and MD simulation was employed to characterize the solvation structures and short-time dynamics of K-doped DME or DMEDA at the atomistic scale. The oxygen coordination is closer to the $K^+$ ion than nitrogen coordination. For the short-time dynamic calculation, $K^+$ ions interact strongly with the nitrogen atoms of DMEDA leading to nitrogen atoms moving more slowly than

oxygen atoms of DME and anions are quite weaker interacting with $K^+$ ions in the 100DMEDA10KSCN system. The experimental EXAFS spectra were fitted with the atomic coordinates from the MD trajectory. Our studies suggest that the quality fitting is well and the MD-EXAFS techniques can give additional insight into the details of the solvation structure.
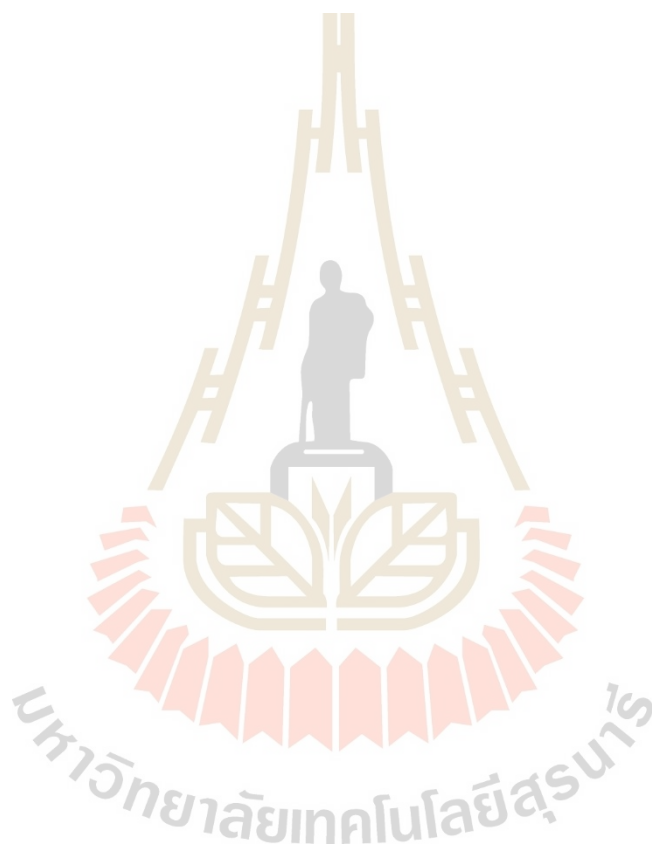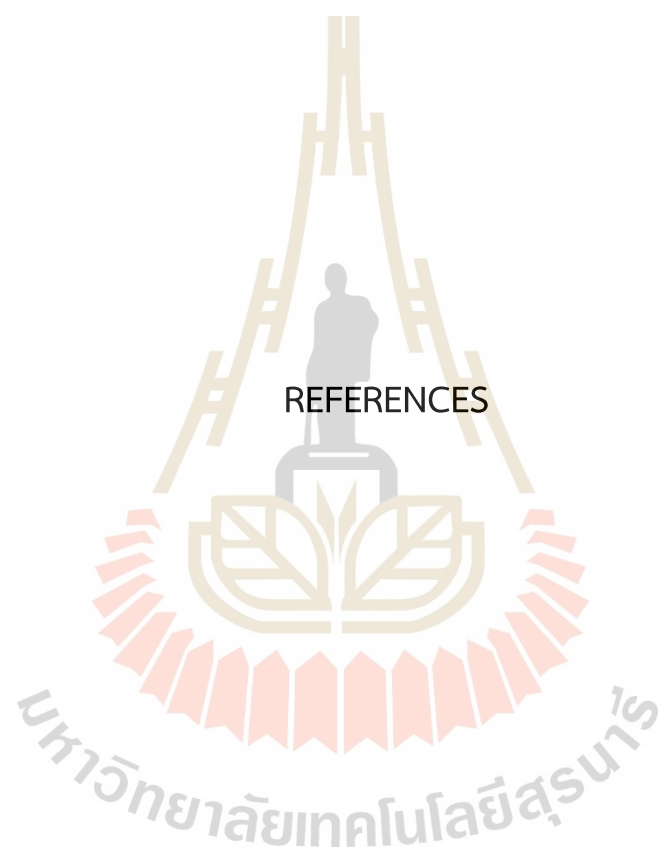
REFERENCES

# REFERENCES

Abe, A., Jernigan, R.L., and Flory, P.J. (1965). Conformational energies of n-alkanes and the random configuration of higher homologs including polymethylene. *Journal of the American Chemical Society, 88,* 631-639.

Abe, A., and Mark, J.E. (1976). Conformational energies and the random-coil dimensions and dipole moments of the polyoxides CH3O[(CH2)yO]xCH$_3$. *Journal of the American Chemical Society, 98,* 6468-6476.

Abe, A., Tasaki, K., and Mark, J.E. (1985). Rotational isomeric state analysis of poly(oxyethylene). Conformational energies and the random-coil configuration. *Polymer, 17,* 883-893.

Allen, M.P., and Tildesley, D.J. (1987). *Computer simulation of liquids*. Oxford University Press: Oxford.

Armitstead, K., Golbeck-Wood, G., and Keller, A. (1992) Polymer crystallization theories. *Advances in Polymer Science, 100,* 219-312.

Bandara, H.M.N., Schlindwein, W.S., Latham, R.J., and Linford, R.G. (1994). Comparison of the cation environment in polymer electrolytes based on poly(ethylene oxide) and transition-metal bromides. *Journal of the Chemical Society, Faraday Transactions, 90,* 3549-3553.

Baschnagel, J., Binder, B., Doruker, P., Gusev, A.A., Hahn, O., Kremer, K., Mattice, W.L., Muller-Plathe, F., Murat, M., Paul, W., Santos, S., Suter, U.W., and Tries, V. (2000). Bridging the gap between atomistic and coarse-grained models of polymers: status and perspectives. *Advances in Polymer Science, 152,* 41–156.

Borodin, O., Douglas, R., Smith, G.D., Trouw, F., and Petrucci, S.J. (2003). MD simulations and experimental study of structure, dynamics, and thermodynamics of poly(ethylene oxide) and its oligomers. *Journal of Physical Chemistry B, 107,* 6813-6823.

Borodin, O., Smith, G.D., and Douglas, R. (2003). Force field development and MD simulations of poly(ethylene oxide)/LiBF$_4$ polymer electrolytes. *Journal of Physical Chemistry B, 107,* 6824-6837.

Bruce, P.G. (1995). Structure and electrochemistry of polymer electrolytes. *Electrochimica Acta, 40,* 2077-2085.

Catlow, C.R.A., Chadwick, A.V., Greaves, G.N., Moroney, L.M., and Worboys, M.R. (1983). An EXAFS study of the structure of rubidium polyethyleneoxide salt complexes. *Solid State Ionics, 9-10,* 1107-1113.

Chaodamrongsakul, J., Merat, K., Klysubun, W., and Vao-Soongnern, V. (2013). A combined molecular dynamic simulation and X-ray absorption spectroscopy to investigate the atomistic solvation structure of cation in poly(vinyl alcohol):potassium thiocyanate (KSCN) solid electrolytes. *Journal of non-crystalline solids, 379,* 21-26.

Chaodamrongsakul, J., Klysubun, W., and Vao-soongnern, V. (2014). Application of X-ray absorption spectroscopy and molecular dynamics simulation to study the atomistic solvation structure of tetraglyme:KSCN electrolytes. *Materials Chemistry and Physics, 143,* 1508-1516.

Chen, T. (1991). Doctoral thesis. Cambridge: Massachusetts Institute of Technology.

Chen, C.-M., and Higgs, P.G. (1998). Monte-Carlo simulations of polymer crystallization in dilute solution. *Journal of Chemical Physics, 108,* 4305–4314.

Chen, C., Depa, P., Sakai, V.G., Maranas, J.K., Lynn, J.W., Peral, I., and Copleyet, J.R.D. (2006). A comparison of united atom, explicit atom, and coarse-grained simulation models for poly(ethylene oxide). *Journal of Chemical Physics, 124,* 234901.

Chillemi, G., D'Angelo, P., Pavel, N.V., Sanna, N., and Barone, V. (2002). Development and validation of an integrated computational approach for the study of ionic species in solution by means of effective two-body potentials. The case of Zn$^{2+}$, Ni$^{2+}$, and Co$^{2+}$ in aqueous solutions. *Journal of the American Chemical Society, 124,* 1968-1976.

Cho, J., and Mattice, W.L. (1997). Estimation of long-range interaction in coarse-grained rotational isomeric state polyethylene chains on a high coordination lattice. *Macromolecules, 30,* 637-644.

Clancy, T.C., and Mattice, W.L. (2000). Rotational isomeric state chains on a high coordination lattice: Dynamic Monte Carlo algorithm details. *Journal of Chemical Physics, 112,* 10049-10055.

Clancy, T.C., and Mattice, W.L. (2001). Miscibility of poly(vinyl chloride) melts composed of mixtures of chains with differing stereochemical composition and stereochemical sequence. *Macromolecules, 34,* 6482-6486.

Derakhshandeh, M., Mozaffari, G., Doufas, A.K., and Hatzikiriakos, S.G. (2014). Quiescent crystallization of polypropylene: experiments and modeling. *Journal of Polymer Science Part B: Polymer Physics, 52,* 1259-1275.

Dias, B.F., Plomp, L., and Veldhuis, J.B.J. (2000). Trends in polymer electrolytes for secondary lithium batteries. *Journal of Power Sources*, *88*, 169 – 191.

Doruker, P., and Mattice, W.L. (1997). Reverse mapping of coarse-grained polyethylene chains from the second nearest neighbor diamond lattice to an atomistic model in continuous space. *Macromolecules, 30,* 5520-5526.

Drongelen, M.V., Roozemond, P., Troisi, E., Doufas, A., and Peters, G. (2015) Quantification of non-isothermal, multi-phase crystallization of isotactic polypropylene: the influence of cooling rate and pressure. *Polymer, 76,* 254-270.

Ezquerra, T.A., Lopez-Cabarcos, E., Hsiao, B.S., and Balta-Calleja, F.J. (1996). Precursors of crystallization via density fluctuations in stiff-chain polymers, *Physical Review, 54,* 989-992.

Flory, P.J. (1956). Statistical thermodynamics of semi-flexible chain molecules. *Proceedings of the Royal Society A: Mathematical, Physical and Engineering Sciences, 234,* 60–73.

Flory, P.J. (1969). *Statistical mechanics of chain molecules*. New York: Wiley-Interscience.

Glatter, O., and Kratky, O. (1982). *Small Angle X-ray Scattering*. London: Academic Press.

Haliloglu, T., Cho, J., and Mattice, W.L. (1998). Simulations of rotational isomeric state models for poly(propy1ene) melts on a high coordination lattice. *Macromolecular Theory and Simulations, 7,* 613-617.

Haliloglu, T., and Mattice, W.L. (1998). Mapping of rotational isomeric state chains with asymmetric torsional potential energy functions on a high coordination lattice: application to polypropylene. *Journal of Chemical Physics, 108,* 6989–6995.

Helfer, C.A., Xu, G., Mattice, W.L., and Pugh, C. (2003). Monte Carlo simulations investigating the threading of cyclic poly (ethylene oxide) by linear chains in the melt. *Macromolecules, 36,* 10071-10078.

Hoffman, J.D., Davis, G.T., and Lauritzen, J.I., Jr. (1976) *The rate of crystallization of linear polymers with chain folding.* New York: Treatise on Solid State Chemistry; Springer.

Jamornsuriya, S., and Vao-soongnern, V. (2022). Molecular simulation of an initial stage of the ordered-structure formation of linear and ring polymers upon cooling from the melts. *Journal of Molecular Liquids, 363,* 119833.

Jo, G., Kim, O., Kim, H., Choi, U.H., Lee, S.B., and Park, M.J. (2016). End-functionalized block copolymer electrolytes: effect of segregation strength on ion transport efficiency. *Polymer Journal, 48*, 465–472.

Klug, H.P. (1933). The crystal structure of potassium thiocyanate. Crystallography Open Database.

Kusinram, C., and Vao-soongnern, V. (2022). A multiscale simulation of amorphous poly(vinyl alcohol). *Materials Today Communications, 30,* 103029.

Lavine, M.S., Waheed, N., and Rutledge, G.C. (2003). Molecular dynamics simulation of orientation and crystallization of polyethylene during uniaxial extension. *Polymer, 44,* 1771-1779.

Lee, Y.L., and Crist, B. (1986). Phase behavior and conductivity in poly(ethylene oxide)-sodium thiocyanate systems. *Journal of Applied Physics*, *60*, 2683-2689.

Li, L. (2014). Crystallization Behavior of Disproportionately High and Low Molecular Weight PEO Blends. *Chinese Journal of Polymer Science, 32,* 1199-1209.

Lightfoot, P., Mehta, M.A., and Bruce, P.G. (1992). Structure of the poly (ethylene oxide)–sodium perchlorate complex $PEO_3$–$NaClO_4$ from powder X-ray diffraction data. *Journal of Materials Chemistry, 2,* 379-381.

Lightfoot, P., Mehta, M.A., and Bruce, P.G. (1993). Crystal structure of the polymer electrolyte poly(ethylene oxide)$_3$:$LiCF_3SO_3$. *Science, 262,* 883-885.

Linford, R.G. (1995). EXAFS studies of polymer electrolytes. *Chemical Society Reviews, 24,* 267-277.

Luo, C., and Sommer, J.U. (2013). Disentanglement of linear polymer chains toward unentangled crystals. *ACS Macro Letters, 2,* 31-34.

Luo, C., and Sommer, J.U (2016). Role of thermal history and entanglement related thickness selection in polymer crystallization. *ACS Macro Letters, 5,* 30-34.

Mancini, G., Sanna, N., Barone, V., Migliorati, V., D'Angelo, P., and Chillemi, G.J. (2008). Structural and dynamical properties of the $Hg^{2+}$ aqua ion:  A molecular dynamics study. *Journal of Physical Chemistry B, 112,* 4694-4702.

Mattice, W.L. and Suter, U.W. (1994). *Conformational theory of large molecules. The rotational isomeric state model in macromolecular systems.* New York: Wiley.

McBreen, J., Yang, X.Q., Lee, H.S., and Okamoto, Y. (1995). X-Ray absorption studies of mixed salt polymer electrolytes. *Journal of The Electrochemical Society, 142,* 348-354.

Mendolia, M.S., and Farrington, G.C. (1995). High-conductivity, solid polymeric electrolytes. *Advances in Chemistry, 245,* 107-130.

Merat, K., Chaodamrongsakul, J., Tanthanuch, W., and Vao-soongnern, V. (2013). Atomistic solvation structure of calcium ion in poly (vinyl alcohol) as studied by molecular dynamics simulation and X-ray absorption spectroscopy. Journal of non-crystalline solids, 371, 47-52.

Metropolis, N., Rosenbluth, A.W., Rosenbluth, M.N., Teller, A.H., and Teller, E. (1953). Equations of state calculations by fast computing machines. *The Journal of Chemical Physics, 21,* 1087-1091.

Meyer, H., and Mulller-Plathe, F. (2001). Formation of chain-folded structures in supercooled polymer melts. *Journal of Chemical Physics, 115,* 7807-7810.

Meyer, H., and Muller-Plathe, F. (2002). Formation of chain-folded structures in supercooled polymer melts examined by MD simulations. *Macromolecules, 35,* 1241-1252.

Migliorati, V., Chillemi, G., and D'Angelo, P. (2011). On the solvation of the $Zn^{2+}$ ion in methanol: A combined quantum mechanics, molecular dynamics, and EXAFS approach. *Inorganic Chemistry, 50,* 8509-8515.

Patricia, M.C. (1994). Solution Properties of a Group of Perfluoropolyethers: Comparison of Unperturbed Dimensions, *Macromolecules, 27,* 6487-6491.

Piorkowska, E., and Rutledge, G.C. (2013). *Handbook of polymer crystallization*. New Jersey: John Wiley & Sons.

Preechatiwong, W., and Schultz, J.M. (1996). Electrical conductivity of poly(ethylene oxide)-alkali metal salt systems and effects of mixed salts and mixed molecular weights. *Polymer, 37,* 5109-5116.

Quartarone, E., Mustarelli, P., and Magistris, A. (1998). PEO – based composite polymer electrolytes. *Solid State Ionics, 110,* 1-14.

Rapold, R.F., and Mattice, W.L. (1995). New high-coordination lattice model for rotational isomeric state polymer chains. *Journal of the Chemical Society, Faraday Transactions, 91,* 2435-2441.

Rapold, R.F., and Mattice, W.L. (1996). Introduction of short and long range energies to simulate real chains on the 2nnd lattice. *Macromolecules, 29,* 2457-2466.

Ravel, B., and Newville, M. (2005). ATHENA, ARTEMIS, HEPHAESTUS: data analysis for X-ray absorption spectroscopy using IFEFFIT. *Journal of Synchrotron Radiation, 12,* 537-541

Reith, D., Meyer, H., and Mu, F. (2001). Mapping atomistic to coarse-grained polymer models using automatic simplex optimization to fit structural properties. *Macromolecules, 35,* 2335-2345.

Robitaille, C.D., and Fauteux, D. (1986). Phase diagrams and conductivity characterization of some PEO-LiX electrolytes. *Journal of the Electrochemical Society, 133,* 315-325.

Smith, G.D., Yoon, D.Y., and Jaffe, R.L. (1993). A Third-order rotational isomeric state model for poly(oxyethylene) based upon ab initio electronic structure analyses of model molecules. *Macromolecules*, *26*, 5213-5218.

Smith, G.D., Jaffe, R.L., and Yoon, D.Y. (1995). Conformations of perfluoro-poly(oxyethylene) from ab initio electronic structure calculations on model molecules. *Macromolecules*, *28*, 5804-5810.

Song, J.Y., Wang, Y.Y., and Wan, C.C. (1999). Review of gel-type polymer electrolytes for lithium-ion batteries. *Journal of Power Sources, 77*, 183-197.

Teo, B. (1986). *EXAFS: Basic principles and data analysis*. Heidelberg: Springer-Verlag.

Vao-soongnern, V., Doruker, P., and Mattice, W.L. (2000). Simulation of an amorphous polyethylene nanofiber on a high coordination lattice. *Macromolecular Theory and Simulations, 9,* 1-13.

Vao-soongnern, V., Xu, G., and Mattice, W.L. (2004). Structure formation in the crystallization and annealing of tetracontane nanoparticles. *Macromolecular Theory and Simulations, 13,* 539–549.

Vao-Soongnern, V. (2014). A multiscale simulation model for poly(ethylene oxide). *Polymer science, Series A, 56,* 928-935.

Vao-soongnern, V., Sukhonthamethirat, N., Rueangsri, K., Sirirak, K., and Matsuba, G. (2023). Molecular simulation of the structural formation of mono- and bidisperse polyethylene upon cooling from the melts. *Journal of Molecular Liquids, 376,* 121434.

Vasanthan, N., Shin, I.D., and Tonelli, A.E. (1996). Structure, conformation, and motions of poly(ethylene oxide) and poly(ethylene glycol) in their urea inclusion compounds. *Macromolecules, 29*, 263-267.

Vonk, C.G., and Kortleve, G. (1967). X-ray small-angle scattering of bulk polyethylene. *Polymer, 220*. 19-24.

Wang, T., Zhang, R., Wu, T., Li, H., and Zhuang, W. (2014). Simulating ion clustering in potassium thiocyanate aqueous solutions with various ion-water models. *Science China Chemistry, 57,* 1723-1730

Wichai, K., and Vao-soongnern, V. (2021). A multiscale simulation of amorphous polystyrene, *Journal of Polymer Research, 28,* 109.

Wichai, K., Vao-soongnern, V., Prasitnok, K., and Klysubun, W. (2023) Molecular dynamics simulation and X-ray absorption spectroscopy to characterize the local structure and dynamics of calcium ion in sulfonated polystyrene. *Journal of Molecular Structure, 1278,* 134972.

Wright, P.V. (1975). Electrical conductivity in ionic complexes of poly(ethylene oxide. *Polymer International, 7,* 319-327.

Xu, G., and Mattice, W.L. (2001). Study on structure formation of short polyethylene chains via dynamic Monte Carlo simulation. *Computational and Theoretical Polymer Science, 11,* 405-413.

Xu, G., Vao-soongnern, V., and Mattice, W.L. (2002). Similarities and differences in the rapid crystallization induced in n-tetracontane by an instantaneous deep quench of the free-standing nanofiber and free-standing thin film. *Macromolecular Theory and Simulations, 11,* 494-500.

Yamamoto, T. (2009). Computer modeling of polymer crystallization-toward computer-assisted materials design. *Polymer, 50,* 1975-1985.

Zeng, W., Liu, J.C., Zhou, J.F., Dong, J.Y., and Yan, S.K. (2008). A comparison study on the melt crystallization kinetics of long chain branched and linear isotactic polypropylene. *Chinese Sciences Bulletin, 53,* 188-197.

Zhang, D., Yan, H., Zhang, H., Zhu, Z., and Qilu (2011). Electrochemical properties of the solid polymer electrolyte $PEO_{20}–LiSO_3CF_3–Urea_{1.5}$. *Solid State Ionics, 199-200,* 32-36.
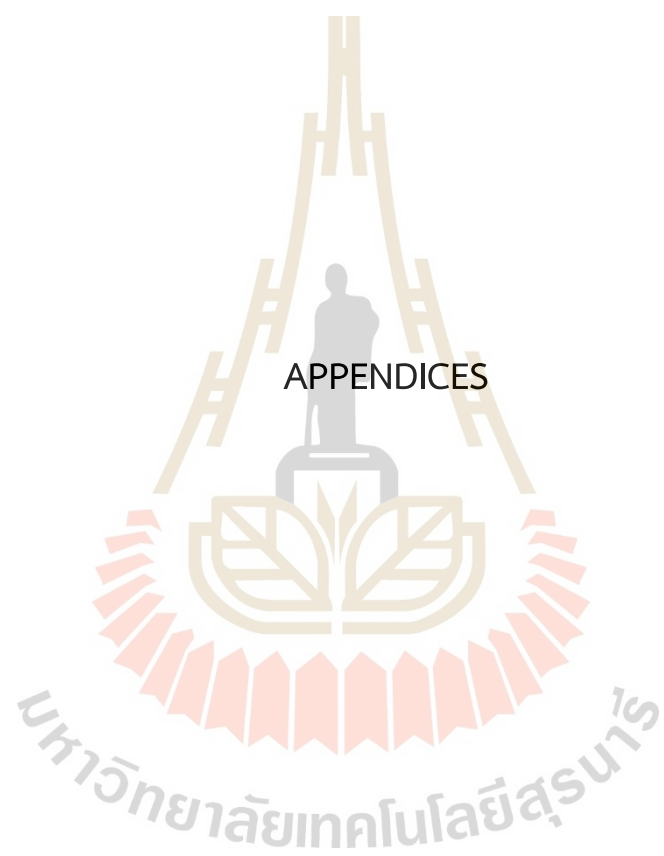
APPENDICES

# APPENDIX A
# THESIS OUTPUT (PUBLICATION)

**Sirirak, K.**, and Vao-soongnern, V. (2023). Molecular simulation for the effect of chain stiffness on polymer crystallization from the melts. *Journal of Molecular Liquids, 387*, 122650.
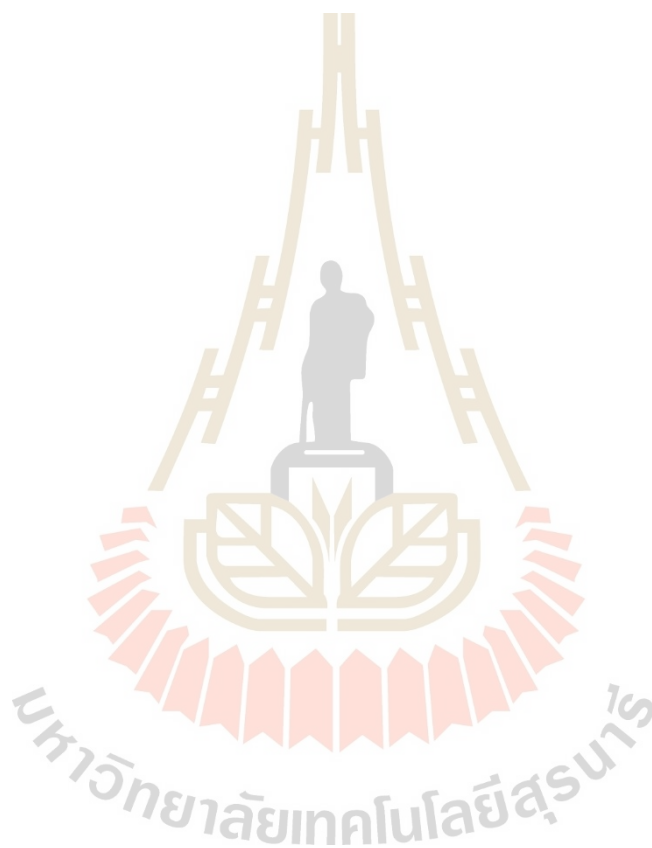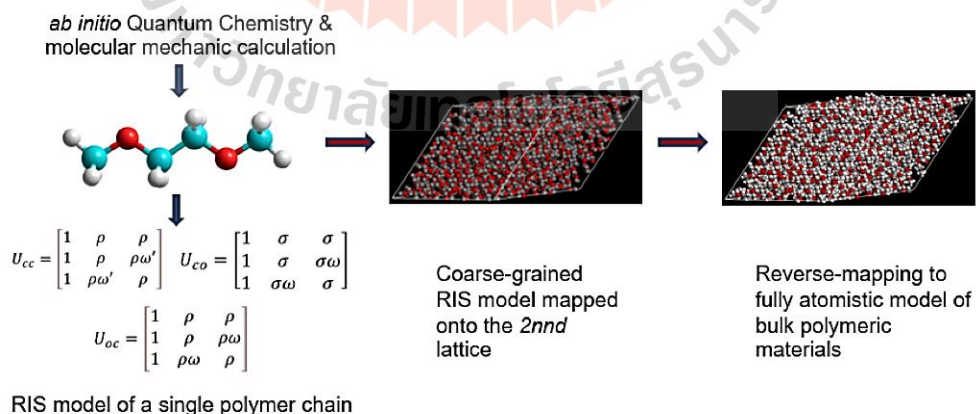
# APPENDIX B

# INTERNATIONAL CONFERENCE I

## National Graduate Research Polymer Conference 2021 (NGRPC2021), Virginia Tech., USA

### Multiscale Simulation for Molecular and Material Properties of Perfluoro- And Normal Poly(ethylene Oxide) Melts

Kanjana Sirirak[1], Visit Vao-Soongnern[1]

[1]Suranaree University of Technology

A recent development of a multiscale simulation of amorphous polymeric materials at the bulk density is applied to perfluoro-, PF-PEO, and normal poly(ethylene oxide), PEO, for comparison. Both polymers can be represented as (CF3O-[CF2-CF2-O]nCF3) and (CH3O-[CH2-CH2-O]nCH3) for PF-PEO and PEO, respectively. The model starts from the refinement of the original rotational isomeric state (RIS) model of PF-PEO and PEO determined from ab initio quantum chemistry calculation. The original statistical weights with third-order interaction were simplified for the coarse-grained (CG) PF-PEO and PEO chains. These CG polymer models were mapped on the second nearest neighbor diamond (2nnd) lattice. The average non-bonded intermolecular interactions were treated by the discretized Lennard-Jones (LJ) potential. PEO and PEI melts at the bulk density were generated and equilibrated using lattice Monte Carlo simulation. The on-lattice properties such as molecular size and conformational statistics agree well with the analytical theory. Fully atomistic amorphous PF-PEO and PEO models at bulk densities can be obtained by the reverse mapping procedure to recover the missing atoms. After an energy minimization and molecular dynamic simulation, properties including torsional angle distribution, solubility parameter and atomic pair correlation function and scattering structure factor were compared between PF-PEO and PEO.

*ab initio* Quantum Chemistry & molecular mechanic calculation

$$U_{cc} = \begin{bmatrix} 1 & \rho & \rho \\ 1 & \rho & \rho\omega' \\ 1 & \rho\omega' & \rho \end{bmatrix} \quad U_{co} = \begin{bmatrix} 1 & \sigma & \sigma \\ 1 & \sigma & \sigma\omega \\ 1 & \sigma\omega & \sigma \end{bmatrix}$$

$$U_{oc} = \begin{bmatrix} 1 & \rho & \rho \\ 1 & \rho & \rho\omega \\ 1 & \rho\omega & \rho \end{bmatrix}$$

RIS model of a single polymer chain

Coarse-grained RIS model mapped onto the *2nnd* lattice

Reverse-mapping to fully atomistic model of bulk polymeric materials

# APPENDIX C

# INTERNATIONAL CONFERENCE II

## The 26th International Conference on Chemical Thermodynamics (ICCT-2023), Osaka, JAPAN

## MOLECULAR SIMULATION OF THE EFFECT OF CHAIN STIFFNESS ON POLYMER CRYSTALLIZATION FROM THE MELTS

Kanjana Sirirak, Kritsana Monkhlang, Visit Vao-soongnern[1]

[1]Suranaree University of Technology, School of Chemistry, Nakhon Ratchasima, 30000, Thailand
e-mail: kanjanasirirak2@gmail.com
Key Words: *molecular simulation, polymer crystallization, chain stiffness.*

Polymer crystallization can be affected by many extrinsic factors, for example, crystallization temperature, cooling rate and pressure. In addition, intrinsic factors such as chain regularity, molecular weight, intermolecular forces, pendant groups, chain topology and chain stiffness can favor a high crystallinity. During the crystallization process, chain ordering takes place only after the chains are stretched to some extent [1]. As real polymers are not fully flexible but most of them have an intrinsic stiffness leading to locally stiff parts. A generic polymer model with only the stiffness entering as a single parameter ($k$) characterizing specific polymers using the modification of the first ($k\sigma$) and the second order ($k\omega$) parameters in the rotational isomeric state (RIS) model of polyethylene (PE) chain. For PE-like models with $k$ in the range of $0.5 - 2.0$ (the characteristic ratio = 4.49 - 8.70 at 473 K), chains can be regarded as more flexible to stiffer chains than normal PE ($k = 1.0$). Herein, MC simulation of the coarse-grained polyethylene (PE) model on the high coordination lattice previously used to study the crystallization of ring polymer [2] is extended to investigate the effect of the chain stiffness on the structural formation upon cooling from the melts. The evolution of the ordered structure of polymer is characterized in terms of the fraction of *trans* state, the length of *trans* sequence, the orientation correlation function at bond and molecular scale, the intermolecular pair correlation function, and the anisotropic change of chain dimension. Simulation data suggest that the rate of structure formation and the degree of crystallinity are better increased for the normal PE chain ($k = 1.0$). Both more flexible and stiffer chains exhibit poorer crystallization. More flexible chains ($k = 0.5$) can adopt more amount of *gauche* conformation and are difficult for the ordered structure formation. On the other hand, stiffer chains ($k = 1.5$ and 2.0), still have *gauche* conformation and cannot be converted to *trans* state during the stepwise cooling from the melts due to the high energy barrier. Our study suggests that only polymers with the appropriate chain stiffness can exhibit clear evidence for crystallization.
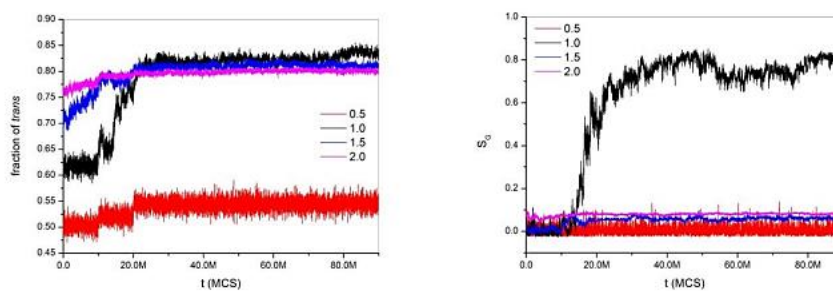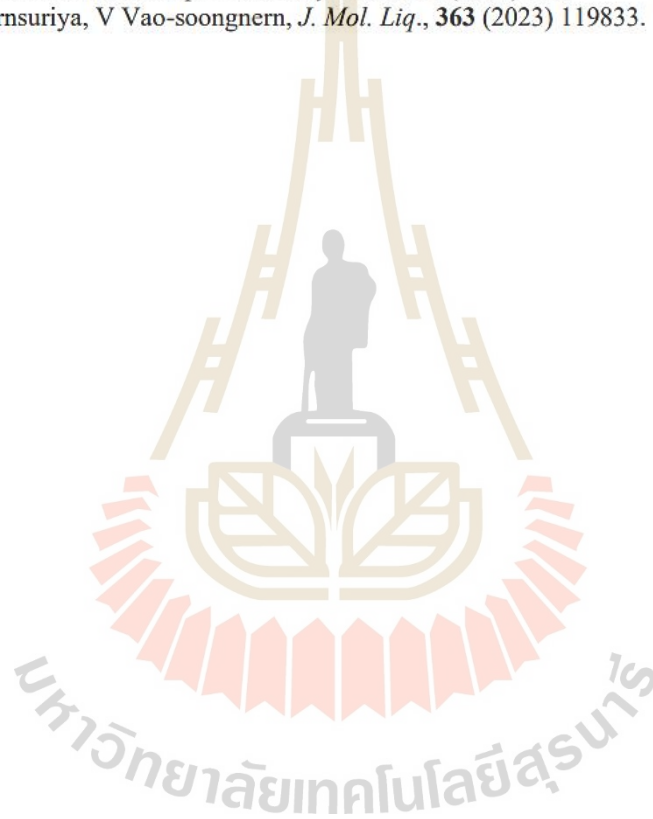
Figure 1 The evolution of (a) the fraction of *trans* conformation and (b) The global orientation order parameter function of PE model with different chain stiffness parameters.

[1] G. Xu, W. L. Mattice, *Comp. Theo. Polym. Sci.*, **11** (2001) 405.
[2] S Jamornsuriya, V Vao-soongnern, *J. Mol. Liq.*, **363** (2023) 119833.

# CURRICULUM VITAE

**Name:** Kanjana Sirirak

**Date of Birth:** 10th June, 1998 at Ubonratchatani Thailand

| | | |
|---|---|---|
| **Education:** | 2021- 2024 | M. Sc. Chemistry, Suranaree University of Technology, DPST scholarship and NRCT Research Assistantship |
| | 2017 - 2021 | B. Sc. Chemistry, Suranaree University of Technology, DPST scholarship |
| | 2014 – 2017 | Matthayom Trakan Phuetphon School, Science-Mathematics (Gifted program) |

**Publications:**

1. Sirirak, K., and Vao-soongnern, V. (2023). Molecular simulation for the effect of chain stiffness on polymer crystallization from the melts. *Journal of Molecular Liquids, 387*, 122650.

2. Sirirak, K., and Vao-soongnern, V. (2023). Molecular simulation of structural properties of polymer blend nanofilms. *Journal of Polymer Research, 30*, 46.

3. Vao-soongnern, V., Sukhonthamethirat, N., Rueangsri, K., Sirirak, K., and Matsuba, G. (2023). Molecular simulation of the structural formation of mono- and bidisperse polyethylene upon cooling from the melts. *Journal of Molecular Liquids, 376*, 121434.

4. Vao-soongnern, V., Chaodamrongsakul, J., Reungsri, K., Sirirak, K., Amonpattaratkit, P., and Klysubun, W. (2023). A Combined Molecular Dynamic Simulation and Synchrotron X-Ray Absorption Spectroscopy to Characterize the Atomistic Local Structure of Ion-Containing Polymers. *Macromolecular Symposia, 408*, 2100444.

**Government scholarship:**

The Development and Promotion of Science and Technology Talented (DPST) scholarship (fully supported)